

FABRICATION AND CHARACTERIZATION OF A MEMS
MAGNETOMETER

FABRICATION AND CHARACTERIZATION OF A MEMS
MAGNETOMETER FOR MEASURING TORQUE OF A MAGNETIC
CRYSTAL

By SARAH SELESNIC, B.Sc.

A Thesis Submitted to the School of Graduate Studies in Partial Fulfilment of the
Requirements for the Degree Master of Applied Science

McMaster University © Copyright by Sarah Selesnic, September 2012

McMaster University MASTER OF APPLIED SCIENCE (2012) Hamilton,
Ontario (Engineering Physics)

TITLE: Fabrication and Characterization of a MEMS Magnetometer for
Measuring Torque of a Magnetic Crystal

AUTHOR: Sarah Selesnic, B.Sc. (McMaster University)

SUPERVISORS: Professor Rafael Kleiman, Professor Graeme Luke

NUMBER OF PAGES: xii, 109

ABSTRACT

With the advances in MEMS technology, the studies of the properties of magnetic crystals have reached the microscopic level. Critical information such as the magnetization and susceptibility of a magnetic sample can be obtained using a microtorque magnetometer, such as ones incorporating piezoresistive or capacitive detection that have been fabricated and tested by earlier research groups. This type of magnetic information is useful in the study of superconductivity, for example. The microtorque magnetometer designed and fabricated in this thesis has the potential of being used in this field of study.

This thesis describes the design, fabrication and testing of a capacitive microtorque magnetometer. By using ANSYS, a computer modelling program, an ideal model of the rotating microtorque magnetometer was devised. Fabrication involved testing a variety of procedures before establishing the successful and efficient method of building the microtorque magnetometer. A fifth order resonant mode was successfully detected during the testing stage. A method of studying the desired resonant mode has been devised and explained in the later chapters of this thesis.

ACKNOWLEDGEMENTS

I would like to thank both of my supervisors Dr. Rafael Kleiman and Dr. Graeme Luke for the inspiration of this project, and for their encouragement and insightful guidance during this project. I want to express my deep appreciation to Abhishaik Rampal and Christopher Pope for laying the foundation for the electrical experiments, and for their helpful insights, encouragement, and considerable assistance throughout this project. As well, I am grateful to both Dr. Zhilin Peng and Doris Stevanovic for the training and extensive aid they provided during the fabrication stage, along with helpful advice. I am thankful to the MEMS group, which includes Dr. Sri Priya Sundararajan, Matthew Minnick, and Nikolaus Jewell, for their beneficial suggestions and discussions pertaining to this thesis. I want to thank my first (immediate and extended) as well as my second family for their encouragement and open homes during the period of this thesis. Last of all, I would like to extend my appreciation to all persons already mentioned and referred to for their overall support during the last three years.

TABLE OF CONTENTS

1. Introduction..... 1

1.1 MEMS 1

 1.1.1 Silicon 2

 1.1.2 Micromachining..... 2

1.2 Magnetometry 3

 1.2.1 Overview of Techniques 3

 1.2.2 Torque Magnetometry 4

1.3 MEMS Torque Magnetometers..... 5

1.4 Thesis Overview 7

2. Theory 9

2.1 Static and Dynamic Beam Bending..... 9

 2.1.1 Stress and Strain..... 9

 2.1.2 Euler-Bernoulli Beam Equation..... 11

 2.1.3 Bridge and Cantilever Modes 14

 2.1.3.1 Bridge Modes..... 14

 2.1.3.2 Cantilever Modes..... 15

 2.1.3.3 Cantilever Example..... 16

2.2 Harmonic Motion..... 18

 2.2.1 Simple Harmonic Motion 18

 2.2.2 Damped Harmonic Motion 19

 2.2.3 Damped, Driven Harmonic Motion 20

 2.2.3.1 Resonance 21

2.3 Capacitive Detection and Actuation..... 21

 2.3.1 Capacitive Detection..... 22

 2.3.2 Capacitive Actuation..... 22

 2.3.2.1 Using AC and DC Voltages..... 24

 2.3.3 Pull-in Effect..... 24

2.4 Magnetism 26

 2.4.1 Magnetization and Magnetic Fields..... 26

 2.4.1.1 Current Carrying Coils..... 28

 2.4.2 Torque 30

2.5 Electrostatic Determination of Torque 31

 2.5.1 Mechanical Torque 31

 2.5.2 Magnetic and Mechanical Torque 32

3. Numerical Analyses 33

3.1 Design..... 33

3.1.1 Original Model.....	33
3.1.2 Improved Model.....	35
3.2 Modal Analysis.....	36
3.2.1 Original Model.....	36
3.2.2 Improved Model.....	46
3.3 Structural Analysis.....	46
3.4 Pull-in Voltage.....	50
4. Fabrication.....	51
4.2 Attempted Procedures.....	58
4.2.1 Two Stage Release Process.....	58
4.2.2 Oxide Removal with Positive Photoresist as Mask.....	63
4.2.3 Two Stage Release with Alternate Masking Materials.....	64
4.2.4 Backside Etch Process with Flip Procedure.....	65
4.2.5 Backside Etch Process without Flip Procedure.....	68
4.3 Perforated Platform Procedure.....	70
4.3.1 Proof of Platform Release.....	77
5. Testing.....	81
5.1 Sample Preparation.....	81
5.1.1 Printed Circuit Boards (PCBs).....	81
5.1.2 Test Samples.....	82
5.1.3 Final Device.....	84
5.2 Electrostatic Testing.....	85
5.2.1 Initial Testing.....	86
5.2.2 Resonance Detection.....	88
5.2.2.1 Device in Vacuum.....	88
5.2.2.2 Important Circuit Components.....	89
5.2.2.3 Single Lock-In.....	90
5.2.2.4 Double Lock-In.....	94
5.2.2.5 Discussion of Results.....	98
5.3 Magnetic Torque Resonance Detection.....	102
6. Conclusion.....	103
6.1 Main Accomplishments.....	103
6.2 Future Work.....	104
References.....	105

LIST OF FIGURES

Figure 1.01: Rossel and Bauer’s piezoresistive cantilever torque magnetometer .. 5
 Figure 1.02: Rossel’s capacitive see-saw torque magnetometer 6
 Figure 1.03: Kohout’s two axes piezoresistive torque magnetometer..... 6
 Figure 2.01: Schematic diagram of a rod subjected to a uniform axial load 9
 Figure 2.02: Stress-strain diagram of stainless steel and silicon 10
 Figure 2.03: a) Schematic of a cantilever subjected to a constant transverse force
 b) Forces and moments acting on a small portion of the cantilever. 11
 Figure 2.04: The first four mode shapes of a bridge..... 15
 Figure 2.05: The first three mode shapes of a cantilever..... 16
 Figure 2.06: A schematic of a cantilever 17
 Figure 2.07: A diagram illustrating the direction of the magnetic field lines of a
 simple bar magnet..... 27
 Figure 2.08: Schematic of the reaction of a bar magnet in a uniform magnetic
 field. 27
 Figure 2.09: A current carrying loop. 29
 Figure 2.10: Bar magnet glued to a cantilever..... 30
 Figure 3.01: The original layout of the torque magnetometer 34
 Figure 3.02: Side view of the torque magnetometer..... 34
 Figure 3.03: Improved layout of the torque magnetometer 35
 Figure 3.04: Original torque magnetometer rotational (1st) mode..... 37
 Figure 3.05: Original torque magnetometer in-out of plane (2nd) mode..... 37
 Figure 3.06: Dimensions of beam..... 38
 Figure 3.07: Plot of rotational frequency versus length..... 39
 Figure 3.08: Plot of rotational frequency versus thickness..... 40
 Figure 3.09: Plot of rotational frequency versus width..... 40
 Figure 3.10: Plot of in-out of plane frequency versus length 42
 Figure 3.11: Plot of in-out of plane frequency versus thickness..... 42
 Figure 3.12: Plot of in-out of plane frequency versus width 43
 Figure 3.13: Contour plot of f_i/f_R for different dimensional ratios. 44
 Figure 3.14: Forces applied counter-clockwise to torque magnetometer model .. 47
 Figure 3.15: Displacement contour plot of torque magnetometer model 48
 Figure 3.16: Close up of displacement contour plot, without mesh 49
 Figure 3.17: Plot of displacement of bridge versus torque applied to platform ... 49
 Figure 4.01: Side view of SOI wafer (not to scale) 52
 Figure 4.02: Pattern of deposited chrome gold on sample (not to scale)..... 52
 Figure 4.03: SEM image of sidewall profile of sample after conventional RIE... 53
 Figure 4.04: SEM image of bridge between electrodes after DRIE 54
 Figure 4.05: Principle of the Bosch process 55
 Figure 4.06: Silicon nanowires 56
 Figure 4.07: Photolithography patterns a) for DRIE #1, where four holes are
 opened up in the device layer b) for DRIE #2, where the entire device layer is
 etched 58

Figure 4.08: AutoCAD image of the device. The area inside the purple lines represent the absence of oxide. 59

Figure 4.09: View of 5 μm narrow gap between top and bottom silicon layer 60

Figure 4.10: First completed device with a gold border 61

Figure 4.11: SEM image of a bridge connected to the platform..... 62

Figure 4.12: SEM image of second sample with NR9 remaining 63

Figure 4.13: Homemade mask for patterning backside hole 65

Figure 4.14: Image of the hole in the substrate after the KOH etch 66

Figure 4.15: View of a sample fabricated by the backside etch process with flip procedure, showing a bridge running between the electrodes 67

Figure 4.16: Another view of the same sample. Burn marks and cracks on a bridge can be seen. 68

Figure 4.17: View of a sample fabricated by the backside etch process without flip procedure. A hole in the substrate and a broken bridge can be seen. 69

Figure 4.18: Another view of the same sample. The hole in the substrate and another damaged bridge can be seen. 69

Figure 4.19: A third view of the same sample, showing a missing bridge 70

Figure 4.20: Revised photolithography pattern with holes in the platform and no L-shaped alignment marks 71

Figure 4.21: View of released L-shaped alignment mark and damaged bridge ... 72

Figure 4.22: Optical image of the completed device 73

Figure 4.23: View of platform and bridge running in between two electrodes 74

Figure 4.24: A close up of a bridge (10 μm wide) running in between two electrodes 74

Figure 4.25: View of a bridge running in between the electrodes 75

Figure 4.26: View of the released platform and a bridge 75

Figure 4.27: Close up of where a bridge meets the platform..... 76

Figure 4.28: Close up of a hole in the platform (100 μm in diameter) 76

Figure 4.29: View of a bridge, with the bottom of the bridge etched near electrode..... 77

Figure 4.30: View of the 5 μm gap between the platform and the substrate 78

Figure 4.31: Close up of where the bridge has broken off of the platform..... 79

Figure 4.32: View of backside of the platform, revealing the absence of oxide .. 79

Figure 5.01: A 12.5 X 12.5 mm device on a PCB 82

Figure 5.02: A corner of the first sample, showing the blob of silver paint shorting the device layer to the substrate. 83

Figure 5.03: A gold wire ball bonded to the device..... 83

Figure 5.04: Device represented in circuit form 85

Figure 5.05: Basic testing circuit, used to deflect the bridge..... 86

Figure 5.06: Deflection of bridge for certain values of DC voltages at middle portion of electrodes 87

Figure 5.07: Deflection of bridge for certain values of DC voltages at corner portion of electrodes 87

Figure 5.08: Device in vacuum, achieved by using a bell jar and a pump 89

Figure 5.09: Basic single lock-in circuit.....	90
Figure 5.10: A more sensitive version of the basic single lock-in circuit.....	91
Figure 5.11: Another sensitive version of the basic single lock-in.....	92
Figure 5.12: Amplitude of signal using single lock-in without 1615	93
Figure 5.13: Amplitude of signal using single lock-in and 1615.....	93
Figure 5.14: Basic double lock-in circuit.....	95
Figure 5.15: Second double lock-in circuit.....	95
Figure 5.16: Third double lock-in circuit.....	96
Figure 5.17: A sensitive version of the double lock-in, using a transformer.....	96
Figure 5.18: Amplitude comparison using double lock-in	97
Figure 5.19: Amplitude comparison using double lock-in and transformer.....	98
Figure 5.20: Resonant peak of bridge mode (B34).....	99
Figure 5.21: Phase of bridge mode (B34).....	100
Figure 5.22: Resonant peak of the bridge mode (B12).....	100
Figure 5.23: Phase of bridge mode (B12).....	101

LIST OF TABLES

Table 3.01: Torque magnetometer material dimensions and properties..... 34
Table 3.02: A list of modes and their corresponding resonant frequencies ($w = 5$
 μm)..... 36
Table 3.03: A list of modes and their corresponding resonant frequencies ($w = 10$
 μm)..... 45
Table 3.04: A list of modes and their corresponding resonant frequencies ($w = 10$
 μm , perforated platform)..... 46
Table 5.01: Theoretical and actual capacitances..... 84
Table 5.02: Comparison of stiffnesses and frequencies..... 102

LIST OF ABBREVIATIONS

AC	Alternating Current
BHF	Buffered Hydrofluoric Acid
CPD	Critical Point Dryer
DC	Direct Current
DRIE	Deep Reactive Ion Etching
HF	Hydrofluoric Acid
MEMS	Microelectromechanical Systems
PCB	Printed Circuit Board
RIE	Reactive Ion Etching
SOI	Silicon On Insulator

LIST OF SYMBOLS

ω	Angular frequency
C	Capacitance
i	Current
ρ	Density
F	Force
f	Frequency
B	Magnetic flux density, Magnetic field
m	Magnetic moment, Mass
M	Magnetization, Moment
I	Moment of inertia
μ	Permeability
μ_0	Permeability of a vacuum
ϵ_0	Permittivity of a vacuum
ϵ_R	Relative permittivity of a material
k	Stiffness/Spring constant
ϵ	Strain
σ	Stress
χ	Susceptibility
τ	Torque
V	Voltage
E	Young's modulus

1. Introduction

In the technological and industrial world, miniaturization is the dominating trend. As micro technologies expand and become widely used, more data or more objects can be fitted into the same quantity of space [1, 2]. One advantage of this practice is quite obvious – less space is needed for the equivalent amount of data, allowing for improvement of a device without increasing its size. However, the laws of physics that have been discovered by mankind differ in effect as the scale drops below the micrometer scale [3]. This is advantageous in some aspects, and disadvantageous in others. As scientists seek to obtain a better understanding of these microscale physical effects, the success of the microelectronics and microelectromechanical systems (MEMS) industry continues to increase.

The beginning of the microelectronics revolution technically started when the first transistor was built, but the MEMS revolution more or less began around the time of the Feynman lectures [1, 2]. Since the 1960's, the MEMS industry has grown. Inkjet nozzles for printers, accelerometers for automobiles, and gyroscopes for game controllers such as the Nintendo Wii are all examples of MEMS devices that have been on the market for several years [3].

1.1 MEMS

MEMS is a broad term that encompasses systems on the micro scale that contain electrical and mechanical parts. In this introduction, two kinds of MEMS will be briefly explained – sensors and actuators. Sensors are used for detection and data collection, whereas actuators convert input into an action or a motion.

Sensors convert energy from one form to another, generating an output reading. Energy forms include heat, pressure, force, sound, and light to name a few. Some examples are optical sensors, biomedical sensors, and chemical sensors. Optical sensors convert light into electronic output, and biomedical sensors detect biological components in the blood, such as glucose. There are a wide variety of chemical sensors, but the overall function is the same. Each sensor contains a component with a property that changes when it comes into contact with a chemical. An example would be a piece of metal – its resistivity changes when oxygen comes into contact with it.

In general, actuators convert electrical signals into actions. A few examples of effects employed by actuators include thermal forces, piezoelectricity, and electrostatic forces. MEMS devices that take advantage of thermal forces use bimetallic strips with different thermal expansion coefficients as a cantilever, so when it is heated, the cantilever bends in a certain direction. This is useful in actuators that contain microvalves – the cantilever acts as a gate.

An example of an actuator that uses piezoelectricity would be one containing piezoelectric crystals that deform when a voltage is applied. In a MEMS device that employs electrostatic force, a voltage is applied across parallel plates, and the parts attached to the parallel plates move as a result. An example would be microgrippers – the two arms are the parallel plates, and can open and close in correspondence to the voltage applied [3, 4].

The torque magnetometer contains both sensing and actuating components. It makes use of electrostatic forces and capacitance, which can be used both to drive and detect. In this device, a bridge and an electrode are the two parallel plates, thus when a voltage is applied the bridge moves. It is a sensor in that it will sense the change in capacitance across the parallel plates when the bridge moves without being driven.

1.1.1 Silicon

Single crystal silicon has excellent mechanical properties, and is inexpensive and widely available, which makes it a convenient and popular material to use in MEMS [5]. Before MEMS came on the scene, silicon was already being used in microelectronics. It can be easily used in batch fabrication – large cylinders of crystalline silicon can be grown and sliced into large wafers to be used for specific purposes. Silicon has a tensile yield strength three times higher than that of stainless steel wire, a Young's modulus close to that of stainless steel, and a Knoop hardness close to that of quartz and higher than most glasses [5]. Also, single crystal silicon has directionally dependent crystallographic planes, making it anisotropic. This property combined with the many chemical etchants (whether isotropic or anisotropic) available for silicon is very advantageous in the fabrication of microscopic devices [6].

1.1.2 Micromachining

Building of devices on the microscale requires alternate procedures than those used on the macroscale. These fabrication processes are divided into two large groups: additive or subtractive processes. Additive processes involve steps that add parts/layers to the device, whereas subtractive processes involve the removal of parts/layers of the device [5, 7, 8]. Both can involve photolithography and etching, although photolithography is associated more with additive processes and etching with subtractive. Depositing metal contacts is an additive process, and removal of a buried oxide layer is a subtractive process.

As will be explained in further detail, the torque magnetometer was fabricated using both additive and subtractive procedures. A silicon on insulator (SOI) wafer was used as the starting material – a silicon dioxide layer sandwiched

by two silicon layers. During the construction of the apparatus, both the top silicon layer and the silicon dioxide layer were etched in particular areas, forming the overall device.

1.2 Magnetometry

Magnetometry is the study of a material's magnetization properties, and is crucial, for example, in the investigation of high temperature superconductivity [9, 10]. It provides details of magnetic states, the presence of magnetic and electronic phase transitions, and gives insight into the behaviour resulting from a second order transition [10]. There are many methods of studying magnetization, four of which will be introduced in the subsection below: superconducting quantum interference device (SQUID), extraction, vibrating sample, and alternating gradient. Torque magnetometry will be explained in the following subsection. For more details on these and other methods, see the appropriate literature [9-15].

1.2.1 Overview of Techniques

A SQUID (superconducting quantum interference device) utilizes pick-up coils within a superconducting magnet system. The type of coil used can play a role in the sensitivity of the SQUID. As the sample is moved through the coils, voltage is measured as a function of distance. From this, torque data can be extracted. The temperatures inside the SQUID are kept at 1.7 - 300 K using a liquid helium cooling system [10]. SQUIDs are advantageous in that they are the most sensitive instrument available for measuring the magnetization of a material (can measure moments up to 10^{-7} emu) – if the magnetic field applied is relatively low [12, 16].

The extraction method is based on flux change, which is dependent on the sample's magnetization. Flux is measured in pulses: first when a sample is inside the search coil (encased within a solenoid), and is measured again when the sample is removed (or extracted). Thus the magnetization of a sample can be measured for a fixed field, but there is no simple way of continuously measuring magnetization [12]. Also, accurate measurements of small samples in pulsed fields are difficult – the pulse durations are too short, and the noise is too high [10].

In the vibrating sample technique, the sample is attached to the end of a long non-magnetic rod, and is suspended between two pick up coils. On the outside of these two pick-up coils are two electromagnets which provide the magnetic field. Alternatively, a solenoid can be used. The sample is vibrated (for example by a mechanical vibrator at the top of the rod), causing an oscillating

magnetic field around the two pick up coils. This results in an alternating electromotive force (emf), which is proportional to the sample's magnetic moment [14]. A lock-in amplifier is used to measure the emf signal. To keep the vibration amplitude constant, a reference magnet complete with its own two pick-up coils is used higher up on the rod. Magnetic moments of up to 10^{-5} emu can be measured, but the sample must weigh no greater than 1 g [12].

A more sensitive version of the vibrating sample method is the alternating gradient technique. It uses a fiber instead of a rod, and gradient coils instead of pick-up coils to generate an alternating field gradient. Magnetic moments up to 10^{-6} emu can be measured using commercial versions, but moments of 10^{-8} emu have been measured by P.J. Flanders [12, 15]. This method has a number of limitations in comparison to the vibrating sample technique. Samples with lower mass must be used, and cleanliness and proper mounting procedures are crucial due to its increased sensitivity. Also, using an alternating gradient means that the field is never constant, making data collection and calculations complicated [12].

1.2.2 Torque Magnetometry

When a sample is placed in a magnetic field, the magnetic moments inside that sample try to align with that field, exerting a torque on the sample. Torque magnetometers measure that torque, therefore it can detect changes in the magnetization of the sample [10]. In samples that are anisotropic, magnetic properties depend on the direction in which they are measured. There are different types of anisotropy: crystal (which arises from spin orbit coupling), shape, stress, exchange, and so on. Crystal anisotropy can be investigated by torque measurements [12].

Early torque magnetometers were basic – the sample was hung on a torsion rod and suspended between two magnets. When a magnetic field was applied, the resulting rotation of the torsion rod could be read by eye. This gives torque as a function of rotation angle [12, 14]. More advanced versions of this design increase accuracy by eliminating manual readouts in favour of electronic data collection [13].

Torque magnetometers of greater sensitivity have a different design. In common cases, the sample is on a cantilever which serves as one capacitor plate. The other capacitor plate is a short distance below the cantilever. Application of a constant magnetic field changes the magnetization of the sample, exerting a torque on the cantilever. As a result of the torque, the cantilever bends toward the second capacitor plate [10]. When a varying magnetic field is applied, the torque or the magnetization of the sample as a function of the field can be obtained [10].

Torque magnetometry reveals relative changes in magnetization of anisotropic samples, or sharp changes in magnetization at phase transitions [10]. At high magnetic fields, torque magnetometers are more sensitive than their

SQUID counterparts [16, 17]. Thus torque magnetometers are a useful tool in the research of the magnetic properties of materials.

1.3 MEMS Torque Magnetometers

Within the last two decades the two fields of torque magnetometry and MEMS have joined to form miniature devices that are practical for magnetic research. There are a number of different ways to incorporate torque magnetometry into the MEMS sphere, as demonstrated by the different articles published by various research groups [16-23]. Cantilevers whose motion alters the piezoresistivity or capacitance are the common design among microtorque magnetometers. Rossel and Bauer published a paper in 1995 on a novel piezoresistive cantilever torque magnetometer, and Brugger and Rossel followed in 1997 with a paper on optimizations of Rossel and Bauer's design [17, 18]. Rossel and Bauer's original design is shown in Figure 1.01, where it can be seen that a Wheatstone bridge was used in detecting changes in resistance. A torque sensitivity of 10^{-14} Nm was measured using this device. Rossel's group made use of commercial piezoresistive cantilevers, whereas Brugger built his own. Their cantilevers hold micrometer (μm) sized samples.

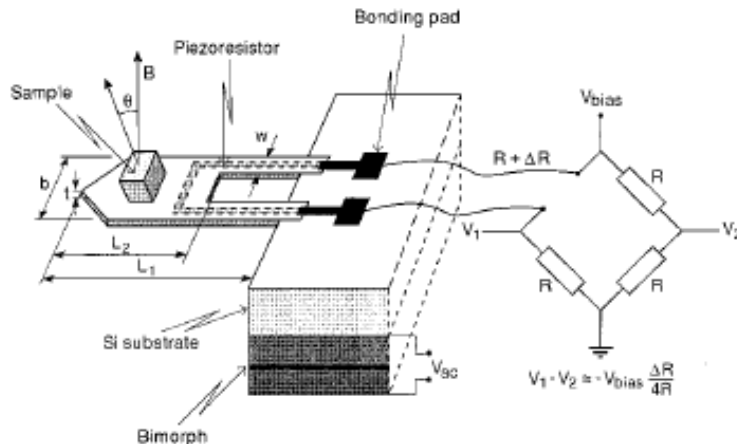


Figure 1.01: Rossel and Bauer's piezoresistive cantilever torque magnetometer [17]

In the years following, Rossel and his team also built a capacitive torque magnetometer using cantilevers. The design of his device is shown in Figure 1.02, from his published 1998 article. In contrast to his earlier torque magnetometer, the most recent one holds millimetre (mm) sized samples. Using a custom made capacitance bridge, it can give a torque sensitivity of 3×10^{-13} Nm. The letters A,

B, and C in the figure denote capacitors [19]. As the sample causes the platforms to seesaw about the torsion axis (the x-axis), a change in capacitance occurs.

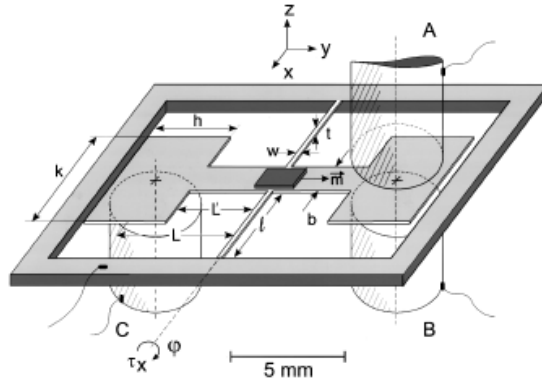


Figure 1.02: Rossel's capacitive see-saw torque magnetometer. The letters A, B, and C denote capacitors.

A more recent example of a MEMS torque magnetometer is shown in Figure 1.03, designed and fabricated by Kohout and his colleagues. Successfully fabricated in 2006, this design allows for simultaneous piezoresistive measurements along two perpendicular axes without a decrease in sensitivity, as described in his journal article [20]. However, his device generates a torque sensitivity 10 times smaller than Rossel's piezoresistive design. On the other hand, a larger variety in measurement modes allows for greater insight into the magnetic properties of high temperature superconducting samples.

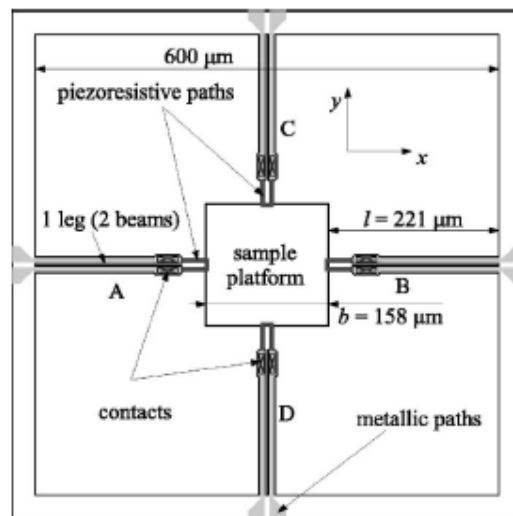


Figure 1.03: Kohout's two axes piezoresistive torque magnetometer [20]

These are just a few examples of microfabricated torque magnetometers that have been fabricated by various research groups, with the view of improving upon an earlier design.

1.4 Thesis Overview

Piezoresistivity and capacitance are the two main options for electrical measurements. Both types of measurements have two main disadvantages. Piezoresistive measurements generate greater background noise at high fields due to magnetoresistance effects, and have a temperature dependence [21]. On the other hand, capacitive measurements are less sensitive, and are more difficult to miniaturize [20]. However, utilizing capacitors would result in less undesired background noise. Knowing that the sample size would be on the order of a millimetre, and that certain features of the torque magnetometer would be on the millimetre scale, the problem of capacitive miniaturization was not as much of an issue. Furthermore, a device using capacitive detection can also be driven, whereas a device using piezoresistivity cannot. This allows for work in both the direct current and alternating current modes. In light of this, it was decided to use capacitance as the method of detection.

The purpose of the torque magnetometer is to measure the torque of magnetic crystals as a function of an applied magnetic field, using capacitor plates to detect beam deflection. The measurement of torque will give changes in magnetization of the sample, giving further insight into the magnetic properties of the crystal. This torque magnetometer was built with the view of being used in magnetic crystal research. It was designed so that it would have the ability to hold millimetre sized samples and to detect beam deflections in the range of hundreds of nanometers (nm). Thus the size of the sample platform and the dimensions of the device were chosen to accommodate these goals.

The particular design of this torque magnetometer was chosen over the more common MEMS torque magnetometer designs, described above, because the goal was to build a torque magnetometer that has the potential of being more sensitive and addresses the disadvantages inherent in their designs. A novel mechanical structure was designed where the fundamental mode is a rotational mode, helping to eliminate unwanted noise from the environment. This design also takes advantage of the thickness of the SOI device layer to increase the overlap capacitance and increase detection sensitivity. The capacitance approach was chosen because it can be used in both ac and dc modes and is relatively insensitive to changes in temperature or magnetic field, ideal for use in cryogenic measurement of the magnetic properties of materials.

It is necessary to provide a summary of the torque magnetometer's developmental flow, to aid in the understanding of this thesis. The developmental flow consists of three stages – design/numerical analyses, fabrication, and testing. First, a working model of the torque magnetometer was designed. The improved

model is also introduced, to allow the reader to compare the two designs. Numerical analyses of this model are divided into two parts – modal and structural. The modal analysis is concerned primarily with the frequency modes of a model with particular dimensions. The purpose for which the torque magnetometer is designed is best achieved if the rotational mode is fundamental; hence modal analysis is very necessary in the determination of dimensions. For example, a relatively thick device layer was chosen so that the rotational mode would be softer than the in and out of plane mode. These statements will be better understood once the reader is made familiar with the design of the torque magnetometer, presented in Chapter 3. Structural analysis is concerned with the deflection of the bridges, and is useful in giving an approximation of the signal strength. This is necessary for the determination of electrode placement. Once the design of the torque magnetometer was established, development of the fabrication process was the next step. A general overview of the three main steps in the fabrication process flow is laid out, and then the details of each of the five attempted processes are given. The reason for the different attempts was the difficulty in releasing the device platform. In explaining the details of each attempt, the reader is made to understand the intricate details of the device, the challenges that were faced, and the importance of certain procedures. Once the design of the torque magnetometer was improved in response to the challenges, fabrication of the device was successful. This procedure is laid out in detail, along with proof that the device was fully complete. Once the fabrication process was established, a number of samples were made for testing. After sample preparation, electrostatic testing was conducted. Electrostatic testing is divided into two stages – initial and resonance. Initial testing is concerned with the basic function of the torque magnetometer, and is necessary to check that all connections are secure and to compare measured capacitances with theoretical values. Resonance testing is concerned primarily with the observation of the fundamental mode, as well as interesting higher order modes. Two main resonance circuits are explained in detail – the single lock-in, and the double lock-in. Results of the testing are discussed, and ideas for future work are given.

The contents of this thesis are quickly summed up here: a brief introduction to necessary theory precedes the numerical analyses of the torque magnetometer. Following that, the numerical analyses, fabrication, and testing of the device are covered in detail. The thesis ends with the conclusion along with proposed ideas of future work that can be done with the torque magnetometer.

2. Theory

This chapter will cover the basic theory behind static and dynamic beam bending, harmonic motion, capacitive detection and actuation, and magnetism. The mathematical relationships derived here will be useful in later chapters when discussing numerical analyses and testing of the torque magnetometer.

2.1 Static and Dynamic Beam Bending

The basic mechanics of materials are discussed in this section, focussing on the reaction of beams to axially and transversely applied loads. In the case of the transversely applied load, the modes of the bridge and cantilever are derived.

2.1.1 Stress and Strain

For a rod of a given cross section A subjected to a uniform axial load P as shown in Figure 2.01, the average value of the stress σ over the cross section is given as follows [3, 24]:

$$\sigma = \frac{P}{A} \quad 2.01$$



Figure 2.01: Schematic diagram of a rod subjected to a uniform axial load P over a cross section of area A , with elongation δ .

The corresponding strain ε is deformation δ per unit length L :

$$\varepsilon = \frac{\delta}{L} \quad 2.02$$

Stress-strain diagrams for different materials are obtained by performing tensile tests on a rod. A rod of a particular material is subjected to a stretching force along its length axis (similar to Figure 2.01) and the deformation is measured. Figure 2.02 is a stress-strain diagram of two materials, stainless steel and silicon. Stainless steel is a typical ductile material, whereas silicon is brittle. The difference can be clearly seen in the diagram.

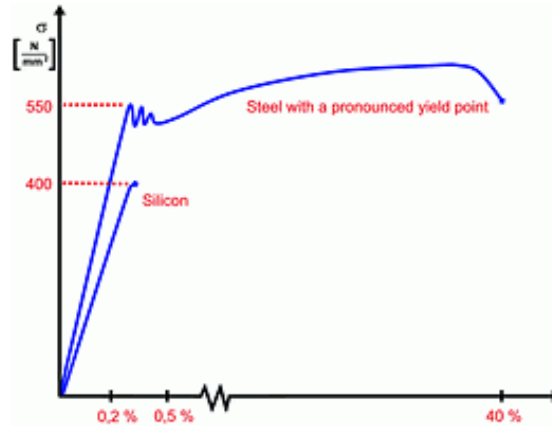


Figure 2.02: Stress-strain diagram of stainless steel and silicon [25].

Looking at the portion of the diagram corresponding to silicon, the relationship between the stress and strain is linear, where E is the modulus of elasticity, or Young's modulus:

$$\sigma = E\varepsilon \quad 2.03$$

Substituting equation 2.01 for stress and equation 2.02 for strain, and rearranging, the result is Hooke's Law [3, 24]:

$$\left(\frac{F}{A}\right) = E\left(\frac{x}{L}\right) \quad 2.04$$

$$F = \left(\frac{EA}{L}\right)x \quad 2.05$$

Where F is the uniform load P , and x is the deformation δ . From the familiar version of Hooke's Law:

$$F = kx \quad 2.06$$

The spring constant k of a rod of silicon subjected to a stretching force along the length axis is therefore:

$$k = \frac{EA}{L} \quad 2.07$$

2.1.2 Euler-Bernoulli Beam Equation

For a beam fixed at one end and free at the other end and deflected by an amount v in the y direction as shown in Figure 2.03a, the resulting forces and moments on a small part dx of the cantilever is shown in Figure 2.03b.

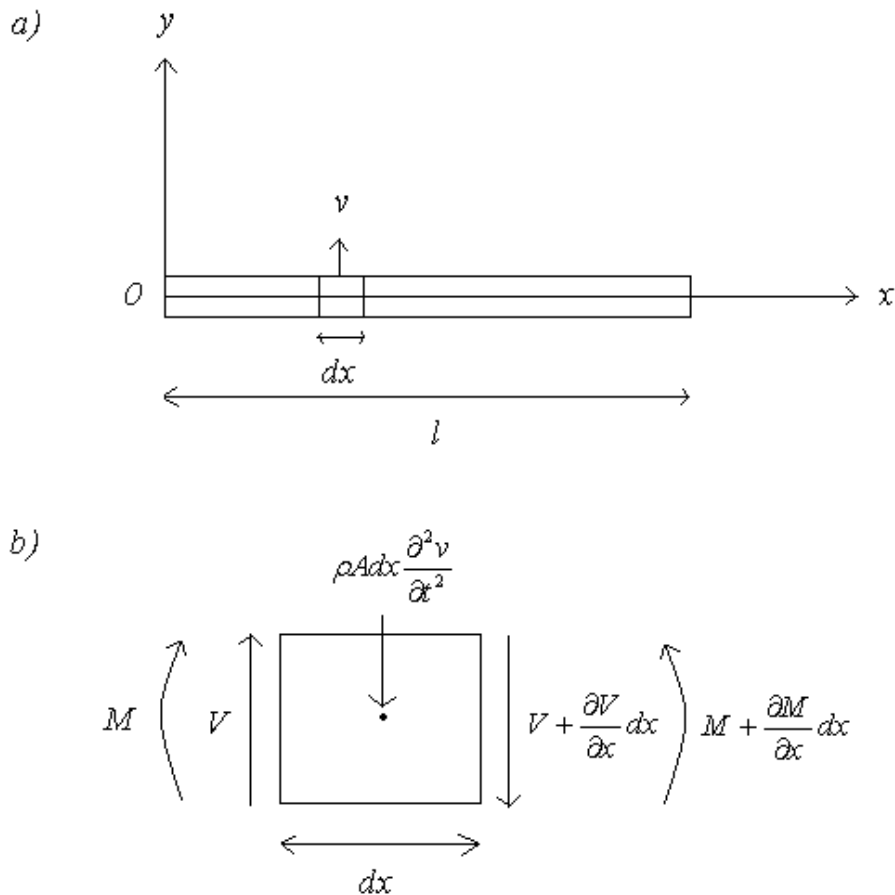


Figure 2.03: a) Schematic of a cantilever subjected to a constant transverse force
 b) Forces and moments acting on a small portion of the cantilever [26].

When at equilibrium in the y direction, the forces are given as follows:

$$V - (V + \frac{\partial V}{\partial x} dx) - \rho A dx \frac{\partial^2 v}{\partial t^2} = 0 \quad 2.08$$

$$\frac{\partial V}{\partial x} dx + \rho A dx \frac{\partial^2 v}{\partial t^2} = 0 \quad 2.09$$

Where V is the shearing force, ρ is the density of the material, A is the cross section, and v is the amount of deflection experienced by the small part dx of the cantilever. At equilibrium, the moments are given below:

$$-V dx + \frac{\partial M}{\partial x} dx \approx 0 \quad 2.10$$

Differentiating equation 2.10 with respect to x and rearranging results in:

$$\frac{\partial V}{\partial x} dx \approx \frac{\partial^2 M}{\partial x^2} dx \quad 2.11$$

Substituting equation 2.11 into equation 2.09 gives:

$$\frac{\partial^2 M}{\partial x^2} dx = -\rho A dx \frac{\partial^2 v}{\partial t^2} \quad 2.12$$

The definition of moment is as follows (the derivation of which can be found in the textbook *Mechanics of Materials* [24]):

$$M = EI \frac{\partial^2 v}{\partial x^2} \quad 2.13$$

Where E is Young's modulus and I is the second moment of inertia. Taking the second derivative of equation 2.13 with respect to x and multiplying by dx gives [3, 24, 26]:

$$\frac{\partial^2 M}{\partial x^2} dx = EI \frac{\partial^4 v}{\partial x^4} dx \quad 2.14$$

Substituting equation 2.12 into equation 2.14 results in the Euler-Bernoulli beam equation:

$$EI \frac{\partial^4 v}{\partial x^4} dx = -\rho A dx \frac{\partial^2 v}{\partial t^2} \quad 2.15$$

This equation can be arranged more conveniently as:

$$\frac{\partial^4 v}{\partial x^4} = -\frac{1}{a^2} \frac{\partial^2 v}{\partial t^2} \quad 2.16$$

With the constant being defined as $a = \sqrt{\frac{EI}{\rho A}}$.

The solution for equation 2.16 is given below [26]:

$$v = X(A \cos \omega t + B \sin \omega t) \quad 2.17$$

Substituting equation 2.17 into equation 2.16 results in a 4th order differential equation (where $q^4 = \frac{\omega^2}{a^2}$):

$$\frac{\partial^4 X}{\partial x^4} - q^4 X = 0 \quad 2.18$$

Letting $X = e^{nx}$, equation 2.18 becomes:

$$e^{nx}(n^4 - q^4) = 0 \quad 2.19$$

The four separate solutions are as follows (where $i = \sqrt{-1}$):

$$n = \begin{cases} q \\ -q \\ iq \\ -iq \end{cases} \quad 2.20$$

Combining all the solutions into the definition of X results in (with C, D, E, and F being constants):

$$X = Ce^{qx} + De^{-qx} + Ee^{iqx} + Fe^{-iqx} \quad 2.21$$

Using Euler’s formula and the trigonometric identities for $\sinh x$ and $\cosh x$, the solution for the Euler-Bernoulli beam equation can also be presented in the following two ways [26, 27]:

$$X = C_1 \sin qx + C_2 \cos qx + C_3 \sinh qx + C_4 \cosh qx \quad 2.22$$

$$X = C_1 (\cos qx + \cosh qx) + C_2 (\cos qx - \cosh qx) + C_3 (\sinh qx + \sinh qx) + C_4 (\sin qx - \sinh qx) \quad 2.23$$

With C_1 , C_2 , C_3 , and C_4 being constants that can be determined using specific boundary conditions.

2.1.3 Bridge and Cantilever Modes

The modes for a beam with different end conditions can be found by solving the Euler-Bernoulli beam equation. Two specific solutions will be derived here – one for a fixed-fixed beam (bridge), and one for a fixed-free beam (cantilever).

At a fixed end of the beam, the deflection and the slope of the deflection are zero. Therefore the conditions are as follows [26]:

$$X = 0 \quad X' = 0 \quad 2.24$$

At a free end of a beam, the bending moment and the shearing force are equal to zero. Thus the following conditions are obeyed:

$$X'' = 0 \quad X''' = 0 \quad 2.25$$

2.1.3.1 Bridge Modes

For a bridge of length l , the end conditions are as follows [26]:

$$X_{x=0} = 0 \quad X'_{x=0} = 0 \quad X_{x=l} = 0 \quad X'_{x=l} = 0 \quad 2.26$$

For the first two conditions to be obeyed, the constants C_1 and C_3 in equation 2.23 must be zero. This results in:

$$X = C_2 (\cos qx - \cosh qx) + C_4 (\sin qx - \sinh qx) \quad 2.27$$

Using the last two conditions in equation 2.26 and finding the determinant, the result is as follows:

$$\cos ql \cosh ql = 1 \tag{2.28}$$

The roots are given below, where $j = 1, 2, 3, \dots$:

$$q_j l = \left(j + \frac{1}{2}\right)\pi \tag{2.29}$$

Recalling that $q^4 = \frac{\omega^2}{a^2}$, and looking forward to equation 2.48, the frequency is:

$$f_j = \frac{\omega_j}{2\pi} = \frac{q_j^2 a}{2\pi} \tag{2.30}$$

The first four mode shapes of the bridge are shown in Figure 2.04.

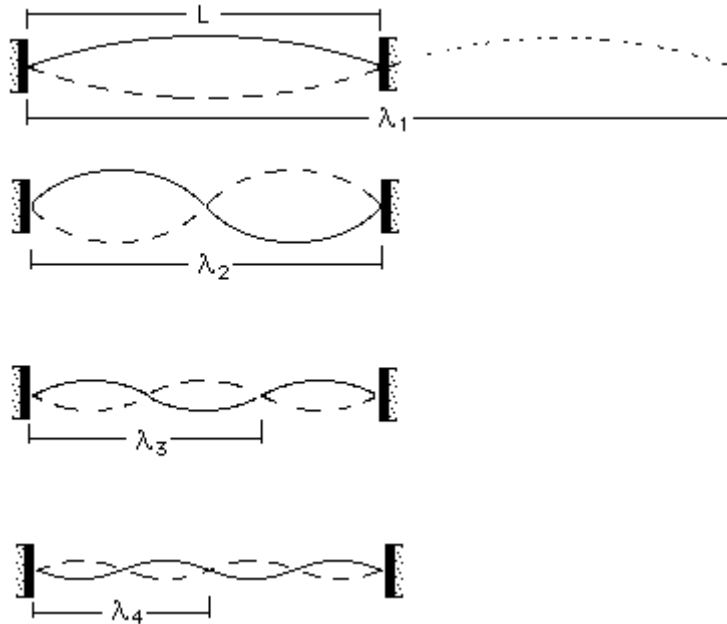


Figure 2.04: The first four mode shapes of a bridge [28].

2.1.3.2 Cantilever Modes

For a cantilever of length l , the end conditions are as follows [26]:

$$X_{x=0} = 0 \quad X'_{x=0} = 0 \quad X''_{x=l} = 0 \quad X'''_{x=l} = 0 \quad 2.31$$

Again, the first two conditions result in equation 2.27. Using the last two conditions and finding the determinant results in:

$$\cos ql \cosh ql = -1 \quad 2.32$$

The roots are given below (where $j = 1, 2, 3, \dots$), with the corresponding frequency being the same as equation 2.30:

$$q_j l = \left(j - \frac{1}{2}\right)\pi \quad 2.33$$

The first three mode shapes of the cantilever are shown in Figure 2.05.

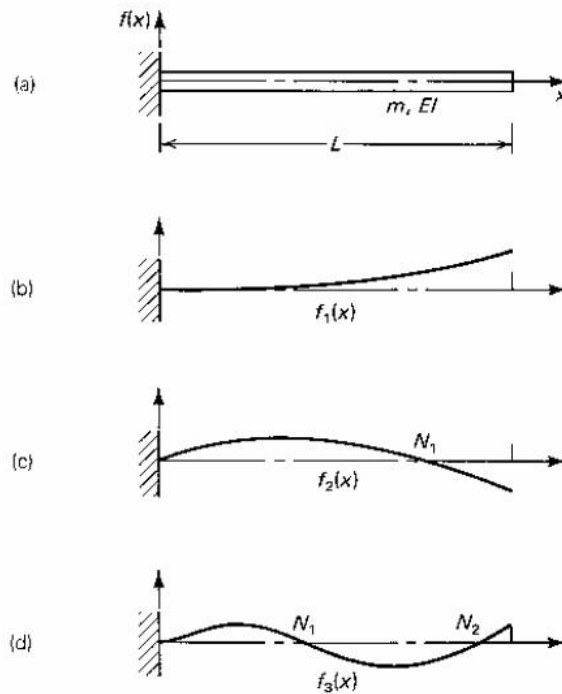


Figure 2.05: The first three mode shapes of a cantilever [29].

2.1.3.3 Cantilever Example

For a cantilever subjected to a transverse load as shown in Figure 2.06, the amount of deflection can be calculated starting with equation 2.13.

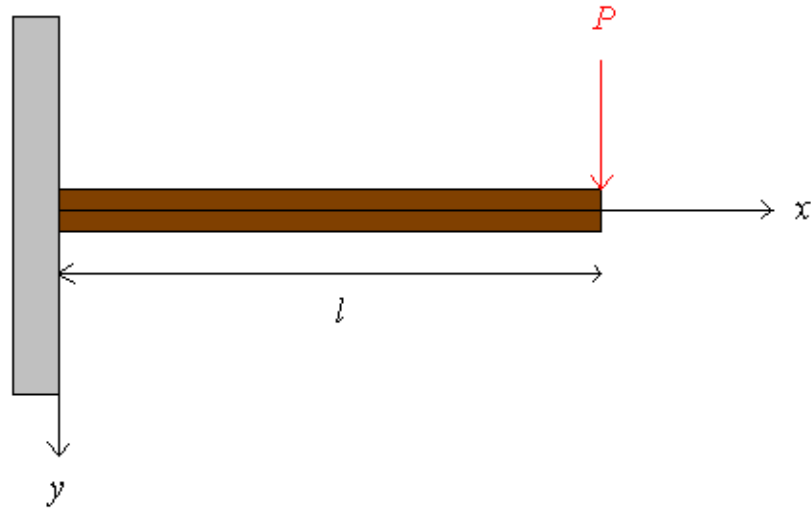


Figure 2.06: A schematic of a cantilever of length l subjected to a transverse load P on the free end.

At some distance x to the left of where the transverse load is applied, the moment is given as follows [24]:

$$M = -Px \quad 2.34$$

Substituting equation 2.34 into equation 2.13, the result is:

$$EI \frac{\partial^2 v}{\partial x^2} = -Px \quad 2.35$$

By integration and solving for the constants, the equation of the elastic curve can be determined:

$$v = \frac{P}{6EI} (-x^3 + 3L^2x - 2L^3) \quad 2.36$$

Thus the deflection at the free end of the cantilever is therefore (where $x = L$):

$$v = -\frac{PL^3}{3EI} \quad 2.37$$

From equation 2.06, the stiffness or the spring constant of the cantilever can be defined as:

$$k = -\frac{P}{v} \quad 2.38$$

Therefore, the stiffness of a cantilever subjected to a transverse load at its free end is as follows [24]:

$$k = \frac{3EI}{L^3} \quad 2.39$$

Where I is the second moment of inertia of a rectangular cantilever, given below (with the load being applied parallel to the width w of the beam, and perpendicular to the thickness t of the beam) [2, 24]:

$$I = \frac{tw^3}{12} \quad 2.40$$

2.2 Harmonic Motion

Oscillations, or vibrations, are an ordinary part of every day life. From a sitting person's knee jittering up and down to the pulsating movement of a speaker to the whirring of a chainsaw, periodic movements are all around us. All objects have a natural (or resonant) frequency – the frequency at which they will naturally vibrate. If an object is subjected to a dynamic force at its resonant frequency, it will begin to vibrate in response, whether it be a bridge, a piece of string, or a crystal glass. The amplitude of this response is greater than it would be if the force were not at its resonant frequency. An object that is vibrating is said to be in harmonic motion.

2.2.1 Simple Harmonic Motion

The simplest case of a harmonic oscillator is a mass suspended from a ceiling by a spring. Equating the spring force k with Newton's first law (where m is the mass, a multiple of density and volume: $m=\rho V$) and rearranging [30, 31]:

$$-kx = m\ddot{x} \quad 2.41$$

$$m\ddot{x} + kx = 0 \quad 2.42$$

When put in a slightly different form, the differential equation becomes:

$$\ddot{x} + \omega_0^2 x = 0 \quad 2.43$$

Where the angular frequency is given as follows:

$$\omega_0^2 = \frac{k}{m} \quad 2.44$$

The solution to the differential equation is of the simple form:

$$x(t) = A \sin(\omega_0 t + \phi) \quad 2.45$$

The motion of the mass oscillating about its equilibrium position repeats itself after phase advances of 2π . Each repetition occurs during a time period called the period of oscillation. The period of the oscillation is [30, 31]:

$$T_0 = \frac{2\pi}{\omega_0} \quad 2.46$$

Frequency is the number of cycles per unit time:

$$f_0 = \frac{1}{T_0} \quad 2.47$$

Substituting equation 2.46 into equation 2.47 and rearranging:

$$\omega_0 = 2\pi f_0 \quad 2.48$$

2.2.2 Damped Harmonic Motion

In almost all harmonic motion systems, there is a significant damping force that needs to be incorporated into the differential equation [30, 31]:

$$\ddot{x} + 2\beta\dot{x} + \omega_0^2 x = 0 \quad 2.49$$

Where the damping parameter is defined as follows (with b being the proportionality constant):

$$\beta = \frac{b}{2m} \quad 2.50$$

Therefore, the general solution is:

$$x(t) = e^{-\beta t} \left[A_1 e^{\sqrt{\beta^2 - \omega_0^2} t} + A_2 e^{-\sqrt{\beta^2 - \omega_0^2} t} \right] \quad 2.51$$

More specific solutions depending on the damping conditions (underdamping, critical, and overdamping) can be worked out. Refer to Marion and Thornton's book or Fowles and Cassiday's book for the solutions [30, 31].

2.2.3 Damped, Driven Harmonic Motion

When a harmonic oscillator is subject to a periodic driving force, the differential equation then becomes [30, 31]:

$$\ddot{x} + 2\beta\dot{x} + \omega_0^2 x = A \cos \omega t \quad 2.52$$

With the amplitude of the driving force given as follows:

$$A = \frac{F_0}{m} \quad 2.53$$

The general solution is composed of two parts, the complementary and the particular solutions:

$$x(t) = x_c(t) + x_p(t) \quad 2.54$$

The complementary solution is simply equation 2.51. The particular solution is given below:

$$x_p(t) = D \cos(\omega t - \delta) \quad 2.55$$

Where the amplitude D and phase shift δ are defined as:

$$D = \frac{A}{\sqrt{(\omega_0^2 - \omega^2)^2 + 4\omega^2\beta^2}} \quad 2.56$$

$$\delta = \tan^{-1} \left(\frac{2\omega\beta}{\omega_0^2 - \omega^2} \right) \quad 2.57$$

2.2.3.1 Resonance

If the driving force is at the object's resonant frequency, the amplitude of the oscillation is at its maximum and the following condition is obeyed [30]:

$$\left. \frac{dD}{d\omega} \right|_{\omega=\omega_R} = 0 \quad 2.58$$

Taking equation 2.56 and differentiating with respect to ω :

$$\left. \frac{dD}{d\omega} \right|_{\omega=\omega_R} = \frac{2\omega_R A [(\omega_0^2 - \omega_R^2) - 2\beta^2]}{[(\omega_0^2 - \omega^2)^2 + 4\omega_R^2 \beta^2]^{3/2}} \quad 2.59$$

Setting equation 2.59 to zero to satisfy the resonance condition:

$$0 = (\omega_0^2 - \omega_R^2) - 2\beta^2 \quad 2.60$$

The angular frequency at resonance is therefore:

$$\omega_R = \sqrt{\omega_0^2 - 2\beta^2} \quad 2.61$$

The corresponding quality factor and the amplitude of the resonant peak are as follows:

$$Q = \frac{\omega_R}{2\beta}, \quad Q \cong \frac{\omega_0}{\Delta\omega} \cong \frac{f_0}{\Delta f} \text{ (if lightly damped)} \quad 2.62$$

$$A_R = \frac{F_0/m}{2\beta\sqrt{\omega_0^2 - \beta^2}} \quad 2.63$$

2.3 Capacitive Detection and Actuation

As mentioned in the previous chapter, the method of torque detection is capacitive. Capacitor plates can be used in MEMS devices to actuate bridges and cantilevers, or they can be used as detectors [3]. Both situations are discussed below.

2.3.1 Capacitive Detection

The capacitance C between two parallel plates is given below [32]:

$$C = \frac{\epsilon_0 \epsilon_R A}{d} \quad 2.64$$

Where A is the surface area of the plate, d is the distance between the two plates, ϵ_R is the relative permittivity, and ϵ_0 is the permittivity of free space. If one of the plates is free to move, the capacitance change is therefore (with d_n being the new distance between the two plates, assuming $d_n < d$):

$$\Delta C = \epsilon_0 \epsilon_R A \left(\frac{1}{d_n} - \frac{1}{d} \right) \quad 2.65$$

The charge Q stored in a parallel plate capacitor is the multiple of the capacitance and the voltage V :

$$Q = CV \quad 2.66$$

The current flowing through a capacitor is the derivative of the charge with respect to time t [3]:

$$i = \frac{dQ}{dt} \quad 2.67$$

$$i = C \frac{dV}{dt} + V \frac{dC}{dt} \quad 2.68$$

For capacitance measurement, the second term in equation 2.68 can be dropped, reducing the equation to:

$$i = C \frac{dV}{dt} \quad 2.68$$

2.3.2 Capacitive Actuation

To show the force acting on a parallel plate capacitor, the energy stored in the parallel plates must first be determined. The energy stored in a capacitor is as follows [3, 32]:

$$W_C = \frac{1}{2}CV^2 \quad 2.70$$

Taking both equations 2.66 and 2.70 and differentiating with respect to C gives:

$$dW_C = \frac{1}{2}V^2 dC \quad 2.71$$

$$dQ_C = VdC \quad 2.72$$

The energy stored in the voltage supply is:

$$W_V = Q_V V \quad 2.73$$

Differentiating with respect to Q_V :

$$dW_V = VdQ_V \quad 2.74$$

Knowing that the charge in the voltage supply changes by:

$$dQ_V = -dQ_C \quad 2.75$$

Substituting equation 2.75 into 2.74, the energy stored in the voltage supply can be viewed as:

$$dW_V = -VdQ_C \quad 2.76$$

Therefore, the total change in electrical energy is given as follows:

$$dW_E = dW_V + dW_C \quad 2.77$$

$$dW_E = \frac{1}{2}V^2 dC - V(VdC) \quad 2.78$$

$$dW_E = -\frac{1}{2}V^2 dC \quad 2.79$$

Finally, given that the force can be determined from energy by the following relation:

$$F = -\frac{dW_E}{dx} \quad 2.80$$

The force acting on two parallel plates is therefore:

$$F = \frac{1}{2}V^2 \frac{dC}{dx} \quad 2.81$$

2.3.2.1 Using AC and DC Voltages

When using both AC and DC voltages for capacitive actuation, the force equation becomes (where the AC voltage is given as $v = v_0 \cos \omega t$) [3]:

$$F = \frac{1}{2}(V_{dc} + v_0 \cos \omega t)^2 \frac{dC}{dx} \quad 2.82$$

Expanding the bracket and using the trigonometric identity $\cos^2 \omega t = \frac{1}{2}(1 + \cos 2\omega t)$:

$$F = \frac{1}{2}(V_{dc}^2 + \frac{1}{2}v_0^2 + 2V_{dc}v_0 \cos \omega t + \frac{1}{2}v_0^2 \cos 2\omega t) \frac{dC}{dx} \quad 2.83$$

The first two voltage terms dominate for a DC drive, and the last two voltage terms dominate for an AC drive. Also, it is interesting to note that the AC current gives rise to a DC current of its own. The third and fourth terms are the voltages at the reference and at double the reference frequencies, respectively.

2.3.3 Pull-in Effect

When dealing with bridges and cantilevers electrostatically on the microscale, one needs to be aware of the pull-in effect. This occurs when the force due to the voltage applied becomes greater than the mechanical force. When that happens, the bridge or cantilever will snap down to the substrate, or to a nearby electrode.

The total force consists of the electrostatic and mechanical forces [3]:

$$F = F_e + F_m \quad 2.84$$

The mechanical force is found in Hooke's Law, given in equation 2.06. The electrostatic force is given below:

$$F_e = \frac{1}{2} \frac{\epsilon_0 \epsilon_R A}{(d-x)^2} V^2 \quad 2.85$$

Thus the total force is as follows:

$$F = \frac{1}{2} \frac{\epsilon_0 \epsilon_R A}{(d-x)^2} V^2 - kx \quad 2.86$$

At equilibrium, the total force is zero, and the equation can be arranged for the pull in voltage:

$$V_P = \sqrt{\frac{2kx_0(d-x_0)^2}{\epsilon_0 \epsilon_R A}} \quad 2.87$$

To find the pull in displacement, equation 2.86 is differentiated with respect to x and evaluated at the equilibrium point:

$$\left. \frac{dF}{dx} \right|_{x=x_0} = \frac{\epsilon_0 \epsilon_R A}{(d-x_0)^3} V_P^2 - k \quad 2.88$$

Equation 2.87 is substituted into equation 2.88:

$$\left. \frac{dF}{dx} \right|_{x=x_0} = \frac{2kx_0}{(d-x_0)} - k \quad 2.89$$

The pull in point occurs when the electrostatic force overcomes the mechanical force, thus setting equation 2.89 equal to zero:

$$0 = k \left(\frac{2x_0}{d-x_0} - 1 \right) \quad 2.90$$

When the stiffness reaches zero, the pull in displacement is therefore:

$$x_P = \frac{1}{3} d \quad 2.91$$

Substituting this result into equation 2.87, the pull in voltage is therefore: [3]

$$V_P = \sqrt{\frac{8}{27}} \sqrt{\frac{kd^3}{\epsilon_0 \epsilon_R A}} \quad 2.92$$

Thus applying a voltage at or higher than the pull-in voltage will cause mechanical failure.

2.4 Magnetism

A very basic introduction on magnetism will be given in this section. In the study of superconductors, the properties of magnetization and susceptibility are important. When it comes to magnetism, scientists have traditionally used the centimetre-gram-second system of units (cgs) as well as the more widely known international system of units (SI). In this section, all definitions are given in cgs units.

2.4.1 Magnetization and Magnetic Fields

Figure 2.07 is an image of a simple bar magnet along with its generated magnetic field. The force F that the bar magnet exerts is given as follows, where p is the pole strength, H is the field intensity, and k is the inverse of the current flux. [11, 14]:

$$F = kpH \quad 2.93$$

The field intensity of the bar magnet is dependent on the pole strength and the distance d from the bar magnet:

$$H = \frac{p}{d^2} \quad 2.94$$

When a bar magnet is placed in a uniform magnetic field, forces will be exerted on the two ends of the bar magnet such that the bar magnet will be rotated to align with the magnetic field, as shown in Figure 2.08.

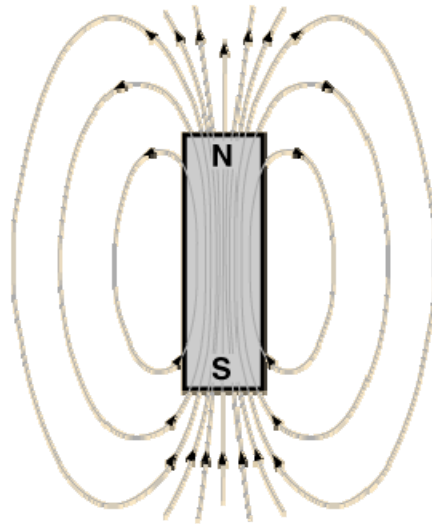


Figure 2.07: A diagram illustrating the direction of the magnetic field lines of a simple bar magnet [33].

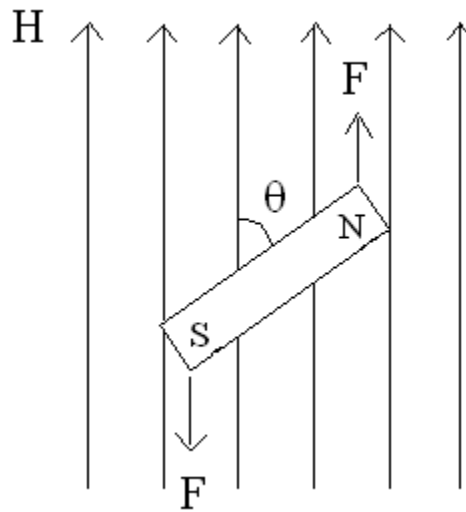


Figure2.08: Schematic of the reaction of a bar magnet in a uniform magnetic field.

If the field intensity is 1, and the angle θ the bar magnet initially makes with the field intensity is 90° , the magnetic moment of the bar magnet is given below, where l is the length of the bar magnet [11, 14]:

$$m = pl \qquad 2.95$$

The magnetization of a bar magnet or of a magnetic material is the magnetic moment per unit volume V :

$$M = \frac{m}{V} \quad 2.96$$

The relationship between the field intensity and the magnetization of a magnetic material, or how the magnetization varies with the field intensity, is given as follows (where χ is the susceptibility):

$$\chi = \frac{M}{H} \quad 2.97$$

This relationship varies with different magnetic materials, and is important in the study of superconductors. The magnetic flux density is related to the field intensity as follows (where μ is the magnetic permeability):

$$\mu = \frac{B}{H} \quad 2.98$$

2.4.1.1 Current Carrying Coils

The magnetic field B produced by a current carrying loop of radius R at a point x as shown in Figure 2.09 can be derived by the Biot-Savart Law and is given as follows (where I is the current and μ_0 is the permeability of free space) [32, 34]:

$$B = \frac{\mu_0 I R^2}{2(x^2 + R^2)^{3/2}} \quad 2.99$$

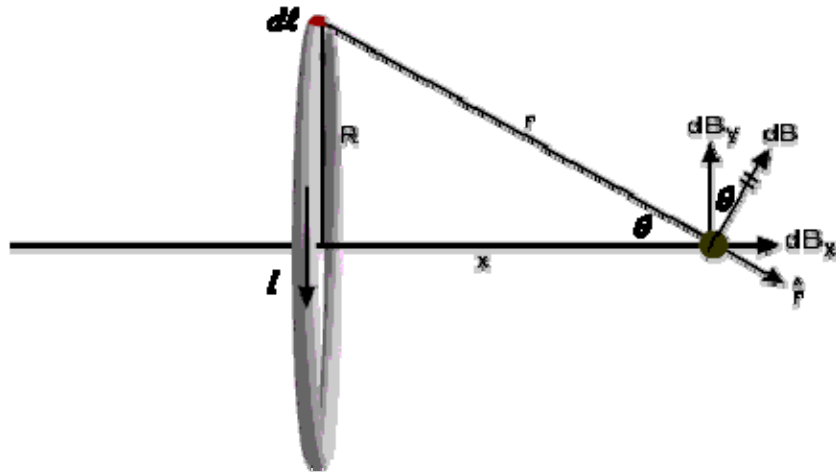


Figure 2.09: A current carrying loop [35].

At the center of the loop, where x is zero, the magnetic field is:

$$B = \frac{\mu_0 I}{2R} \quad 2.100$$

A tightly wound coil of wire consisting of N loops over a length L is called a solenoid. If the solenoid is of a finite length L , it can be approximated as a stack of current carrying loops. In this situation, the magnetic field at a point x along the length axis is [36]:

$$B = \frac{\mu_0 IN}{2} \left(\frac{L/2 - x}{\sqrt{(x - L/2)^2 + R^2}} + \frac{L/2 + x}{\sqrt{(x + L/2)^2 + R^2}} \right) \quad 2.101$$

From this relationship, the magnetic field at various points along the solenoid can be derived. At the midpoint of the solenoid (where x is zero), the magnetic field is therefore:

$$B = \frac{\mu_0 IN}{2} \left(\frac{L}{\sqrt{(L/2)^2 + R^2}} \right) \quad 2.102$$

For an infinite solenoid where $L \gg R$, equation 2.101 is further reduced to:

$$B = \frac{\mu_0 IN}{L} \quad 2.103$$

Moving outside of the solenoid along the length axis, the magnetic field decreases and eventually reaches zero.

2.4.2 Torque

There is a simple relation for the torque between a magnetized sample and the magnetic field applied to that sample. Using an example of a bar magnet glued to a beam shown in Figure 2.10, the torque of the bar magnet can be calculated.

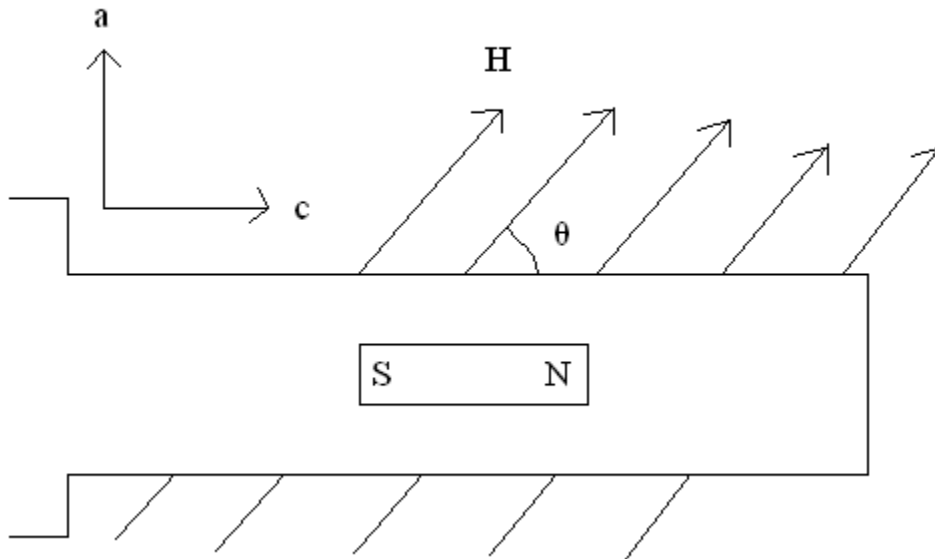


Figure 2.10: Bar magnet glued to a cantilever, and subjected to a magnetic field of intensity H .

The applied magnetic field of magnetic flux B is parallel to the surface of the beam [10]:

$$\vec{B} = B \sin \theta \hat{a} + B \cos \theta \hat{c} \quad 2.104$$

Therefore, the magnetization M of the sample is as follows:

$$\vec{M} = M_a \hat{a} + M_c \hat{c} \quad 2.105$$

According to equation 2.98, $B = \mu H$. Thus $M = \frac{\chi}{\mu} B$. Substituting this into equation 2.105:

$$\vec{M} = \frac{1}{\mu} (\chi_a B \sin \theta \hat{a} + \chi_c B \cos \theta \hat{c}) \quad 2.106$$

Using equations 2.104 and 2.106, the torque τ applied to the beam can be calculated as follows [11, 14, 33]:

$$\tau = \vec{M} \times \vec{B} \quad 2.107$$

$$\tau = (\hat{b}_1 \hat{c}_2 - \hat{c}_1 \hat{b}_2) \hat{a} + (\hat{a}_1 \hat{c}_2 - \hat{c}_1 \hat{a}_2) \hat{b} + (\hat{b}_1 \hat{a}_2 - \hat{a}_1 \hat{b}_2) \hat{c} \quad 2.108$$

$$\tau = \frac{B^2}{\mu} \sin \theta \cos \theta (\chi_a - \chi_b) \hat{b} \quad 2.109$$

Thus torque is directly proportional to the susceptibility change of the sample.

2.5 Electrostatic Determination of Torque

A simple way of extracting magnetization and susceptibility data from a sample is to measure its torque as a result of a magnetic field. If the torque is known, the unknown properties of that sample (namely its magnetization and susceptibility) can be determined.

2.5.1 Mechanical Torque

Mechanically, torque is given by the simple equation [32]:

$$\tau = r \times F \quad 2.110$$

where r is the radius of the torque arm. If the force is applied over a range of points, it is more convenient to start with torque as an integral:

$$\tau = \int r \cdot dF \quad 2.111$$

$$dF = \frac{F}{L} dr \quad 2.112$$

with L being the length over which the force is applied. Substituting equation 2.112 into equation 2.111 and integrating with limits of r_1 and r_2 :

$$\tau = \frac{F}{L} \int_{r_1}^{r_2} r \cdot dr \quad 2.113$$

Solving the integral produces:

$$\tau = \frac{F}{L} \left(\frac{r_2^2 - r_1^2}{2} \right) \quad 2.114$$

2.5.2 Magnetic and Mechanical Torque

If there is a sample attached to a beam similar to the scenario laid out in Section 2.4.2, and a magnetic field is applied to that sample, it will exert a torque upon the beam. The magnetic field causes the magnetic moments inside the sample to exert a torque on the sample, which in turn exerts a torque on the beam. Thus the magnetic and mechanical torques are linked. The mechanical torque results in a displacement of the beam. If the beam is one plate in a pair of parallel plates (with the other plate being below the beam), then the displacement of the beam results in a capacitance change. The amount of capacitance change depends on the magnetic field strength. Therefore, by applying a known magnetic field to a sample and measuring the capacitance change, certain magnetic properties such as the magnetization and susceptibility of the sample can be extracted.

3. Numerical Analyses

In this chapter, the design and numerical analyses of the torque magnetometer will be covered. All numerical analyses were performed using ANSYS (version 13.0), an engineering simulation software which uses the finite element method. Two analyses will be explained in this chapter – modal and structural analysis. Modal analysis is concerned with frequency modes corresponding to different models of the torque magnetometer. Structural analysis involves the estimation of the bridge displacements. Numerical analyses are useful in determining the ideal design and dimensions of the torque magnetometer.

3.1 Design

Very simply, the idea of the torque magnetometer investigated here is a circular platform with four bridges extending from it to four corners. At these corners, the bridges are fixed – so when the platform rotates, the bridges deflect evenly. When performing numerical analyses on the torque magnetometer, the dimensions (width, length, thickness) of the bridges and platform as well as electrode placements were varied. From the results of those analyses, the most ideal design for our purposes was determined, with the purposes being to build a MEMS torque magnetometer for magnetic crystal research that has the potential of being more sensitive than previously fabricated MEMS torque magnetometers.

3.1.1 Original Model

A diagram of the first model of the torque magnetometer that was fabricated is shown in Figure 3.01. All corner supports and electrodes are fully supported, and the bridge and platform are freestanding as illustrated in Figure 3.02. The dimensions of this model are given in Table 3.01.

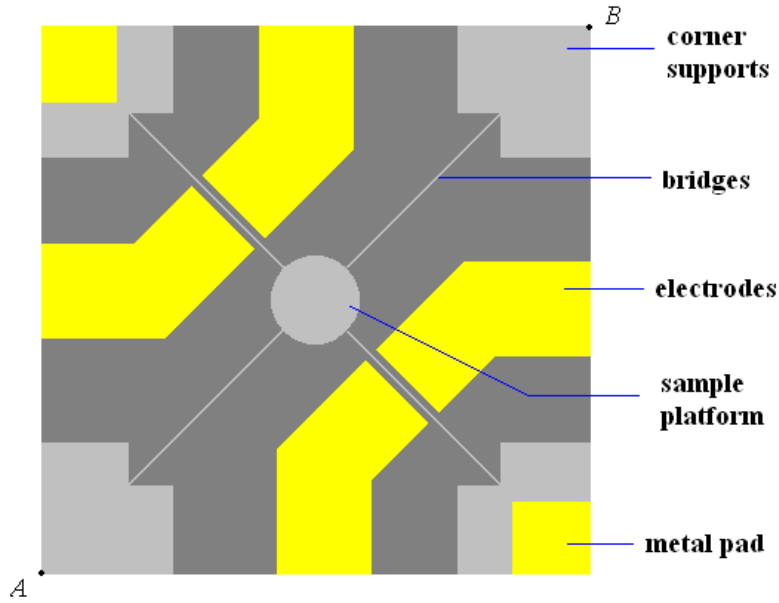


Figure 3.01: The original layout of the torque magnetometer. The light grey, dark grey, and yellow represent the device layer, the substrate, and the gold pads, respectively.

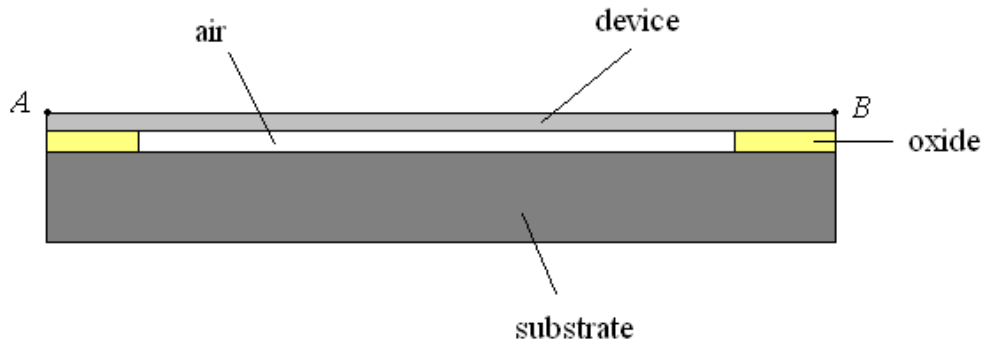


Figure 3.02: Side view of the torque magnetometer

Table 3.01: Torque magnetometer material dimensions and properties

Dimensions/Properties	Values
Width of bridge	5, 10, 15 μm
Thickness of device	50 μm
Length of bridge	5 mm
Distance between bridge and electrode	5, 10 μm

Diameter of platform	2 mm
Poisson's ratio	0.09
Density	2330 kg/m ³
Young's modulus	1.5 X 10 ⁹ Pa

3.1.2 Improved Model

For reasons that will be discussed in the next chapter, the improved model of the torque magnetometer has a perforated platform as shown in Figure 3.03. The dimensions of the device are the same as the original model, with the 100 μm diameter holes in the platform hexagonally arranged (200 μm spacing).

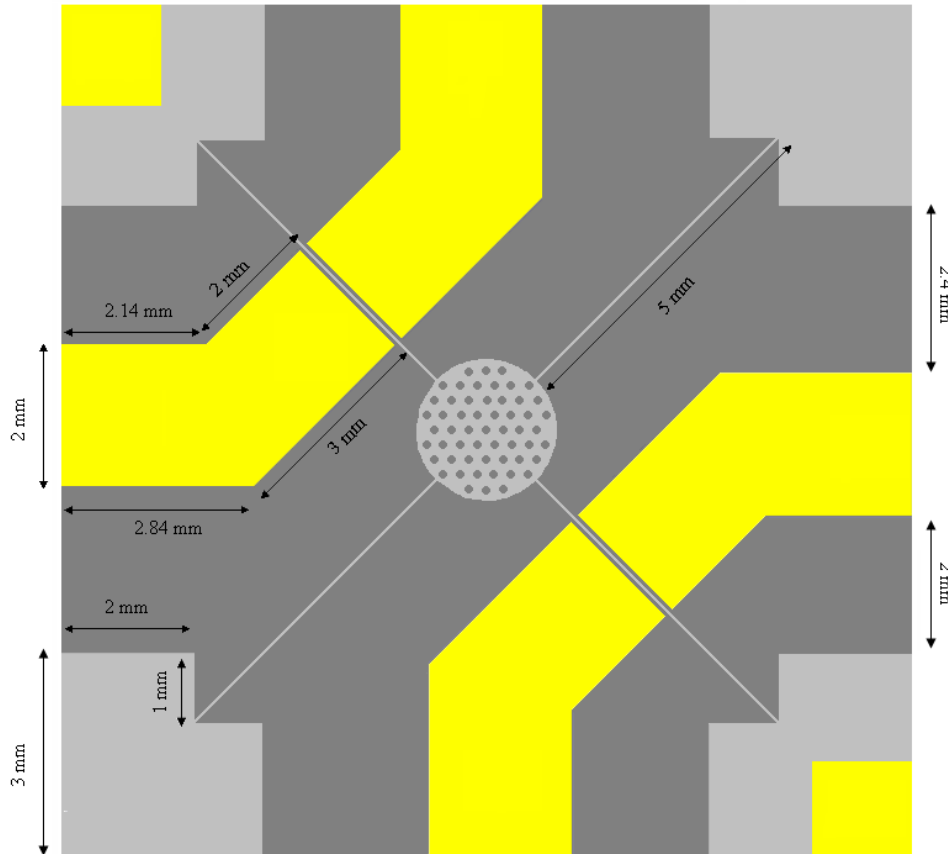


Figure 3.03: Improved layout of the torque magnetometer, with the 100 μm holes arranged hexagonally in the platform (200 μm spacing)

3.2 Modal Analysis

The torque magnetometer (like other objects) has higher order resonant frequency modes in addition to the fundamental mode. By using the finite element method, ANSYS can generate a certain number of modes for a particular model with specific dimensions – in this project ten were generated for each model [37].

3.2.1 Original Model

Using the dimensions found in Table 3.01 (with width being 5 μm), the first ten resonant frequency modes of the original model were generated by ANSYS and are given in Table 3.02. Images of the first two modes are shown in Figures 3.04 and 3.05 respectively, where the four bridges are fixed at the four ends. The first mode is rotational, where the platform rotates slightly, causing all four bridges to deflect symmetrically. The second mode is the in and out of plane mode, where the entire device oscillates along the thickness direction. The sixth mode is the second order rotational mode, and the seventh and eighth modes are the second order in and out of plane modes. Modes three, four, and five are modes in which the platform does not move and the bridges vibrate – corresponding to the standard first order bridge (fixed-fixed beam) mode. The second order modes of these are found in modes nine and ten (and presumably eleven).

Table 3.02: A list of modes and their corresponding resonant frequencies ($w = 5 \mu\text{m}$)

Mode	Resonant Frequency (Hz)	Mode
1	235.45	Rotational
2	451.12	In and out of plane
3	1649.1	Bridge
4	1649.1	Bridge
5	1649.2	Bridge
6	1687.5	2 nd order rotational
7	2346.9	2 nd order in and out of plane
8	2347.0	2 nd order in and out of plane
9	4545.6	2 nd order bridge
10	4545.8	2 nd order bridge

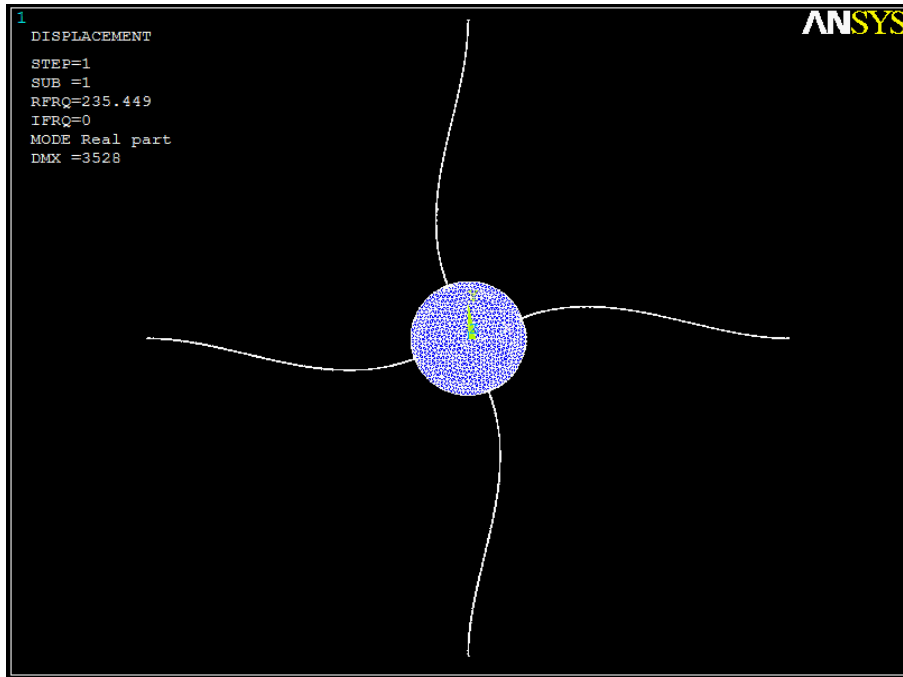


Figure 3.04: Original torque magnetometer rotational (1st) mode



Figure 3.05: Original torque magnetometer in-out of plane (2nd) mode, side view

Analytically, the resonant frequencies of the first two modes can be determined using the relationships derived in the previous chapter. In the rotational mode, there is both an axial and a transverse load acting upon the bridges. From equations 2.07 and 2.39, the approximate combined stiffness is therefore:

$$k_R \approx \frac{EA}{L} + \frac{3EI}{L^3} \quad 3.01$$

According to the dimensions given in the schematic of the bridge displayed in Figure 3.06, the area A is wt . Substituting this as well as equation 2.40 into equation 3.01:

$$k_R \approx E \left(\frac{tw}{L} + \frac{tw^3}{4L^3} \right) \quad 3.02$$

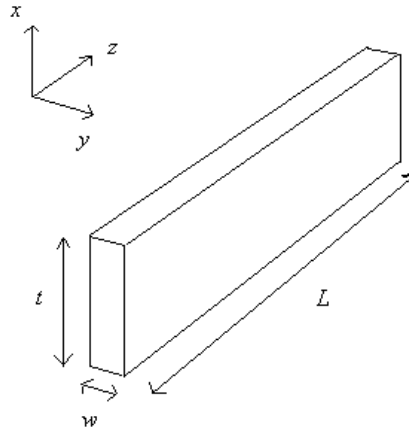


Figure 3.06: Dimensions of beam, with t being the thickness, w being the width, and L being the length

Using the relationships in equations 2.44 and 2.48, the resulting rotational frequency is:

$$f_R \approx \frac{1}{2\pi\sqrt{m}} \sqrt{E \left(\frac{tw}{L} + \frac{tw^3}{4L^3} \right)} \quad 3.03$$

Remembering that mass is a function of density and volume (with the overall volume V being dominated by the platform volume, $\pi r^2 t$):

$$f_R \approx \frac{1}{2\pi} \sqrt{\frac{E}{\rho\pi r^2}} \sqrt{\frac{w}{L} + \frac{w^3}{4L^3}} \quad 3.04$$

Letting constant $A = \frac{1}{2\pi} \sqrt{\frac{E}{\rho\pi r^2}}$ and $c = \frac{1}{4}$, equation 3.04 can be re-written as:

$$f_R \approx A \sqrt{\frac{w}{L} + c \frac{w^3}{L^3}} \quad 3.05$$

Keeping the width and thickness of the bridge constant while varying the length, five torque magnetometer models were analyzed on ANSYS (no changes were made to the platform). Taking the rotational frequency from each of them, a plot of rotational frequency versus length was produced, shown in Figure 3.07. The plots displayed in Figures 3.08 and 3.09 were produced in a similar way, varying the thickness and widths instead. These plots confirm the approximation in equation 3.05.

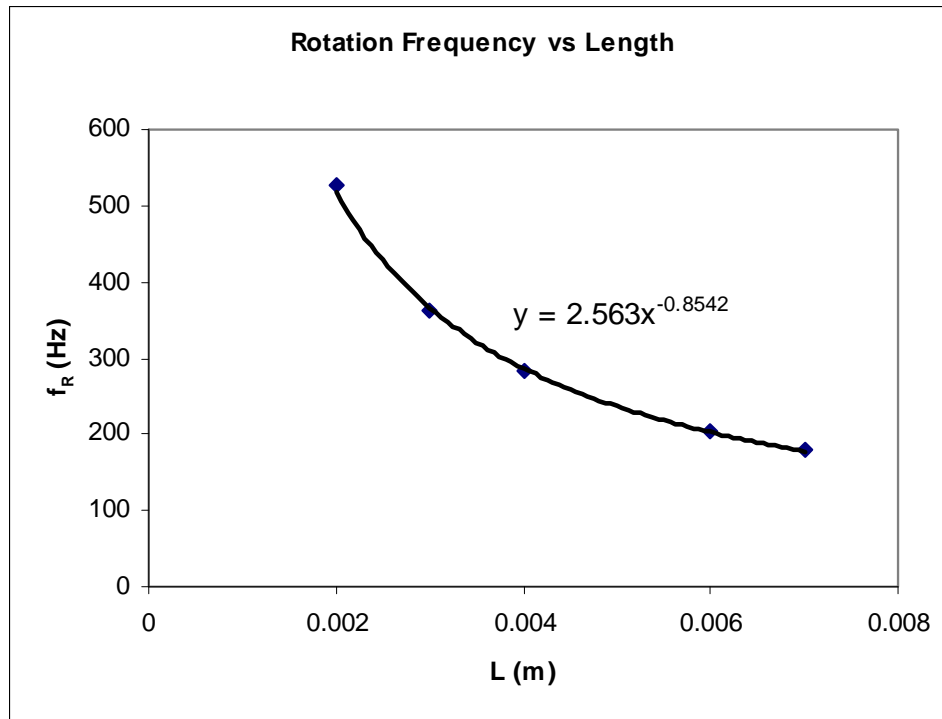


Figure 3.07: Plot of rotational frequency versus length for original torque magnetometer, obtained from ANSYS

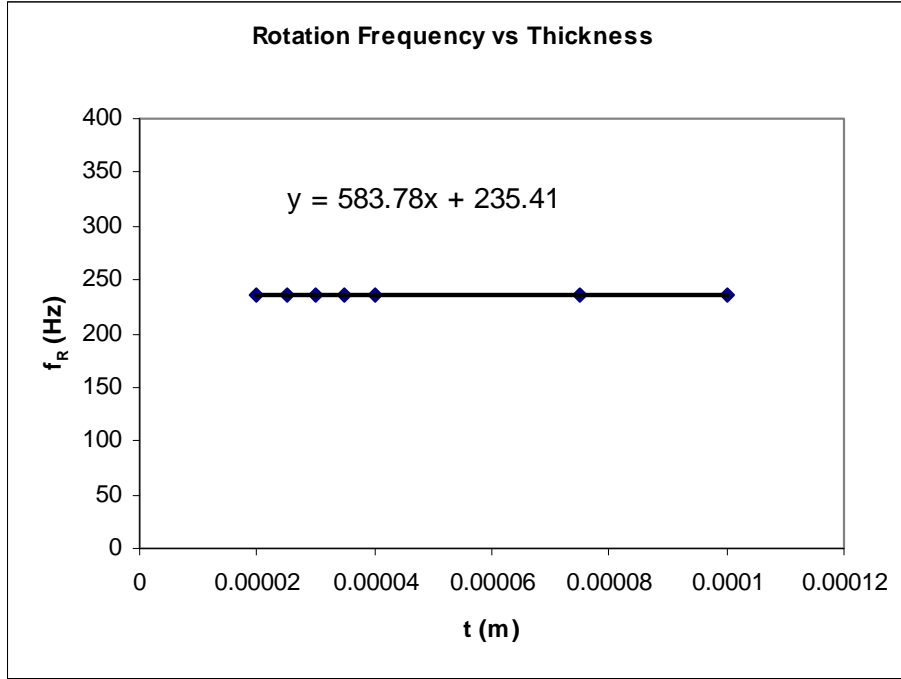


Figure 3.08: Plot of rotational frequency versus thickness for original torque magnetometer, obtained from ANSYS

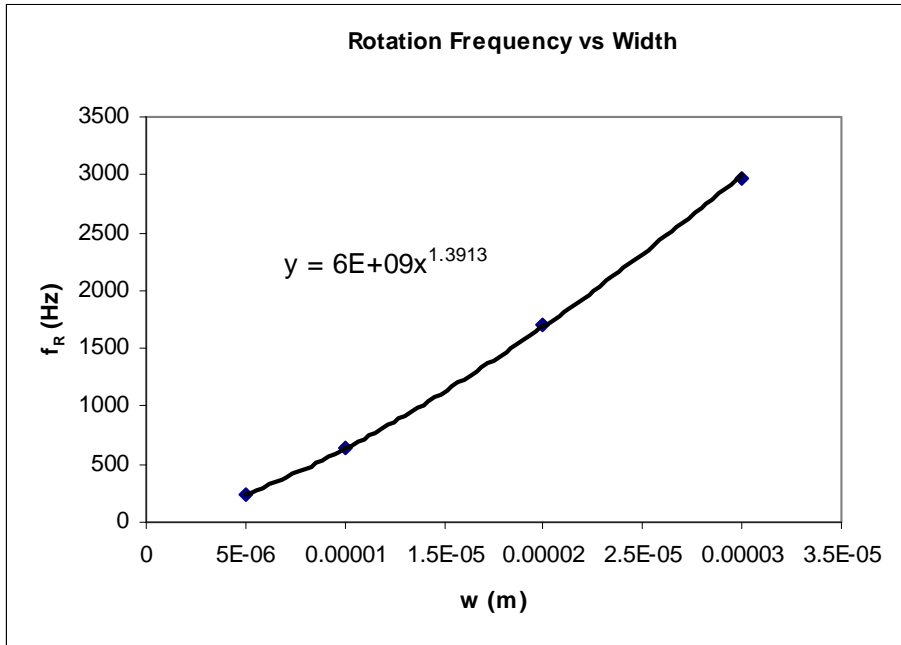


Figure 3.09: Plot of rotational frequency versus width for original torque magnetometer, obtained from ANSYS

In the in and out of plane mode, only a transverse force is acting upon the bridges (the axial force is insignificant):

$$k_I \approx \frac{3EI}{L^3} \quad 3.06$$

The moment of inertia for the in and out of plane mode changes from equation 2.40 to:

$$I = \frac{wt^3}{12} \quad 3.07$$

Thus the resulting stiffness is:

$$k_I \approx \frac{Ewt^3}{4L^3} \quad 3.08$$

The corresponding frequency can be determined:

$$f_I \approx \frac{1}{2\pi\sqrt{m}} \sqrt{E \frac{wt^3}{4L^3}} \quad 3.09$$

$$f_I \approx \frac{1}{2\pi} \sqrt{\frac{E}{\rho\pi r^2}} \sqrt{\frac{wt^2}{4L^3}} \quad 3.10$$

$$f_I \approx A\sqrt{c \frac{wt^2}{L^3}} \quad 3.11$$

From the same analyses used to generate the first three frequency plots, the in and out of plane modes were taken and used to produce the plots shown in Figures 3.10, 3.11, and 3.12. These plots also confirm the result found in equation 3.11.

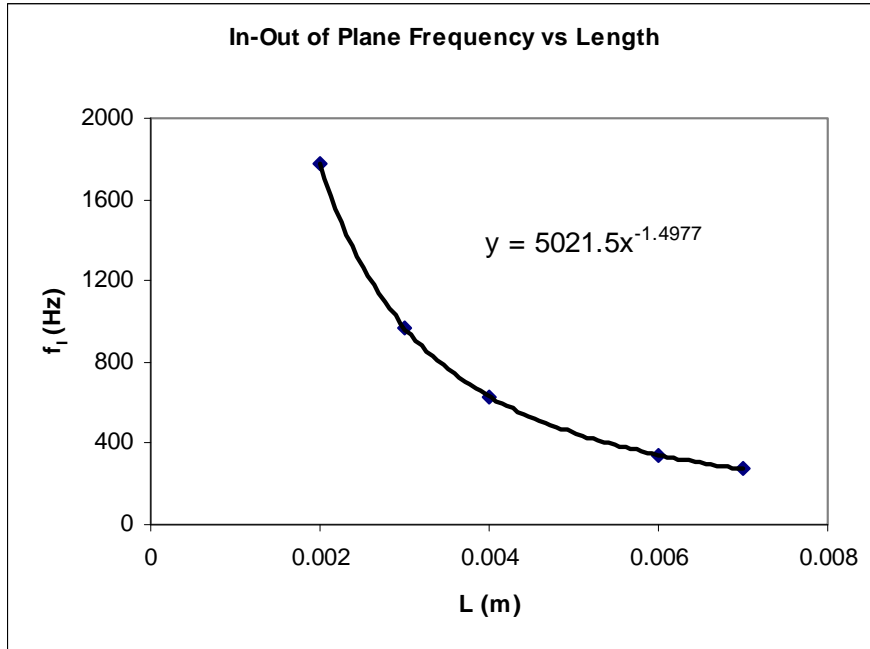


Figure 3.10: Plot of in-out of plane frequency versus length for original torque magnetometer, obtained from ANSYS

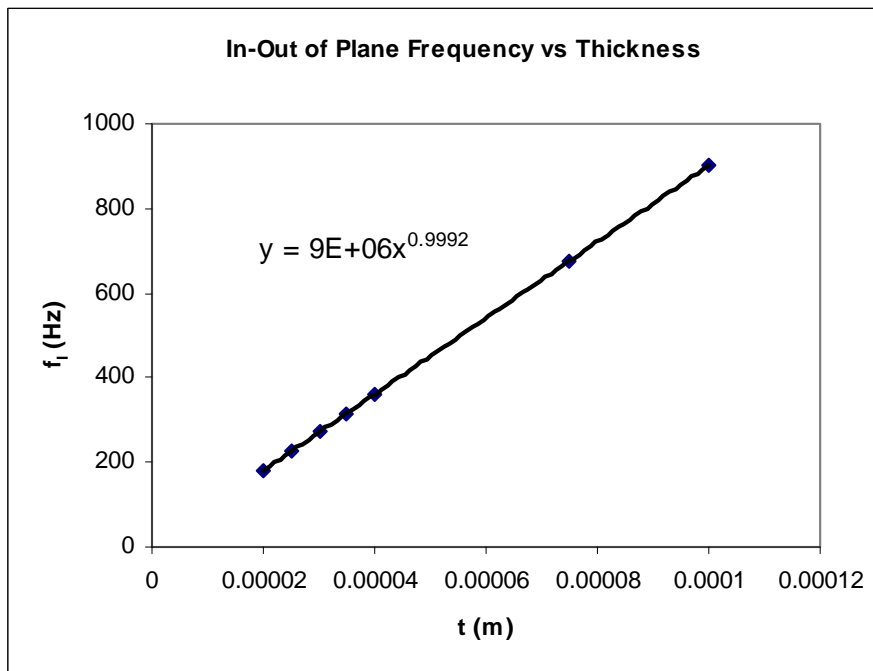


Figure 3.11: Plot of in-out of plane frequency versus thickness for original torque magnetometer, obtained from ANSYS

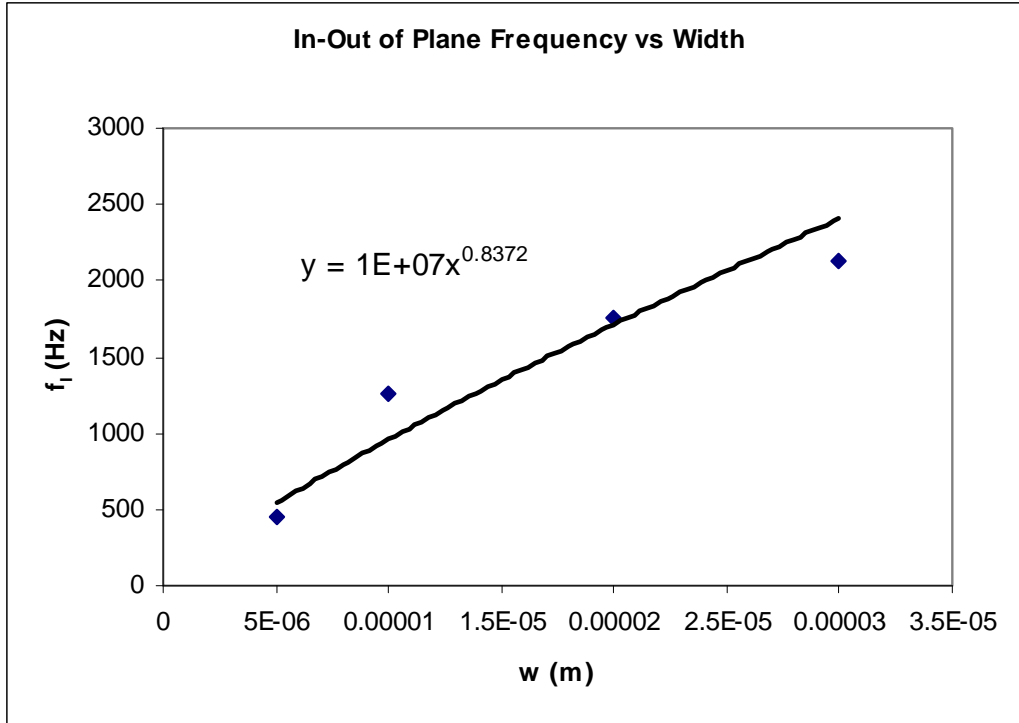


Figure 3.12: Plot of in-out of plane frequency versus width for original torque magnetometer, obtained from ANSYS

Using equations 3.03 and 3.09, the ratio of the in and out of plane mode to the rotational mode is as follows:

$$\frac{f_I}{f_R} \approx \sqrt{\left(\frac{(t/L)^2}{c(t/L/t/w)^2 + 1} \right)} \quad 3.12$$

Having arranged the frequency ratio in equation 3.12 as a function of t/w and t/L , a contour plot incorporating the relationships is given in Figure 3.13. The three lines represent three different values of L/w . The two dots correspond to a torque magnetometer with the dimensions found in Table 3.01, with the black dot being the model with $w = 5 \mu m$, and the grey dot being the model with $w = 10 \mu m$.

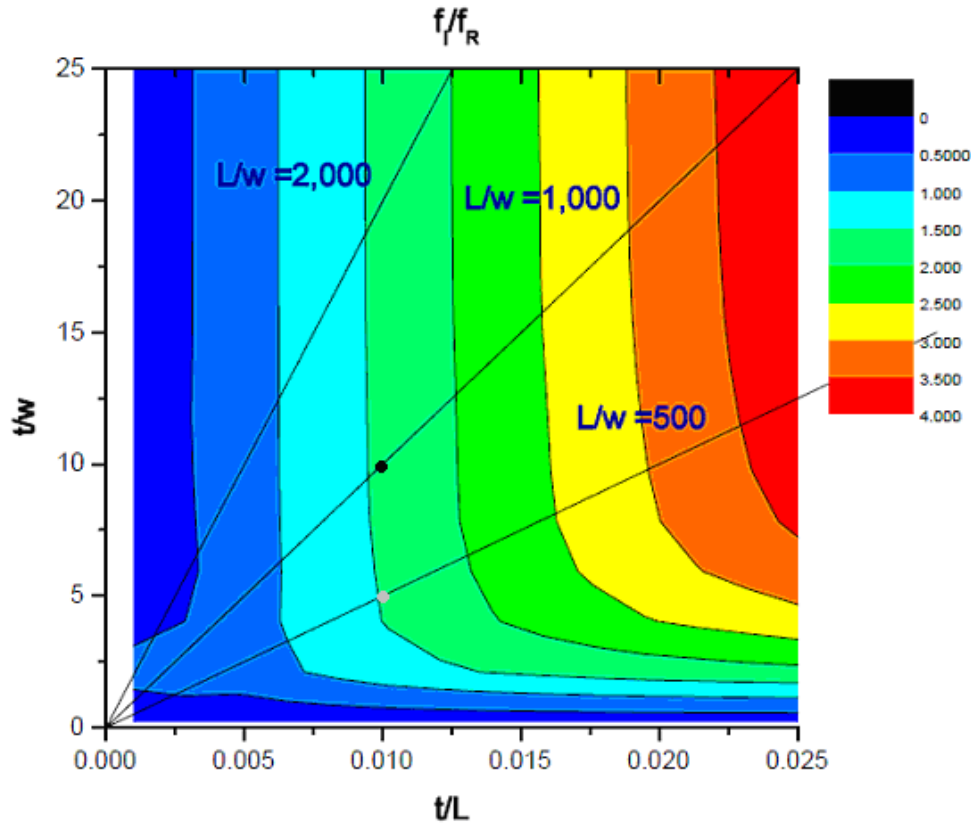


Figure 3.13: Contour plot of f_i/f_R for different dimensional ratios. The black and grey dots correspond to a torque magnetometer with the dimensions found in Table 3.01, with $w = 5 \mu\text{m}$ and $w = 10 \mu\text{m}$, respectively.

Given a certain frequency ratio, the contour plot can be used to determine what dimensions the torque magnetometer can have (or vice versa). Since the purpose of the torque magnetometer depends on its ability to rotate, having the rotational mode as the fundamental mode is desired. Thus, a frequency ratio of two would be sufficient to separate the fundamental mode from the second order mode. For a torque magnetometer with the particular dimensions given in Table 3.01 ($w = 5 \mu\text{m}$), ANSYS gives a frequency ratio of 1.92. For the same torque magnetometer, the contour plot gives a ratio of ~ 1.6 , which is relatively close to the value given by ANSYS. While designing a chrome on glass mask for photolithography, several variations of the bridge width and the distances between the bridge and electrode (gap) were incorporated for flexibility. Bridge widths chosen were 5, 10, and 15 μm , and the gap varied between 5 and 10 μm (as given in Table 3.01). Due to a miscommunication, the 5 μm width bridges did not appear on the chrome glass mask, thus patterns with 10 μm bridges were used. ANSYS simulations were run to gauge the effect this would have on the resonant

frequencies, and the results are listed in Table 3.03. According to this table, the frequency ratio of the in and out of plane mode to the rotational mode is 0.98. The contour plot gives a ratio of ~ 1.5 , which is still relatively close to the numerical data.

According to equation 3.05, doubling the width of the bridge (from 5 to 10 μm) would result in the following effect:

$$f_{R2} \sim A \sqrt{\frac{(2w)}{L} + c \frac{(2w)^3}{L^3}} \quad 3.13$$

Doubling of the width has a greater effect on the second term; thus the first term can be ignored for the time being:

$$f_{R2} \sim 2\sqrt{2} \cdot f_R \quad 3.14$$

This result is not fully accurate, but does predict a value close to the one found in Table 3.03, corresponding to the second mode. The first mode in said table corresponds to the in and out of plane mode, and is well within the range predicted by equation 3.11:

$$f_{I2} \sim A \sqrt{c \frac{(2w)t^2}{L^3}} \quad 3.15$$

$$f_{I2} \sim \sqrt{2} \cdot f_I \quad 3.16$$

Doubling the bridge width has a significant effect on the order and values of the frequency modes (shown in Table 3.03), as expected. The first mode that appears is now the in and out of plane mode, with the rotational mode following as a close second. Modes three and four are the second order in and out of plane modes, and the eighth mode is the second order rotational mode. Modes five, six, seven, nine, and ten give the same mode shapes as modes three, four, five, nine, and ten in Table 3.02, respectively.

Table 3.03: A list of modes and their corresponding resonant frequencies ($w = 10 \mu\text{m}$)

Mode	Resonant Frequency (Hz)	Mode
1	632.55	In and out of plane
2	643.61	Rotational
3	3213.5	2 nd order in and out of plane
4	3213.6	2 nd order in and out of plane
5	3296.7	Bridge

6	3296.8	Bridge
7	3297.0	Bridge
8	3447.3	2 nd order rotational
9	9087.1	2 nd order bridge
10	9087.3	2 nd order bridge

3.2.2 Improved Model

Adding holes to the platform does not significantly affect either the values of the frequency modes or the order, because the modes are largely dependent on the bridge dimensions. The modes are listed in Table 3.04, with the order being the same as the modes in Table 3.03. The greatest change from Table 3.03 to Table 3.04 is an increase of 30 Hz.

Table 3.04: A list of modes and their corresponding resonant frequencies ($w = 10 \mu\text{m}$, perforated platform)

Mode	Resonant Frequency (Hz)	Mode
1	662.89	In and out of plane
2	668.44	Rotational
3	3297.0	2 nd order in and out of plane
4	3297.1	2 nd order in and out of plane
5	3297.3	Bridge
6	3335.0	Bridge
7	3338.6	Bridge
8	3460.8	2 nd order rotational
9	9087.8	2 nd order bridge
10	9088.6	2 nd order bridge

3.3 Structural Analysis

A modal analysis in ANSYS is very useful in providing images, but it is not quantitative in terms of displacement. To determine the displacement of the bridges, a structural analysis was completed. By applying a constant force to one fifth of the bridge length (keeping the ends fixed), as demonstrated by the red arrows in Figure 3.14, a theoretical scenario of how the torque magnetometer moves is established.

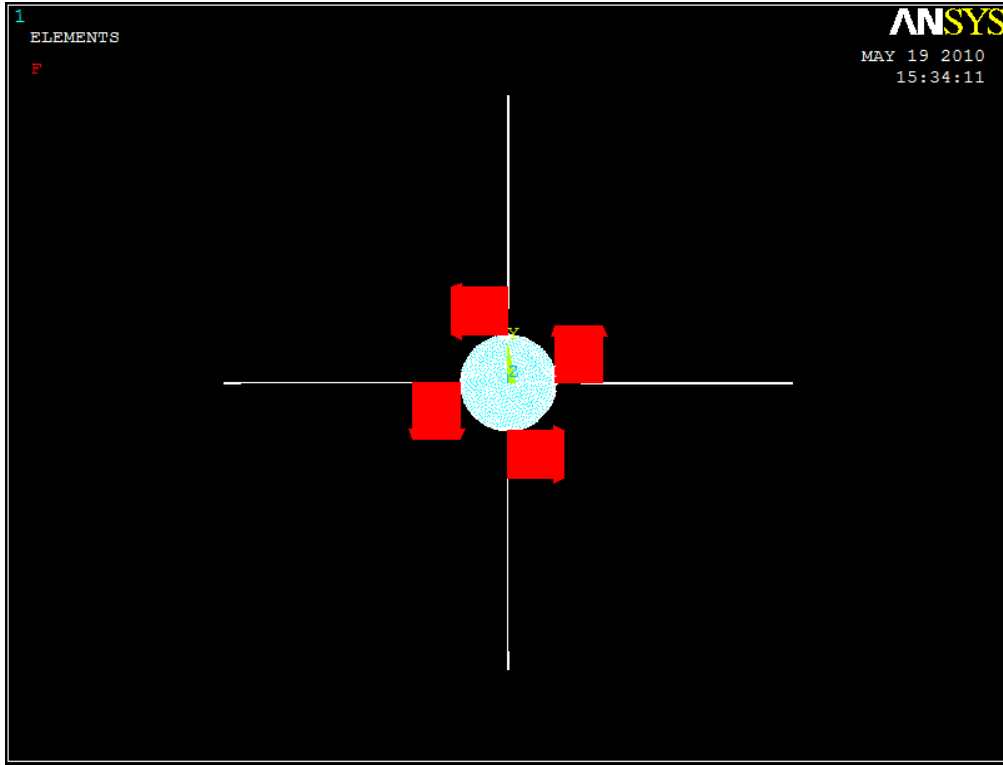


Figure 3.14: Forces applied counter-clockwise to torque magnetometer model, in theoretical representation of how actual forces would be applied

The contour plots of the rotating torque magnetometer showing the quantitative bridge displacements are shown in Figures 3.15 and 3.16, along with the original structure. Interestingly, contour circles on the platform indicate that the platform is being stretched. However, further analysis proved the stretching to be highly insignificant in comparison to the displacement of the bridges.

Using equation 2.114, the torque exerted on the torque magnetometer as a result of the forces can be calculated (r_1 and r_2 are 1 mm and 2 mm, respectively). Thus a direct correlation can be drawn between the torque exerted and the amount of bridge deflection. For different values of force applied, varying amounts of bridge deflection were extracted. A plot incorporating torque and bridge deflection is displayed in Figure 3.17. From that graph, a linear relationship between torque and bridge deflection B_d is given:

$$B_d = 2 \times 10^6 \tau \tag{3.17}$$

For a torque of 1.5×10^{-13} N-m (from a 1×10^{-10} N force), the corresponding bridge deflection is 300 nm. Using equation 2.65 to calculate the capacitance change (with $A = 2\text{mm} \times 50 \mu\text{m}$, $d = 5 \mu\text{m}$), the result is 10 fF. A capacitance

change lower than 10 fF would be extremely hard to detect, thus a torque of 1.5×10^{-13} N-m or greater needs to be exerted for a detectable signal to occur.

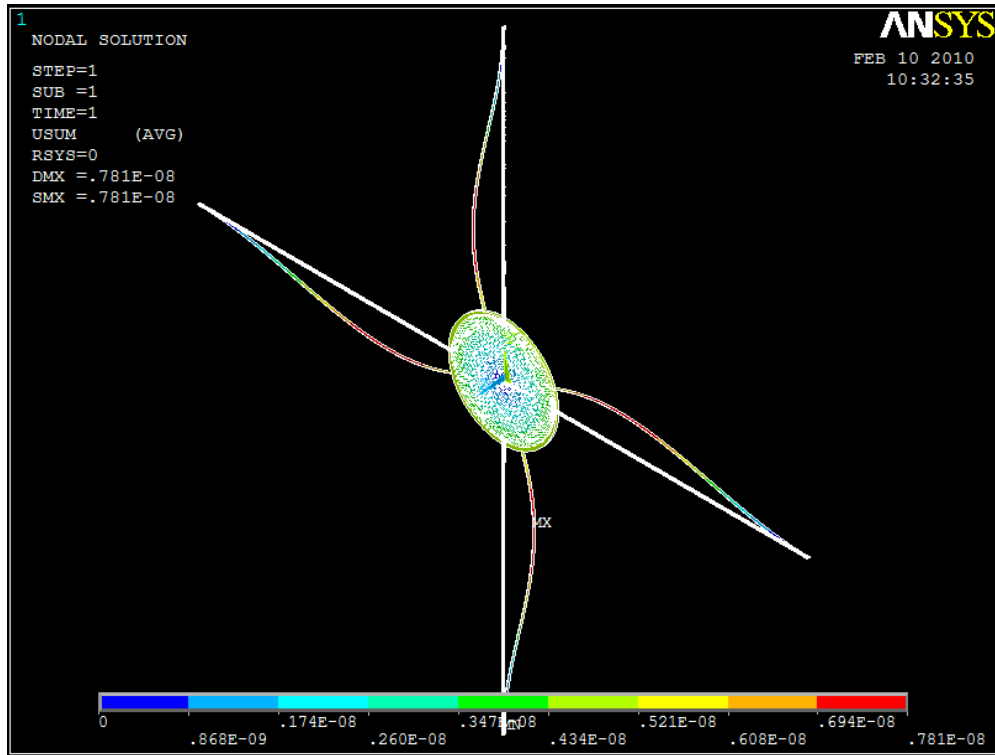


Figure 3.15: Displacement contour plot of torque magnetometer model, showing the amount of deflection of each bridge

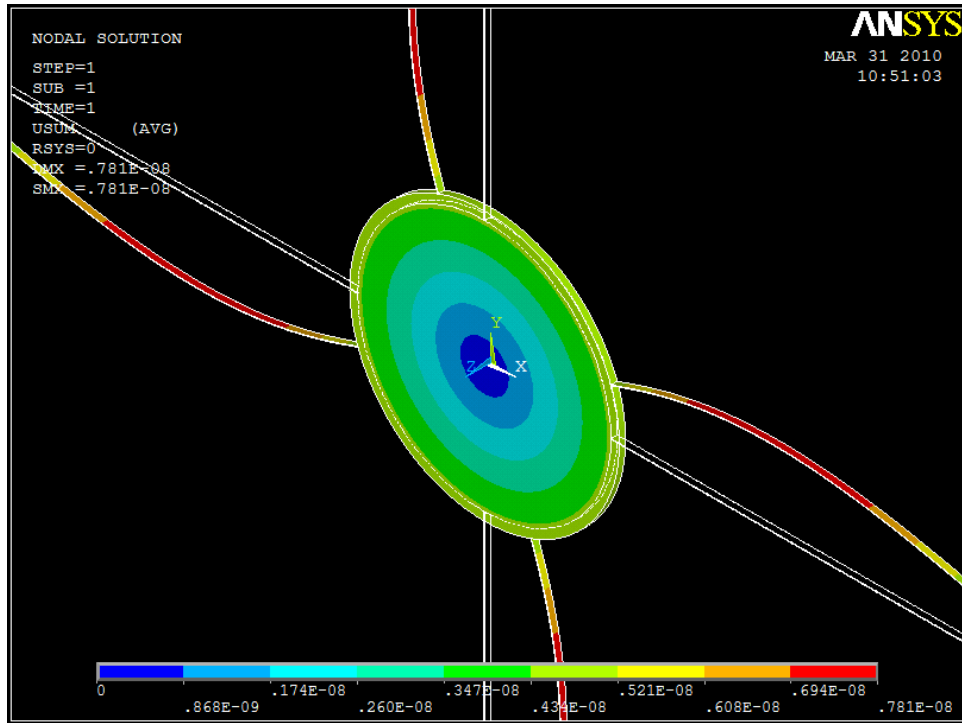


Figure 3.16: Close up of displacement contour plot, without mesh

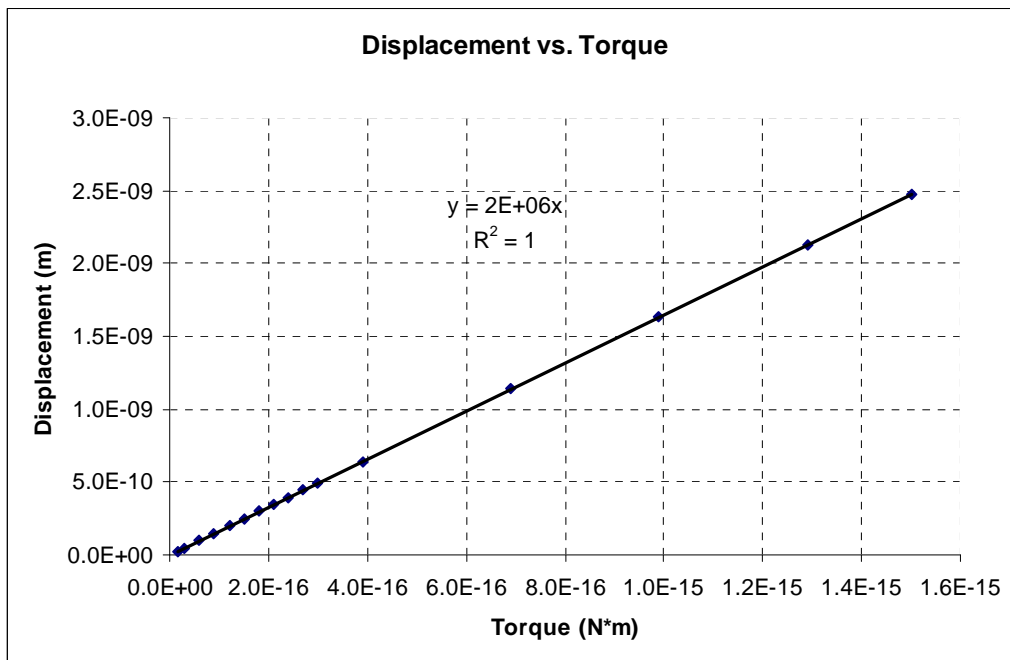


Figure 3.17: Plot of displacement of bridge versus torque applied to platform, obtained from ANSYS

Electrode size and placement were balanced between detectability and the constraints of the device. Ideally, the electrodes should be placed as close as possible to the bridge for greater detection, but far enough away so that the pull-in voltage is higher than what is required for the electrical experiments. The ends of the electrodes reach the edges of the device so that connections can be made easily.

3.4 Pull-in Voltage

To find the pull-in voltage, the stiffness of the rotational mode is required. Using the information from Tables 3.01 and 3.04 and equation 2.44, the approximate stiffness of the rotational mode can be calculated. The results are given below:

$$\begin{aligned} V &= \pi r^2 t + 4wtL \\ V &= 1.67 \times 10^{-10} \text{ m}^3 \end{aligned} \quad 3.18$$

$$m = 3.89 \times 10^{-7} \text{ kg} \quad 3.19$$

$$k_R = 0.174 \text{ N-m} \quad 3.20$$

Therefore, the approximate pull-in voltage for the rotational mode is:

$$V_p = 2.62 \text{ V} \quad 3.21$$

Using this value of voltage and a capacitance of 10 fF, the charge stored in the capacitor plates according to equation 2.66 is calculated to be 2.62×10^{-14} C. The noise floor of the Amptek (an amplifier used in electrical experiments) is 1.6×10^{-17} C. Using the pull-in voltage and the lowest detectable capacitance value, the resulting charge is well above the noise floor of the amplifier. Thus lowering the voltage by an order or two of magnitude will still result in a charge that can be detected.

4. Fabrication

Determining the fabrication process flow for the torque magnetometer was interesting and challenging. Given that the torque magnetometer has macro and micro features, certain challenges appeared that were eventually overcome. This chapter provides a general outline of the fabrication process, expands on lessons learned from early attempts, and concludes with the steps involved in the successful procedure.

The original design of the torque magnetometer included a solid platform. All of the early attempts were focussed on fabricating a device with that particular design. The success of the final attempt is due to the addition of holes to the platform. By changing this aspect of the design, a torque magnetometer was successfully fabricated and fully released. For convenience, it is named the Perforated Platform Process. All procedures were performed in a Class 10000 cleanroom located in the John Hopkins Engineering Building on the McMaster University campus.

4.1 General Overview

All of the processes attempted followed a general procedure that can be broken down into three stages: metallization, deep reactive ion etching (DRIE), and release etch. Before fabrication began, however, it was necessary to prepare the initial samples.

Sample Preparation:

Samples were fabricated from 150 mm diameter crystalline SOI <100> oriented wafers doped with boron. The device and substrate layers have resistivities of 0.001 – 0.005 Ω -cm and 1-20 Ω -cm, respectively. Physical connections can only be made to two corners of the device, thus a conducting device layer is necessary to set the bridges and the platform at a fixed potential while doing electrical experiments. The thicknesses of the device, oxide, and substrate layers are 50 μm , 5 μm , and 590 μm , respectively (displayed in Figure 4.01). After cleaving the large wafer into approximately 15 x 15 mm squares, the samples were placed in a beaker of DI water in an ultrasonic bath to remove any silicon particles produced from the cleaving process. The samples were subsequently immersed in buffered hydrofluoric acid (BHF) to remove any native oxide.



Figure 4.01: Side view of SOI wafer (not to scale)

1. Metallization:

Metallization was accomplished by the lift-off procedure, and served to lay down contacts for the electrodes and bridges [38]. Approximately 20 nm of chromium and 200 nm of gold respectively were deposited using an electron beam evaporator. Figure 4.02 displays the schematic top view of a sample after metallization.

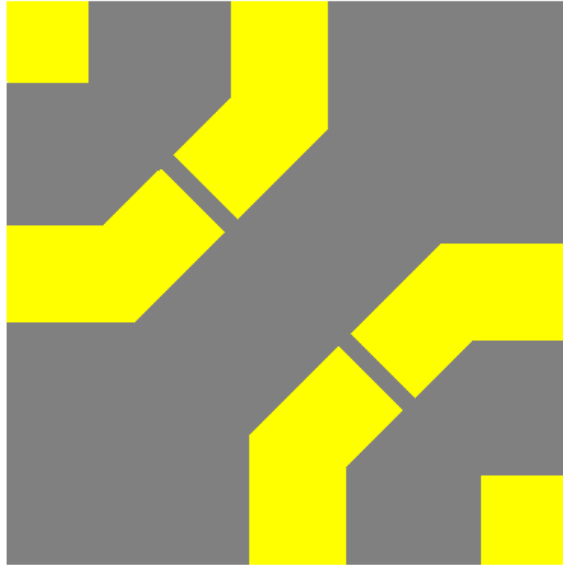


Figure 4.02: Pattern of deposited chrome gold on sample (not to scale), achieved by the lift-off procedure

After metallization, the samples were all cut to the same size (12.5 x 12.5 mm) using a dicing saw. Due to the thickness of the SOI wafer, cleaving to the exact size was difficult, hence the use of the dicing saw. The blade used was 750 mm deep and 30 μm wide. This step removed any excess gold around the border of the device, thus isolating the electrodes and bridge contacts.

2. Deep Reactive Ion Etching (DRIE):

Once metallization and dicing were completed, the next step was to etch out the device pattern by means of DRIE. Reactive ion etching (RIE) was not sufficient to provide the aspect ratios desired, as explained in the next two paragraphs.

Given that the bridges are between 5 and 10 μm away from the electrodes, and given that the device layer is 50 μm deep, straight sidewalls with an aspect ratio of at least 10:1 are desired. After 200 min of RIE at 100 W using the STS 320 PC here at McMaster University, 50 μm of silicon was etched, and the oxide layer was exposed [39]. Figure 4.26 is an SEM image illustrating the resulting sidewalls. The gap in the SU8 mask was 400 x 400 μm . The aspect ratio of the sidewall is approximately 1:1.

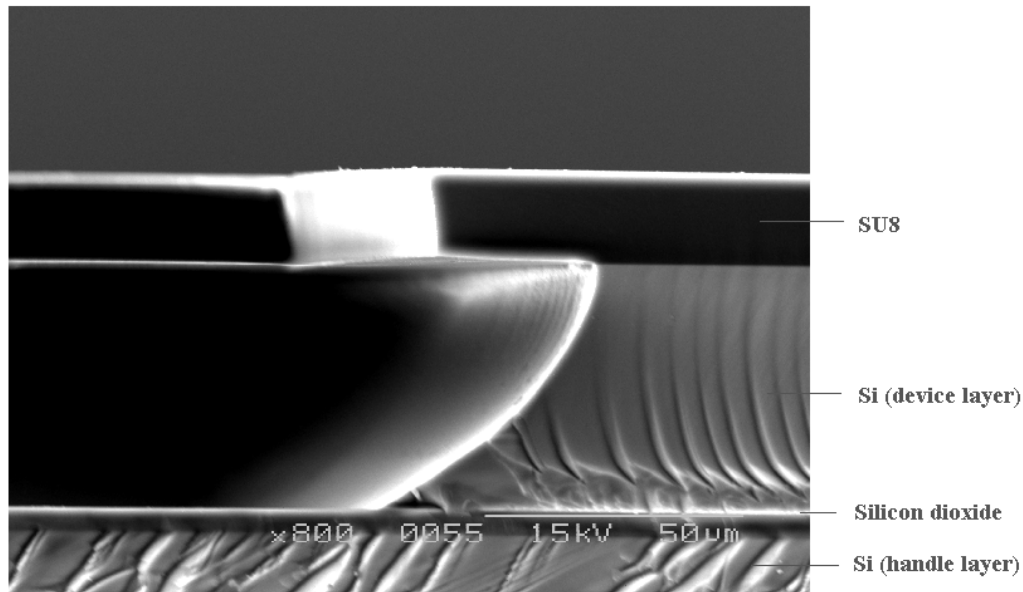


Figure 4.03: SEM image of sidewall profile of sample after conventional RIE

In comparison, after 25 min of DRIE at 1800 W using the Alcatel 601E at the University of Western Ontario, 50 μm of silicon was etched through a gap 10 μm wide. Figure 4.04 shows the result. As can be clearly seen, the aspect ratio is 10:1 or greater.

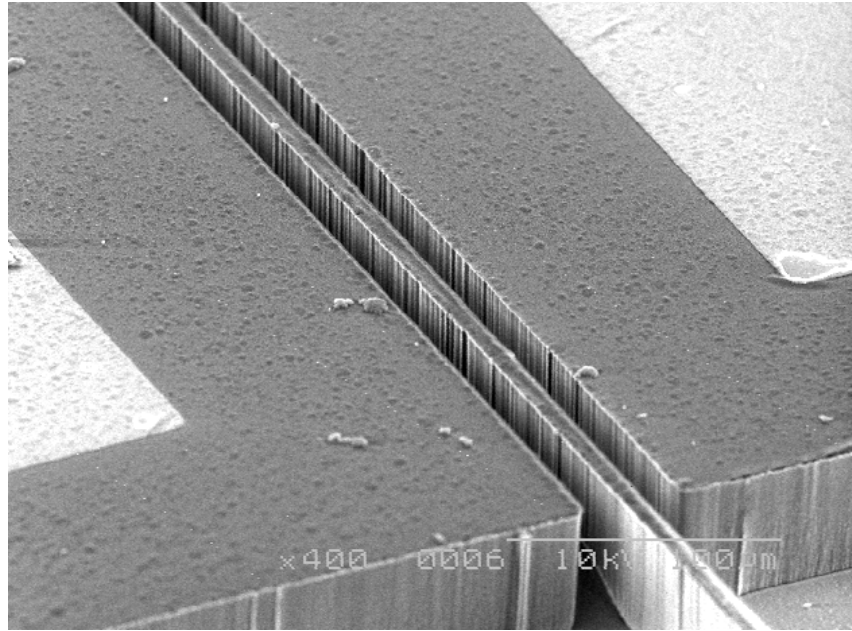


Figure 4.04: SEM image of bridge between electrodes after DRIE, and before the bridge release. The gold contacts can be seen (100 μm magnification).

The huge difference between the two results lie in the process employed. RIE uses one gas to etch the silicon, SF_6 . During the duration of the process, the sample is bombarded with this one gas, causing more undercutting as the etch progresses. DRIE, on the other hand, alternates between two gases, SF_6 and C_4F_8 . Demonstrated in Figure 4.05, the etch starts out with SF_6 for a few seconds, then switches over to C_4F_8 for a few seconds, and then repeats. In those first few seconds, an etch pit is created by the SF_6 gas. C_4F_8 is used to passivate or to shield the etch pit. After passivation, the sample is again bombarded with SF_6 , which etches through the passivation layer on the bottom of the etch pit quicker than the layer on the sidewalls. The result is scalloped sidewalls, with the scallops being no more than 70 nm in length after a 50 μm etch [40, 41]. The usage of the passivation layer and the cyclic nature of DRIE sets the Bosch process far above RIE in terms of straight sidewalls and insignificant undercutting.

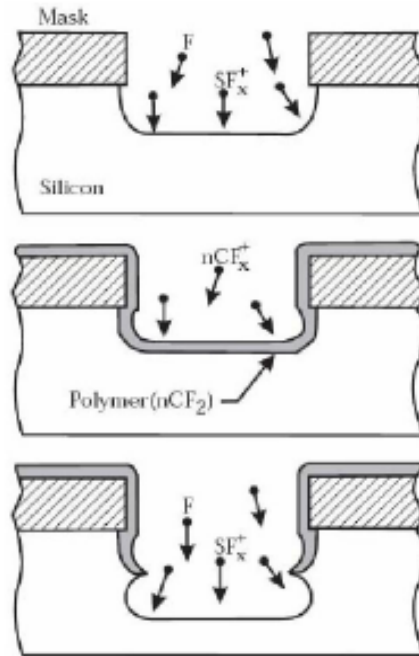


Figure 4.05: Principle of the Bosch process. It alternates between two gases, SF_6 and C_4F_8 , where SF_6 etches and C_4F_8 passivates [42].

Keeping the etch depth and the flow rates of the gases constant, the total etch time and the cycle times of the gases are dependent on the size of the gap openings in the mask. Larger gap openings require longer etch times and shorter C_4F_8 cycle times. Changing the cycle time allotted to C_4F_8 has significant effects. If the time is too high, too much of the passivation layer is deposited, and 9 seconds of SF_6 is not enough to fully etch through that layer. This results in silicon nanowires at the bottom of the etch pit, which is sometimes referred to as ‘grass’. The same effect occurs in other situations. For example, if the protecting photoresist layer on top of an SOI sample is too thin during DRIE the etch begins to eat into the top silicon layer. Figure 4.06 demonstrates this effect with a close-up of the edge of the top silicon layer. This particular sample has been etched with DRIE and the middle oxide has been removed. Parts of the bottom layer also have silicon nanowires. If the cycle time is too low, SF_6 eats through the passivation layer quickly and ends up eating into the corners of the etch pit. This results in an etch pit with a widened bottom (like the base of a vase). Looking carefully at Figure 4.04, it is concluded that the cycle time allotted to C_4F_8 must have been slightly too low. It is for this reason that the completed device has bridges partially etched along the bottoms.

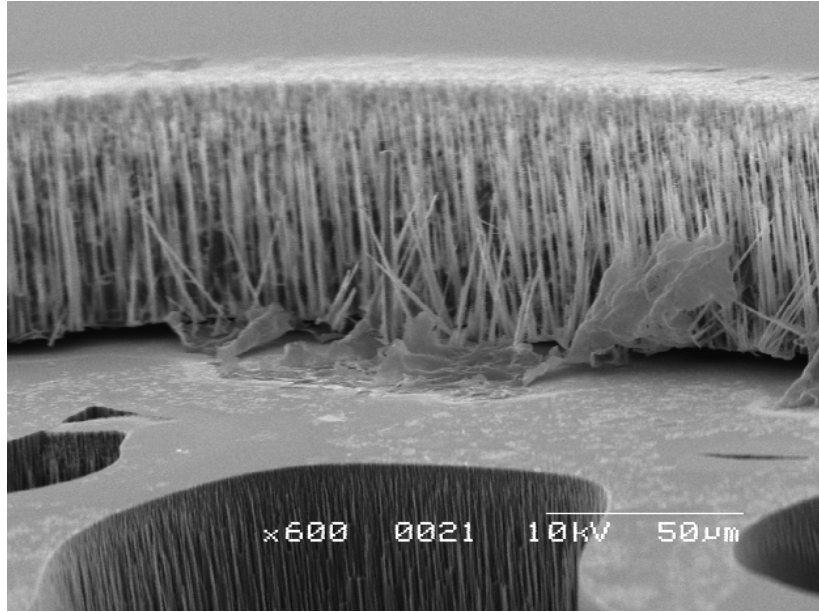


Figure 4.06: Silicon nanowires as a result of inadequate photoresist protection during DRIE. Bits of photoresist in between the top and bottom silicon layers can be seen.

Mounting of the samples in the Alcatel 601E requires the samples to sit upon a 4-inch wafer, due to the constraints of the mounting platform. Crystal bond was used to glue the samples onto the center of the 4-inch wafer to prevent movement; four samples to each wafer. Care must be taken in the application of the crystal bond, as it is also used as a thermal conductor. A sufficient amount is needed to conduct the heat from the sample to the 4-inch wafer, to prevent heat damage to the sample.

In preparation for DRIE, the samples were coated with negative photoresist (SU8 2 or Futurexx NR9 1500P), which was patterned to be used as a mask [43, 44]. During the etch, the photoresist became so hardened that the removal agents which accompany both brands of photoresist were too ineffective. As a result, removal of the photoresist mask after the completion of the etch required the use of a stronger agent. A piranha etch – a 3:1 mix of sulphuric acid and hydrogen peroxide – was sufficient.

3. Release Etch:

At this point, the structure has been formed and is sitting on the 5 μm oxide layer. One final step remains: to remove said oxide layer underneath the structure by immersing the sample in a 48% hydrofluoric acid (HF) solution. This solution is also referred to as concentrated HF. This was the tricky part – trying to remove all the oxide underneath the structure without collapsing the electrodes

and corner supports. Looking at Figure 3.01, one can see the reason for the difficulty is because the solid platform is of the same size as the electrodes and corner supports. This is the main reason why the development of the torque magnetometer fabrication process flow required several different attempts, and why the release of the structure with a perforated platform was much simpler.

After removal of oxide in between two layers of silicon, stiction of the two layers is a common problem in microfabrication. Stiction is not a significant problem on the macroscale, because surface tension does not dominate as it does on the microscale. Oxide is normally removed by HF, and then the sample is immersed in rinse water. When the sample is taken out of the rinse water, the water in between the two layers begins to dry. As the water droplet evaporates, the device is drawn to the substrate by surface tension until it makes contact. Once contact is made, Van der Waals forces maintain the bond, and it is nearly impossible to separate the two layers without damaging the device [4]. Stiction is also a common problem with high aspect ratio structures, such as nanowalls. If the distance between two nanowalls is short enough, the two structures will bend toward each other after rinsing and drying [45]. Since the bridges of the torque magnetometer have an aspect ratio of 10:1, and the gap between the bridge and electrode is 5-15 μm , it is expected that stiction will occur if the sample is left to air dry.

A critical point dryer takes advantage of the critical point of carbon dioxide. A Tousimis® Autosamdri®-815 Series B critical point dryer was employed in this case [46]. The device is immersed in a chamber filled with ultra pure alcohol directly after being rinsed, and then cooled down to 0°C, after which the chamber is filled with liquid carbon dioxide. During the purge mode, the waste alcohol exits the chamber. The critical point of carbon dioxide is at a pressure of 1072 psi and at a temperature of 31°C [47]. Beyond this is the supercritical phase, in which there is no boundary between liquid and gas. In this state, there is no difference between liquid and gas. Therefore there is zero surface tension. This allows the conversion of liquid into a gaseous state without any stiction [47]. After the purge mode the chamber pressure is raised to 1350 psi, and the temperature is raised to 31°C. It is kept at this point for approximately 4 minutes. The final stages of the critical drying process involve the bleeding of the gas and the venting of the chamber, leaving behind the dried and undistorted sample [46].

The critical point drying step has proven to be effective in preventing stiction in the torque magnetometer, and is a very convenient way of drying the device without causing damage.

To quickly sum up, the metallization step lays down the metal contacts for electrical measurements. DRIE etches away unwanted areas of the top device layer, forming the device. Concentrated HF etches away the middle layer (oxide), thereby releasing the device.

4.2 Attempted Procedures

A number of procedures were tested (some simultaneously) before arriving at the successful perforated platform process. Each is listed below in the order in which they were tested. To avoid repetition, the metallization step is not mentioned in the following sections, as no revisions to that stage were made.

4.2.1 Two Stage Release Process

To deal with the release problem, the DRIE process was divided into two stages, thus including an extra release step. Figure 4.07a reveals the pattern used for the first etch step. Four holes are opened up in the center of the silicon. Thus when placed in concentrated HF, the oxide is etched only in the vicinity of those four holes – releasing the center of the device. The second etch opens up the rest of the silicon (Figure 4.07b), and the sample is immersed in a second bath of concentrated HF for a much shorter time to release the bridges.

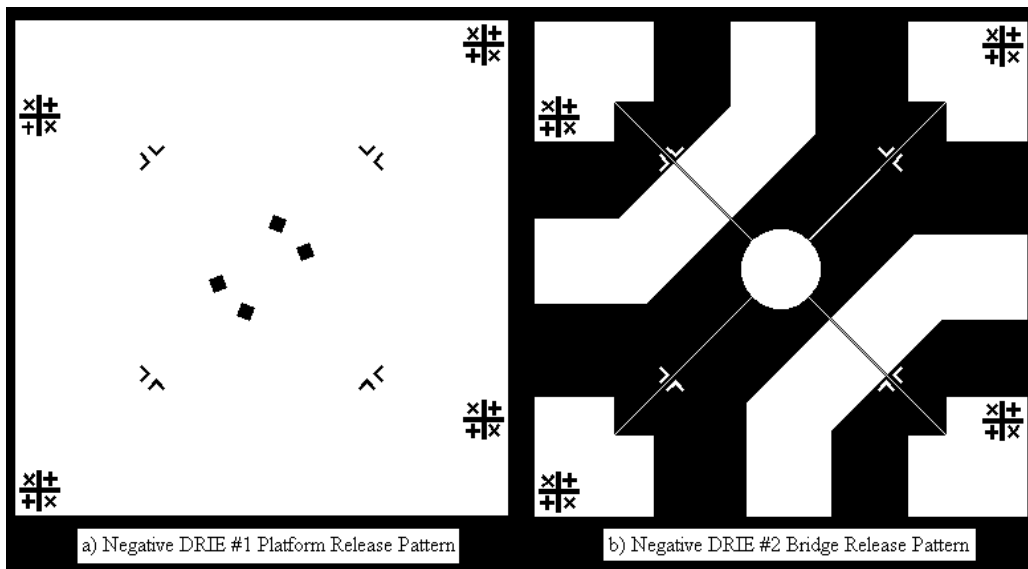


Figure 4.07: Photolithography patterns a) for DRIE #1, where four holes are opened up in the device layer b) for DRIE #2, where the entire device layer is etched

First DRIE Step:

The first DRIE step was as carried out as explained in Section 4.1 using 2 μm of SU8 2 as a mask. Only 12 minutes and 30 seconds of DRIE was needed to

etch 50 μm of silicon through holes of 400 μm by 400 μm . Cycle times allotted to SF_6 and C_4F_8 were 9 seconds and 2.5 seconds, respectively.

First Release Etch Step:

To release the center of the device, the entire sample needed to be immersed in concentrated HF for approximately 12 hours. Because of the long etch time, protection of the border of the sample is required to prevent undercutting of the corner supports and electrodes at the sides. In order to cover the exposed oxide on the border, the sample was ‘masked’ before being placed in the concentrated HF bath. This was accomplished by ‘gluing’ the sample on a larger scrap piece of silicon with Shipley S1808 photoresist, and painting the same photoresist along the sides of the sample. For convenience, this procedure is referred to as the S1808 side masking technique. After alternating between painting on layers and baking at 110°C, the sample was immersed in concentrated HF. Afterwards the sample was placed in a critical point dryer to avoid the pull-in of the released platform (center of device) to the substrate [48]. Figure 4.08 displays the approximate etched area of oxide.

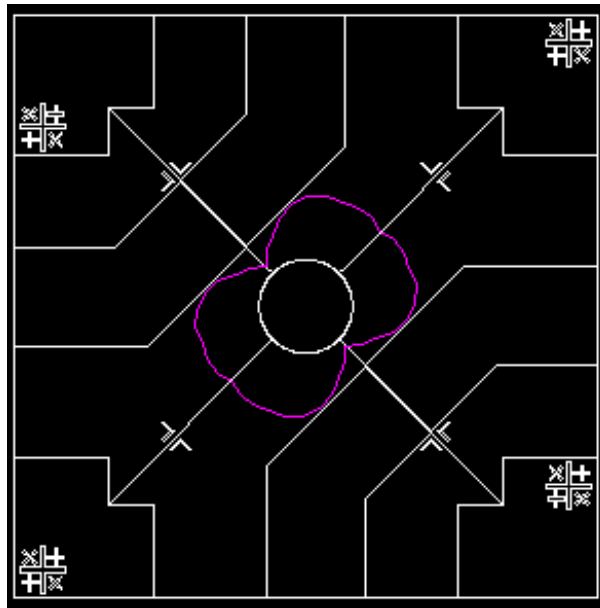


Figure 4.08: AutoCAD image of the device. The area inside the purple lines represent the absence of oxide.

Concentrated HF removes oxide at a rate of 2.3 $\mu\text{m}/\text{min}$ [48]. Since the platform is of a 1 mm radius, all of the oxide should ideally have been removed after 7 hours and 15 minutes. However, because of the narrowness and length of the path the HF has to travel, the etch rate is not constant. The gap between the

top and bottom silicon layer is $5\ \mu\text{m}$ (Figure 4.09). As the etch progresses, the HF has to travel farther underneath the platform, while also filtering out the dissolved oxide. Thus the etch slows down the farther along it progresses. Not knowing how long the etch would actually take, the rate of oxide removal was determined experimentally by using test samples, and subjecting those samples to a KOH etch after HF immersion to see the profile of the remaining oxide [5]. Because the substrate layer is ten times thicker than the device layer, the KOH eats away the device layer first, revealing whatever oxide remains on the substrate layer. From this the actual HF etch rate was determined. During testing, the conditions of the HF etch such as the rotations per minute (RPM) of the spinner and the amount of concentrated HF used were kept consistent.

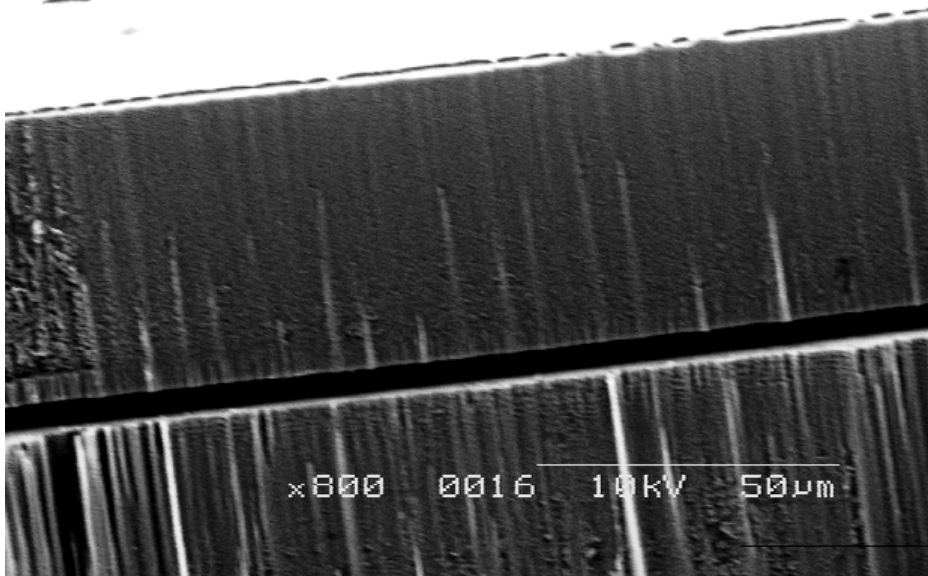


Figure 4.09: View of $5\ \mu\text{m}$ narrow gap between top and bottom silicon layer

Second DRIE Step:

The second DRIE step was carried out as explained in Section 4.1 using $5\ \mu\text{m}$ of NR9 as a mask. At this point it was not realized that NR9 would become equally hardened after DRIE as SU8 was. NR9 was chosen for this step because of its ability to dissolve readily in acetone.

As anticipated, because of much narrower gaps in the etch pattern, the etch was prolonged in order to allow the product gases more time to leave the etch pits. A range of 25-30 min was needed to reach the oxide. Cycle times for SF_6 and C_4F_8 were 9 seconds and 2.4 seconds, respectively.

Once the etch was completed, the sample was placed in acetone in an unsuccessful attempt to remove the NR9. The sample could not be observed under a microscope or SEM as it had to be kept in liquid until after being removed from

the CPD. Thus it was not known the acetone was unsuccessful in removing the NR9 until after the bridges had been released.

Second Release Etch Step:

To release the bridges, immersion in concentrated HF for 3 minutes was sufficient. Figure 4.10 exhibits the first completed device after it was taken out of the CPD, and Figure 4.11 is a SEM image of a portion of the platform and one bridge. During the first fabrication run the dicing step had not yet been incorporated, hence the gold border around the device. The white area around the platform in Figure 4.10 is where the substrate has been etched into by DRIE. As already mentioned earlier, the second DRIE was prolonged so straight sidewalls could be maintained in areas where the gaps were narrow (i.e. between bridges and electrodes). However, in open areas, 25-30 minutes was more than enough for the etch to eat away the entire device layer. Once it hits the oxide, the etch slows down considerably (rate of oxide removal by DRIE: ~ 70 nm/min). Since there was no oxide in the region around the platform, the etch began to eat into the substrate layer. This is the reason for the silicon nanowires present around the platform in Figure 4.11.

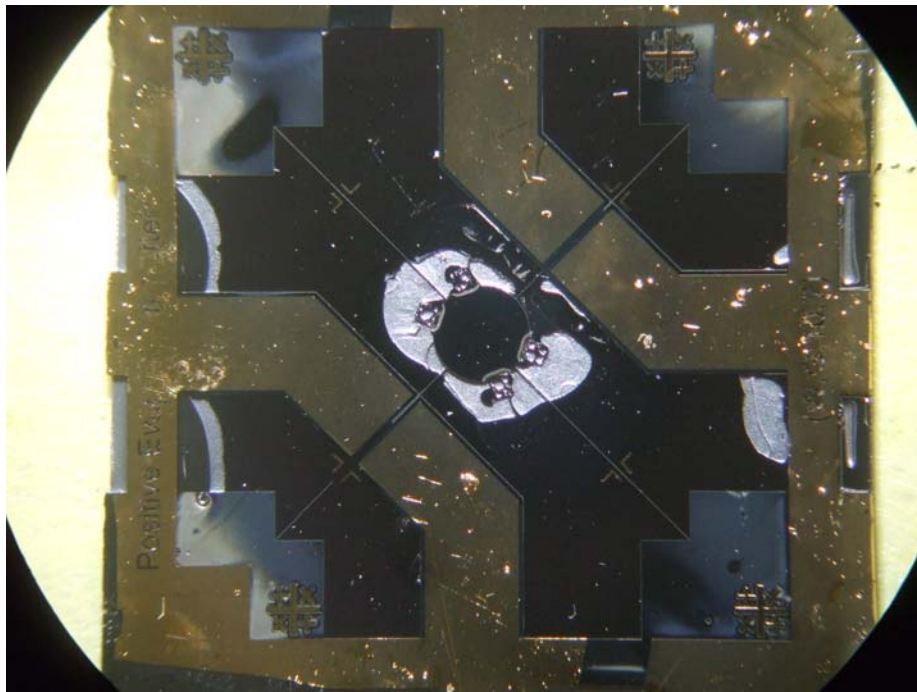


Figure 4.10: First completed device with a gold border. The white area around the platform is where the substrate layer has been etched.

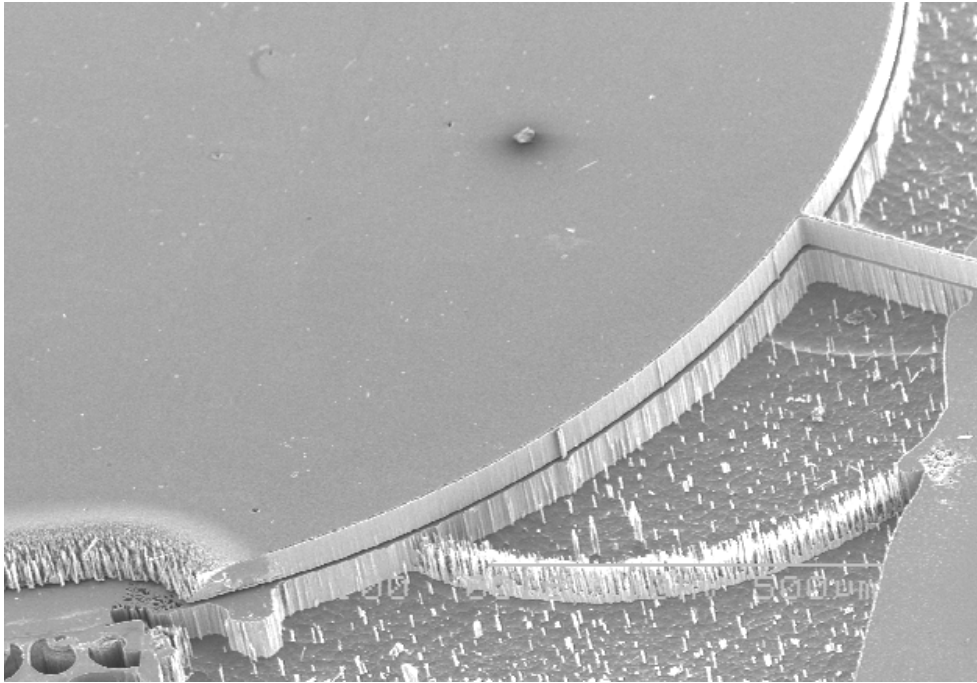


Figure 4.11: SEM image of a bridge connected to the platform (500 μm magnification). The nanowires are a result of the DRIE eating into the substrate layer.

This device has not been proven to be fully released. There was not much that could be done by way of electrical measurements (due to the gold border), thus a second sample was made. It was fabricated using the same procedure with the addition of dicing, and a piranha etch after the second DRIE to remove the NR9. But this device was proven not to be released, according to Figure 4.12. A thin layer of NR9 sticking out from underneath the platform of the second sample can be seen. Somehow the NR9 was able to travel underneath the platform – most likely while the sample was being prepared for the second DRIE. At that point, four holes had been opened up in the device layer, and the oxide had been removed from underneath the platform. So as the photoresist was being poured on the sample, it is very possible that some of it spilled into the four holes and began to travel underneath the platform. The reason for the difficulty of removing photoresist from underneath the platform is not well known.

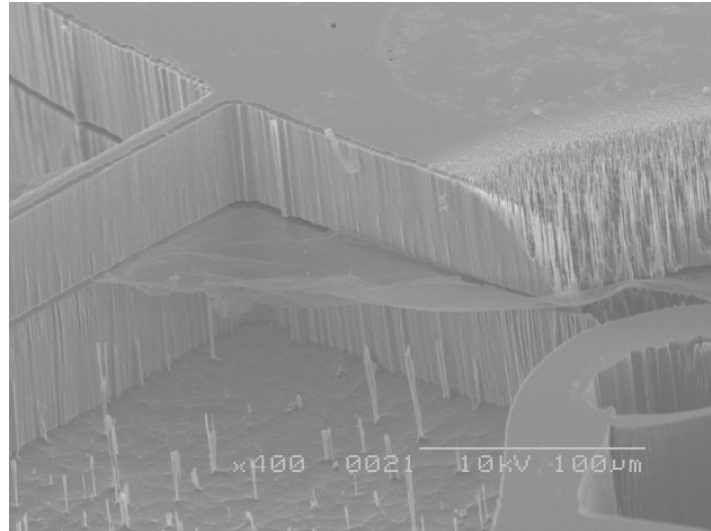


Figure 4.12: SEM image of second sample with NR9 remaining. A thin sheet of NR9 can be seen sticking out from underneath the platform, proving that the device is not fully released.

Not being able to solve the problem, this process was set aside and other methods were devised and tested.

4.2.2 Oxide Removal with Positive Photoresist as Mask

The idea for this attempt came from the S1808 side masking technique. From this technique, it can be concluded that positive photoresist (if applied thickly) is sufficient to protect the oxide along the sides of the sample from being eaten away in a 12 hour long concentrated HF etch. Therefore, it might be a suitable top mask in concentrated HF.

DRIE Step:

Instead of dividing the DRIE into two stages, the entire device pattern was etched in one step. This step was carried out as in Section 4.1 with Figure 4.07b as the mask pattern, and 5 μm of SU8 2 as the mask.

First Release Etch Step:

This is where using positive photoresist as a mask in concentrated HF comes in. Before going into detail, it is necessary to provide a little information on positive/negative tone masks. Both patterns presented in Figure 4.07 are negative tone masks. Negative photoresist is used and black areas on the masks

are washed away in the developer. The use of negative photoresists was necessary because they are more robust than positive photoresists and provide better protection in a DRIE. The reverse of the patterns in Figure 4.07 (turning black areas into white and vice versa) would give positive tone masks.

Using the reverse of the pattern in Figure 4.07a and Shipley SC1827 positive photoresist, the sample was patterned. SC1827 was used because it is thicker than S1808. The S1808 side mask technique was also performed on the sample. Then, it was immersed in concentrated HF for 12 hours to release the platform. This step is similar to the first release etch step in Section 4.1, except SC1827 is used as a mask instead of the silicon device layer.

Observation of the sample after the concentrated HF etch revealed that all of the oxide had been removed in all open areas of the sample. The photoresist layer was still present, but had been partially lifted off in areas where the oxide had been. Apparently, if given an opening, concentrated HF is able to go under positive photoresist and eat away any oxide present.

Primer is often used to improve adherence of photoresist to a sample. Hoping to prevent the lift off of the SC1827 in concentrated HF, an initial layer of primer was laid down in the second attempt. No difference in the results was seen.

Second Release Etch Step:

If the procedure had been successful up to this point, the next step would be to remove the SC1827 by using acetone. Lastly, the sample would be submerged in concentrated HF for a 3 minute etch to release the bridges, followed by a CPD run.

The results of this experiment led to the conclusion that positive photoresist is not a suitable protective mask for relatively long concentrated HF etches. There are other alternatives for concentrated HF masking (such as black wax), but combining those alternatives with the fragile nature of the bridges is extremely difficult.

4.2.3 Two Stage Release with Alternate Masking Materials

The first DRIE step and the first release etch step remained the same as in Section 4.2.1.

Second DRIE Step:

In Section 4.2.1, NR9 failed as a mask because it was difficult to remove from underneath the platform. SU8 was chosen for the second attempt at this process because it is more viscous than NR9, and would not be able to travel underneath the platform as easily. Thus the problem of removing photoresist from underneath the platform would not arise.

However, after spinning on of SU8, the center of the device dipped. This is a sign of stiction. Once that occurs, proper patterning of the photoresist is immensely difficult because the surface is not flat. The reason for the stiction is not immediately known. It is possible that stiction did not occur when using NR9 because it was able to travel underneath the platform and prevent it from dipping to the substrate.

Not being able to resolve this issue, the two stage DRIE process was set aside.

4.2.4 Backside Etch Process with Flip Procedure

The backside etch process consists of etching through the backside and the front side, in that order. Etching in this way would require the need for only one short concentrated HF release etch. To reduce the number of trips to a remotely located DRIE system, a procedure was developed in which both ion etches could be done in one trip, in the reverse order.

DRIE Step:

Beginning with a cleaved, metallized, and diced sample, the backside was patterned with a ~2 mm hole, using the mask shown below in Figure 4.13. The pattern on the glass mask was crudely formed using electrical tape and a microscope slide. Approximately 40 μm of SU8 25 was deposited and exposed [43]. The sample was then flipped, and the front side was patterned with SU8 according to the pattern found in Figure 4.07b.

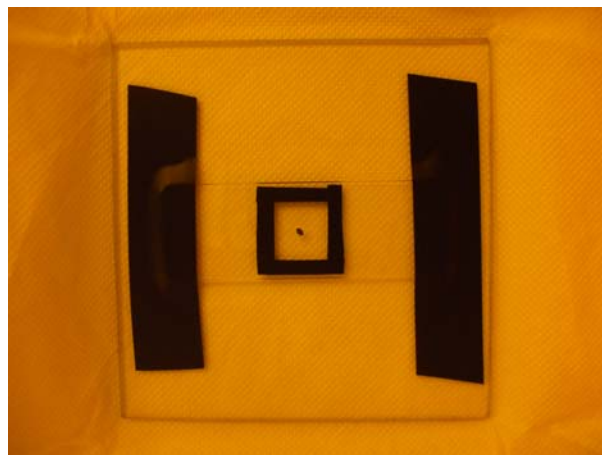


Figure 4.13: Homemade mask for patterning backside hole either by DRIE or by KOH etching

Etching of the front side was performed first, and then the sample was flipped and the backside was etched. This order was established to prevent distortion of the more fragile front side photoresist pattern. Due to the much longer etch depth of the backside (590 μm), DRIE took approximately 2 hours to reach the oxide layer.

Removing of the hole in the backside could alternatively be done by KOH etching, as straight sidewalls are not needed in this case. KOH etches silicon anisotropically, and at a much higher rate than silicon dioxide [5, 6]. Approximately 1.2 μm of wet oxide growth on both front and back sides of a diced wafer should be a sufficient mask in a 20% by weight KOH solution at 70°C for 12 hours [39, 49]. Thus a 2.5 μm layer of wet oxide was grown on both sides of the sample, using a tube furnace at 1,000°C for 24 hours [50]. Patterning of the oxide mask was done by deposition and exposure of SU8 and dipping the sample into concentrated HF for 3 minutes. The front and sides were protected by using the S1808 side masking technique. Following is an image of the hole after the KOH etch.

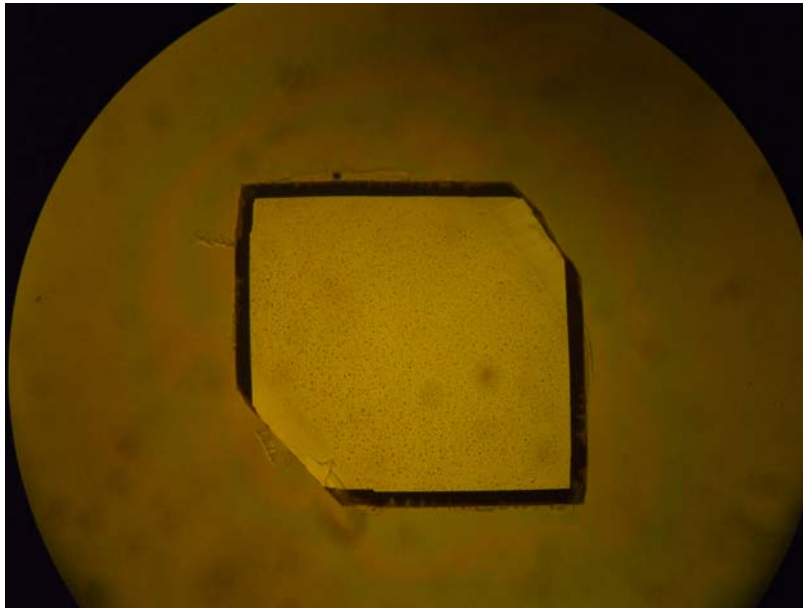


Figure 4.14: Image of the hole in the substrate after the KOH etch. The oxide layer can be seen through the diamond shaped hole.

However, due to time constraints, it was quicker to DRIE the hole in the backside. Since that method was successful, there was no reason at the time to continue with this alternative.

Unfortunately, the time saving flip procedure ended up bringing more harm than good to the fabrication process. As explained in Section 4.1, the 4-inch wafer holding the samples bear the brunt of the heat. While the sample is being

bombarded with gases, the heat is conducted from the sample through the crystal bond to the 4-inch wafer. During the etching of the backside, the already etched front side with a layer of SU8 was in contact with the crystal bond for approximately 2 hours, sustaining significant heat damage. Figures 4.15 and 4.16 show the extent of the burns and cracking. As a result of the heat damage, the majority of the bridges on all the samples were either cracked or broken. By the end of processing the weakened bridges were missing sections.



Figure 4.15: View of a sample fabricated by the backside etch process with flip procedure, showing a bridge running between the electrodes. Burn marks can be seen.



Figure 4.16: Another view of the same sample. Burn marks and cracks on a bridge can be seen.

Removal of the flip procedure from the backside etch process was the obvious next step, as explained in the next subsection.

4.2.5 Backside Etch Process without Flip Procedure

DRIE is once again divided into two stages, but there is no release etch in between.

First DRIE Step:

Having eliminated the flip procedure, it made more sense in terms of stability to have the backside etched first. This was done again by DRIE, using 40 μm of SU8 25 patterned with the mask displayed in Figure 4.13. SU8 removal was performed using a piranha etch.

Second DRIE Step:

The front side was patterned using 5 μm of SU8 2 according to the pattern in Figure 4.03b and etched by DRIE. Before this second etch was performed, the hole in the backside was filled with crystal bond to prevent damaging effects during the DRIE. Once the device was observed under an optical microscope after

the etch was completed, it was discovered that most of the bridges were broken. Images of the two bridges on either side of the platform are shown in Figures 4.17 and 4.18.

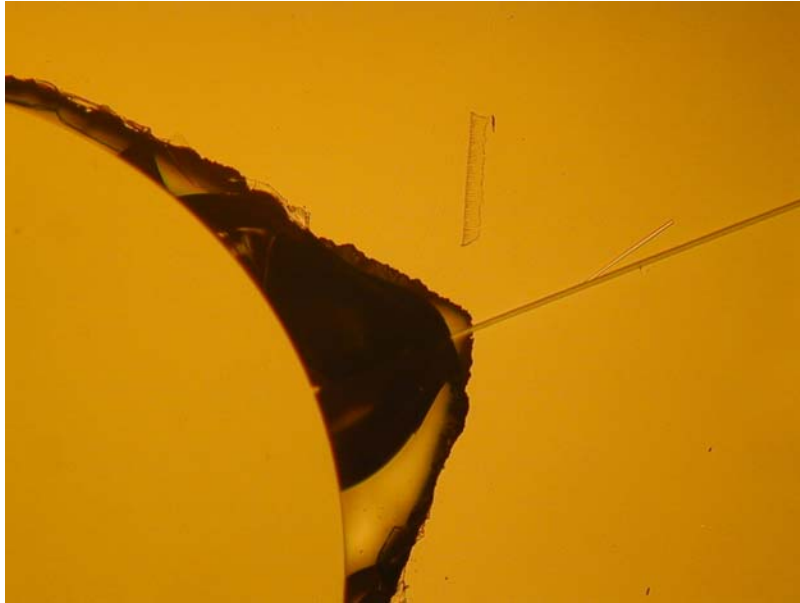


Figure 4.17: View of a sample fabricated by the backside etch process without flip procedure. A hole in the substrate and a broken bridge can be seen.

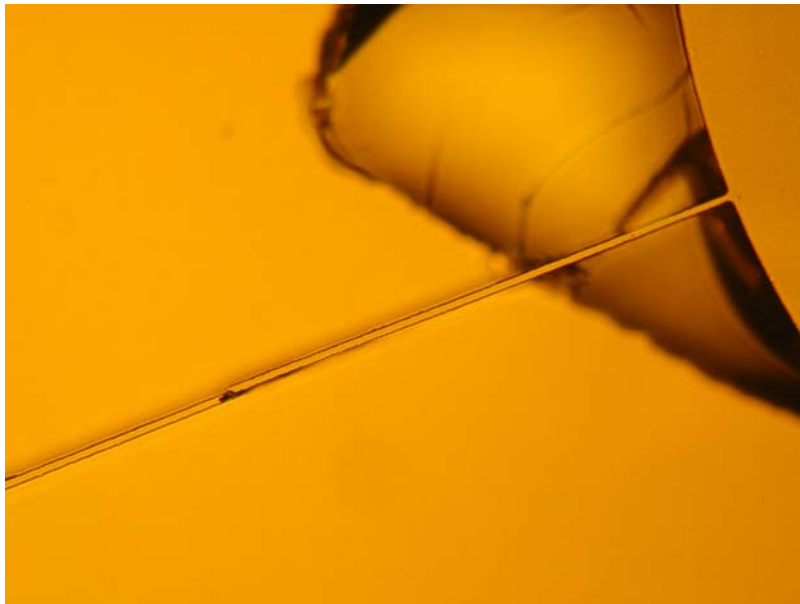


Figure 4.18: Another view of the same sample. The hole in the substrate and another damaged bridge can be seen.

The hole crudely patterned in the backside can be seen in the above images – it is mostly diamond shaped. There are two ideas as to why the bridges broke: a) as the backside pit was filled with crystal bond, air gases were trapped at the bottom of the pit. During DRIE these gases expanded due to heat, pushing on the platform and causing the bridges to break or b) it could be due to the expansion of the crystal bond itself, as it was heated up during DRIE.

If the hole patterned in the backside was a perfect circle of a diameter smaller than the platform itself, the same result would probably occur. The expansion of the gases or of the crystal bond is enough to move the entire platform upwards. Figure 4.18 supports that theory, since the bridge is not broken over the gap, but farther down its length. Figure 4.19 is another supporting image from the same device, of another portion of the platform where the hole from the backside cannot be seen. This bridge is also broken.



Figure 4.19: A third view of the same sample, showing a missing bridge

This procedure was devised to increase accessibility to the area underneath the platform, for easier and quicker oxide removal. Since it did not pan out, another way of access was formulated – through the device side instead of the backside.

4.3 Perforated Platform Procedure

As the name suggests, this particular procedure involved etching of holes in the platform along with the rest of the device. Starting in the center, the holes

are arrayed hexagonally, thus ensuring equal distances between each pair of holes. Four different hole configurations are possible: the diameters of the holes are 50 and 100 μm , and the spacing in between them are 200 and 300 μm .

Etching holes into the device for easier release is a common MEMS technique which was avoided up until now. The magnetic crystal used as a sample would need to be glued to the platform – which could pose a problem if the glue seeped through the holes. However, it is possible to find glue that is more viscous. Or a different way of adhering the sample to the platform could be devised.

DRIE Step:

Using the pattern displayed in Figure 4.20 with a hole diameter and spacing of 100 μm and 300 μm respectively, the first device was etched with 5 μm of SU8 2 as a mask. The new pattern contains holes in the platform, and does not have L-shaped alignment marks. Figure 4.21 shows why these alignment marks were removed – they are released in the final step and are free to move around in HF, thus damaging the bridges in the process. This image was taken of a sample fabricated using the perforated platform procedure (hole diameter and spacing of 100 μm and 200 μm respectively), but was previously metallized using an old pattern with L-shaped alignment marks. Being protected by gold, the L-shaped alignment marks were not etched during DRIE, but were released in concentrated HF.

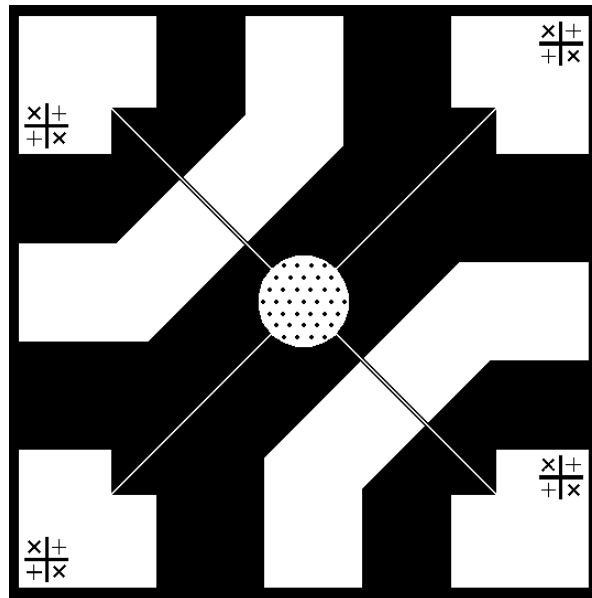


Figure 4.20: Revised photolithography pattern with holes in the platform and no L-shaped alignment marks

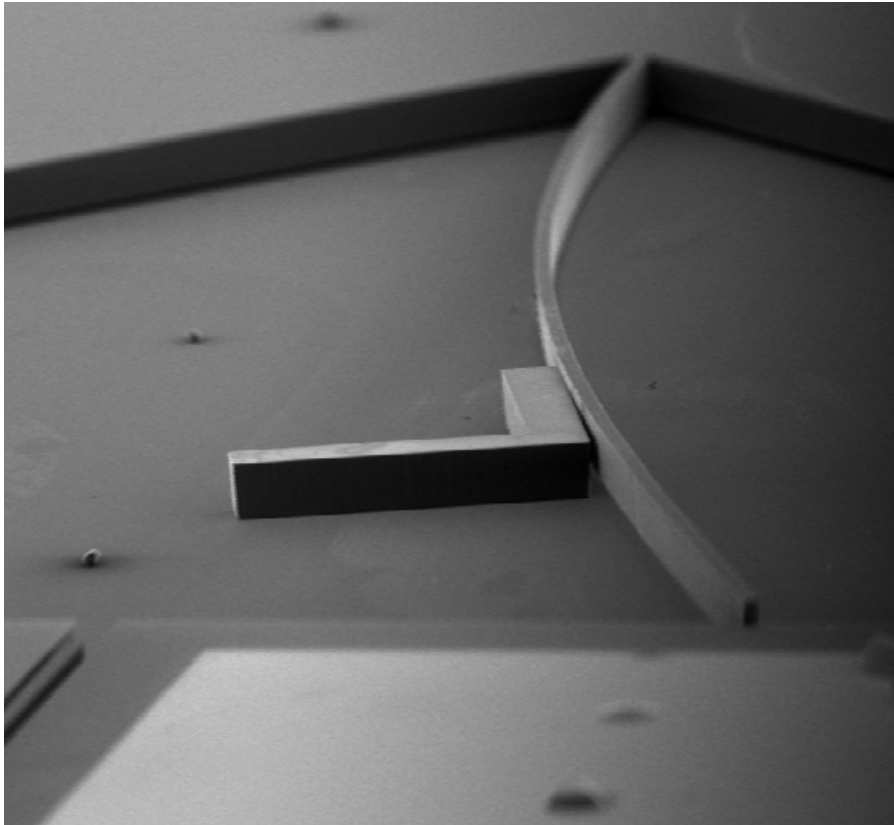


Figure 4.21: View of released L-shaped alignment mark and damaged bridge in a sample fabricated using the original photolithography masks

Release Etch Step:

According to the concentrated HF etch rate (and depending on the spacing between hole pairs), the release etch should take 45 – 60 minutes [48]. Due to effects explained in Section 4.2.1, the actual etch takes at least twice as long. Determination of the actual rate was determined through testing (without KOH this time), and is explained in the sub section below.

After a piranha etch to remove the SU8 and an HF release bath for 3.5 hours, the sample was subsequently placed in the CPD and dried. Following are a number of images of the released torque magnetometer, with an optical image being shown first. The rest of the images were taken in a SEM. For unknown reasons, the metallized gold did not turn out well – it is very spotty. This could be a cleanliness issue. Figures 4.23 to 4.27 display different angles of the device, showing the platform, bridges, and electrodes. Figure 4.28 is a close up of one of the holes in the platform. In some of these images, bits and pieces of unidentified debris can be seen scattered in different areas of the device. These objects could have come from a variety of sources, and could be any of the following: left-over

photoresist, silicon particles, dirt from a beaker, or dust particles from the air. In Figures 4.23 to 4.25 a partial profile of the gold electrodes can be seen, with bubbles and bits of unidentified dirt sitting on them. This is the reason for the ‘spottiness’ in Figure 4.22. The reason for the bubbles on the gold is unknown, and it contributed to the possible uncleanness of the surface before metallization.

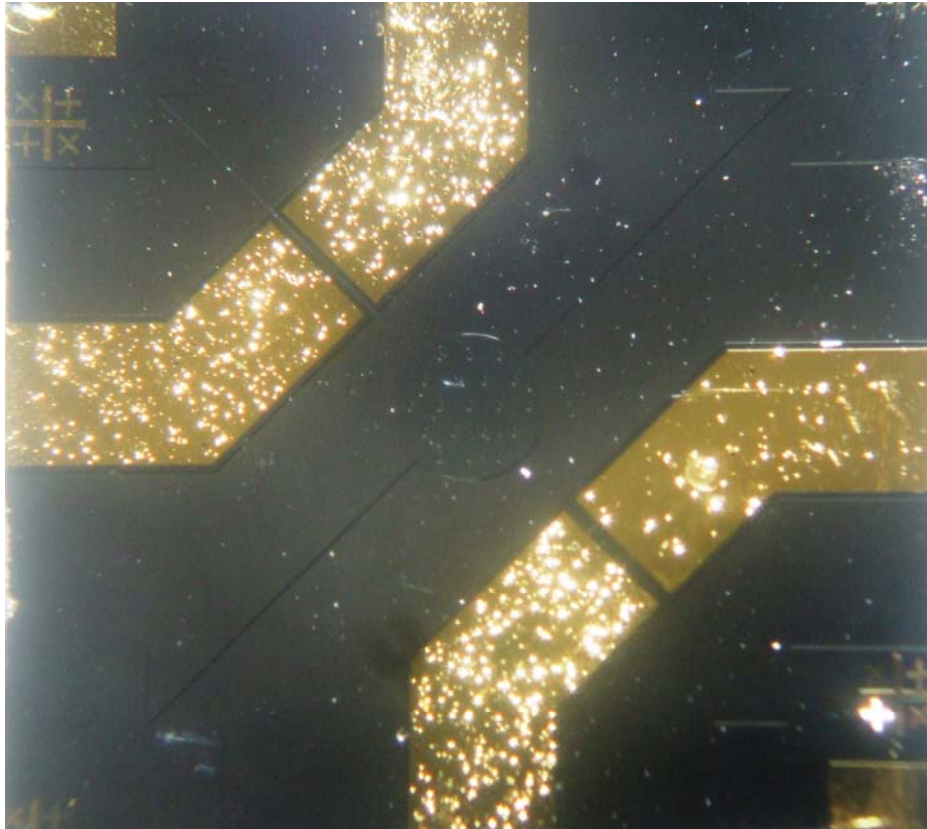


Figure 4.22: Optical image of the completed device, where the yellow is the chrome-gold laid down in the metallization step. Spottiness is attributed to uncleanness.

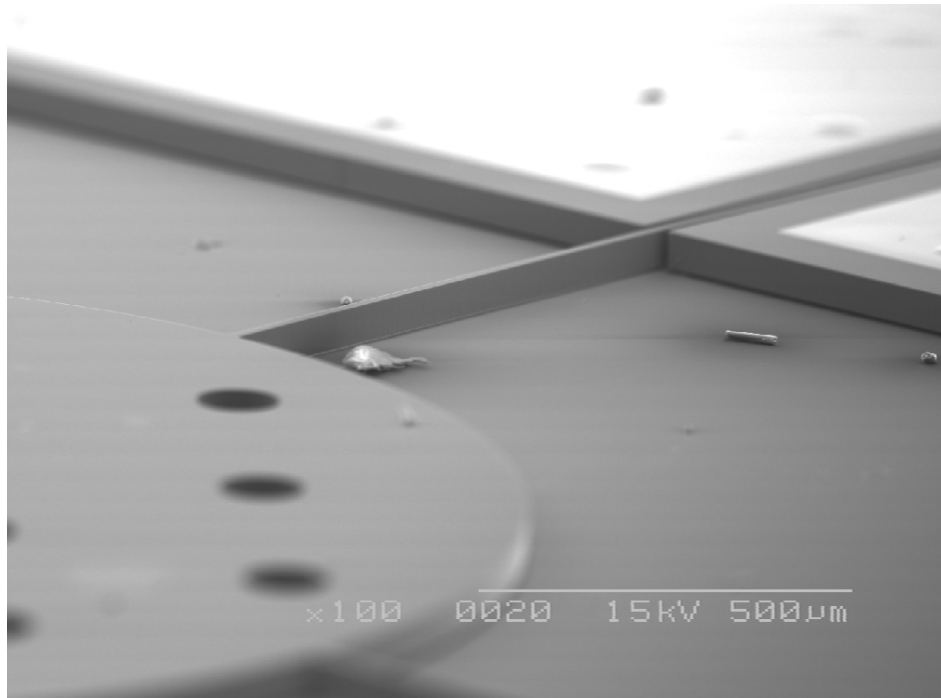


Figure 4.23: View of the platform and a bridge running in between two electrodes

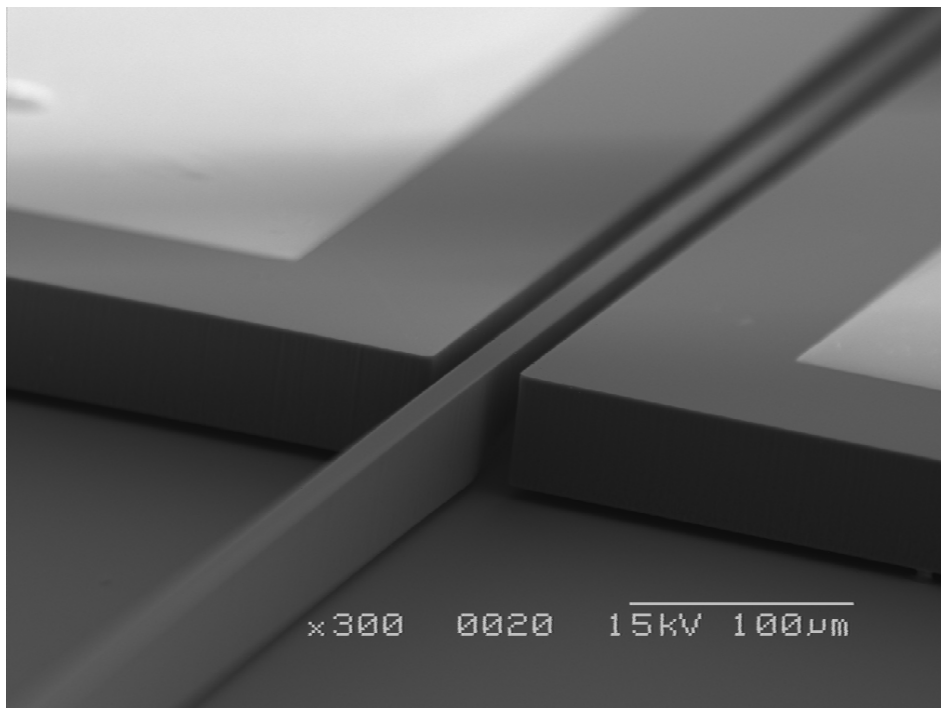


Figure 4.24: A close up of a bridge (10 μm wide) running in between two electrodes

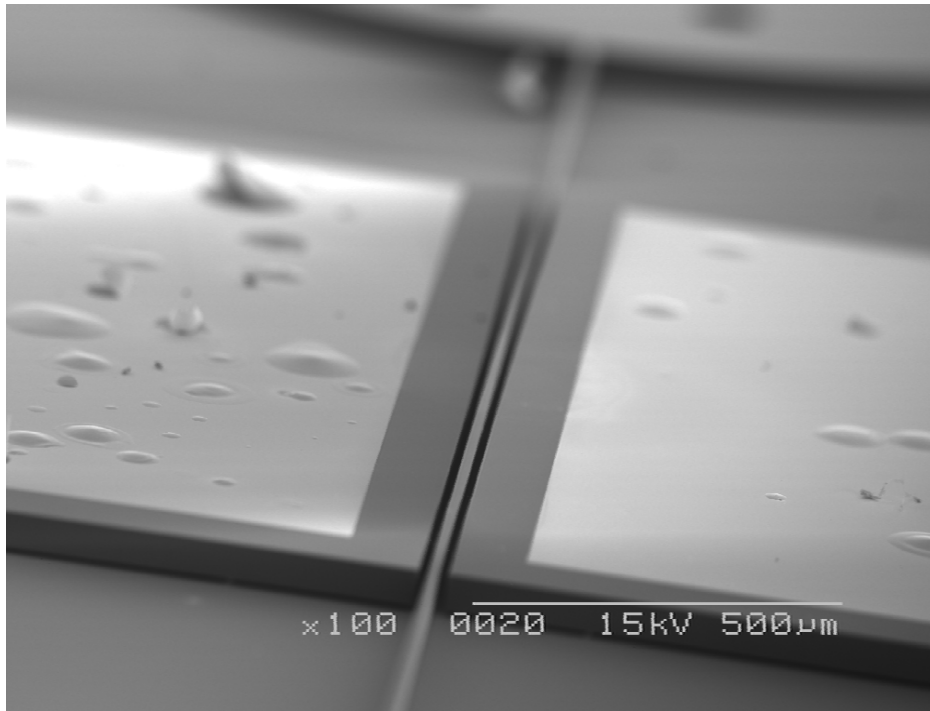


Figure 4.25: View of a bridge running in between the electrodes

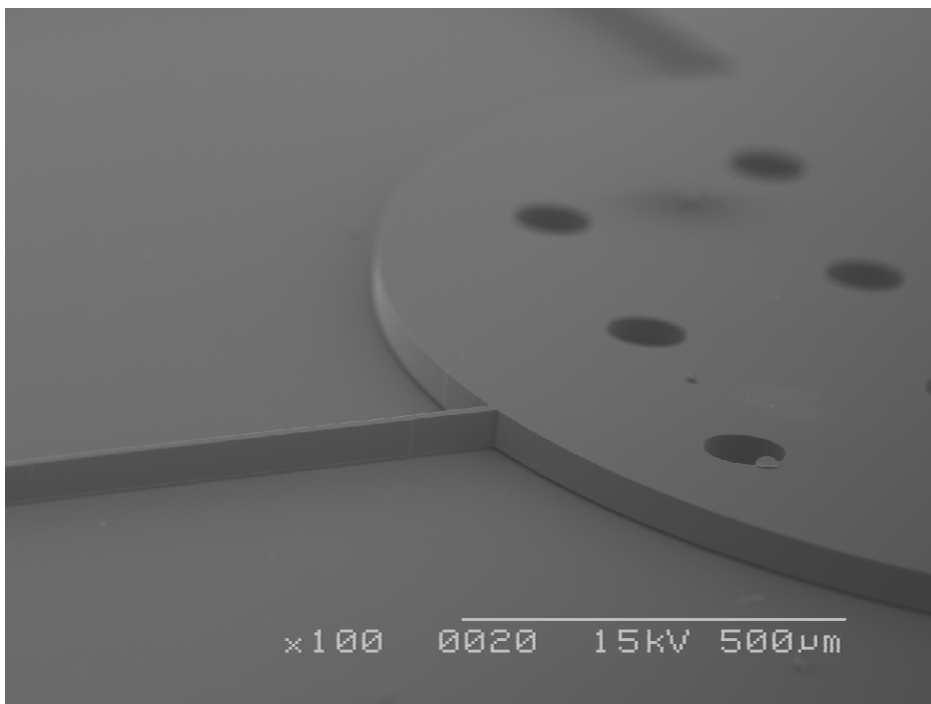


Figure 4.26: View of the released platform and a bridge (50 µm thick), 200 µm spacing between the holes

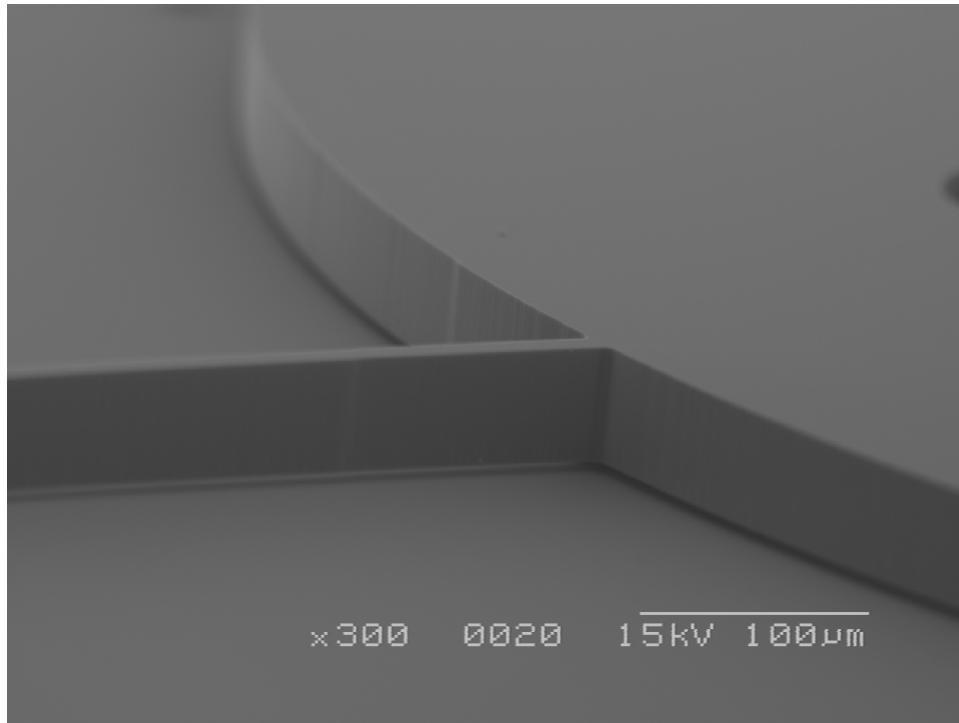


Figure 4.27: Close up of where a bridge meets the platform

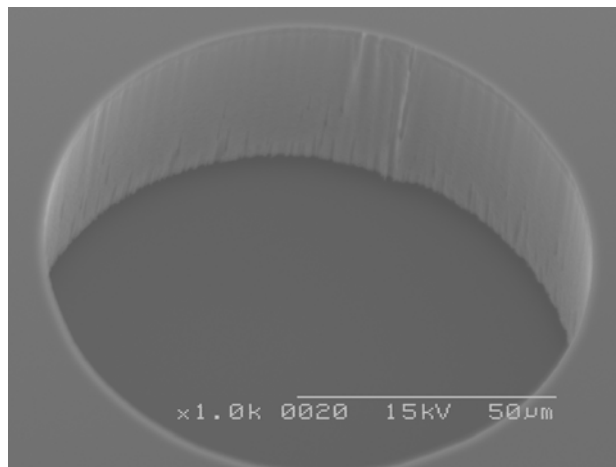


Figure 4.28: Close up of a hole in the platform (100 μm in diameter)

This is the first time a torque magnetometer of this design has successfully been fabricated. As is the case with most new designs, there are a number of imperfections that can be improved upon, cleanliness being the first one. Secondly, more time needs to be spent on perfecting the DRIE conditions. Looking at Figure 4.29, one can see that the bottom of the bridge near the electrode has been etched away.

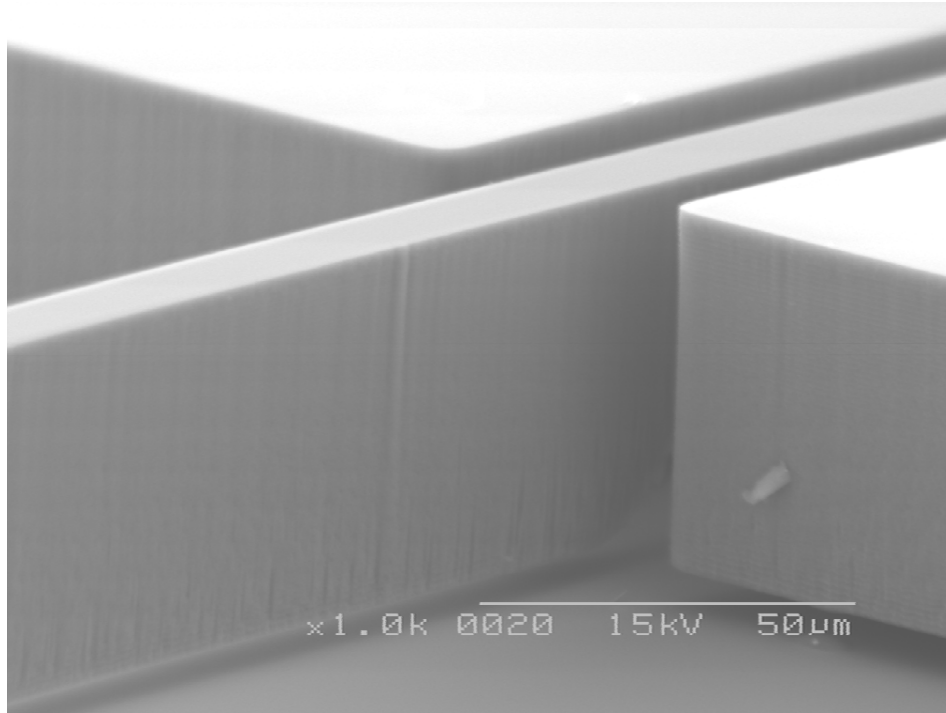


Figure 4.29: View of a bridge, with the bottom of the bridge etched near electrode. This is attributed to the cycle time of the C_4F_8 during DRIE being too low.

Looking closely at the bottom of the bridge as it enters the electrode in this image and image 4.04, approximately a quarter to a third of the bottom of the bridge has been etched in areas where it runs through the electrodes. This can be remedied by experimenting with DRIE conditions.

4.3.1 Proof of Platform Release

Experiments with the concentrated HF rate were performed on a sample that had been discarded, due to broken bridges (Figure 4.21 is an image of a part of this sample). After a concentrated HF bath of 45 minutes, removal of the platform by using tweezers was attempted. Since the platform would not budge, it was suspected that it was either not fully released, or it had stuck to the substrate. Imaging under SEM showed that it was the former (Figure 4.30 shows a gap between the platform and the substrate).

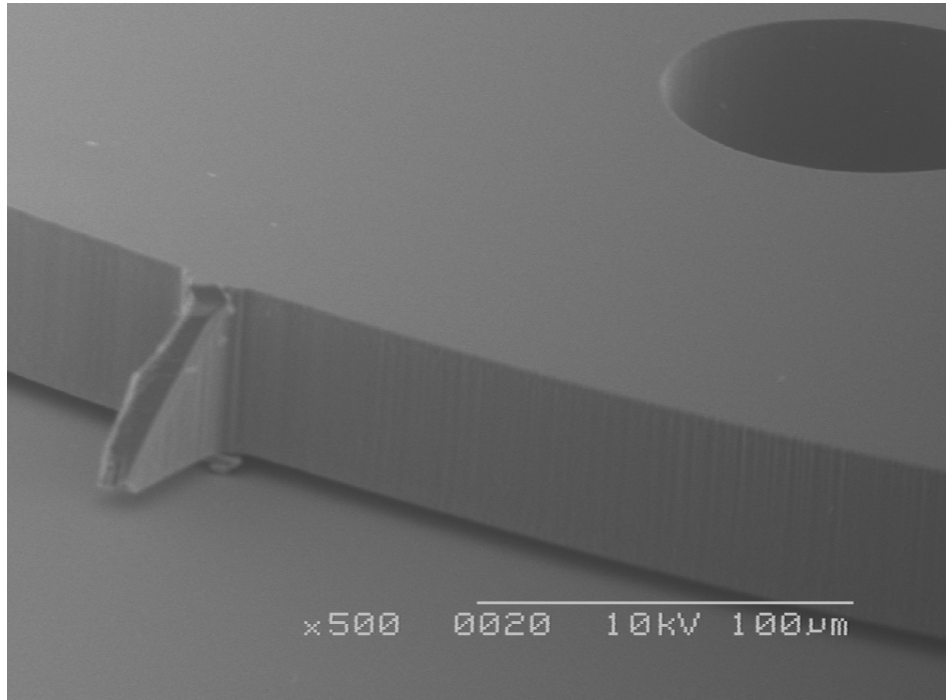


Figure 4.30: View of the 5 μm gap between the platform and the substrate. The place where the bridge broke off can be seen.

The sample was then placed in concentrated HF for another 20 minutes. It was subsequently rinsed and dried with a N_2 gun, and imaged under a SEM. There was no change. Thus the sample was put back into concentrated HF for another hour. While drying with a N_2 gun, the platform came off. The backside of the platform was imaged, shown in Figures 4.31 and 4.32, revealing no remaining oxide. The device was also observed in the SEM, and no oxide could be seen in the area where the platform had been. Thus it was determined that the releasing of a platform with holes of 100 μm in diameter with 200 μm in spacing between pairs requires no more than 2 hours and 5 minutes in concentrated HF.

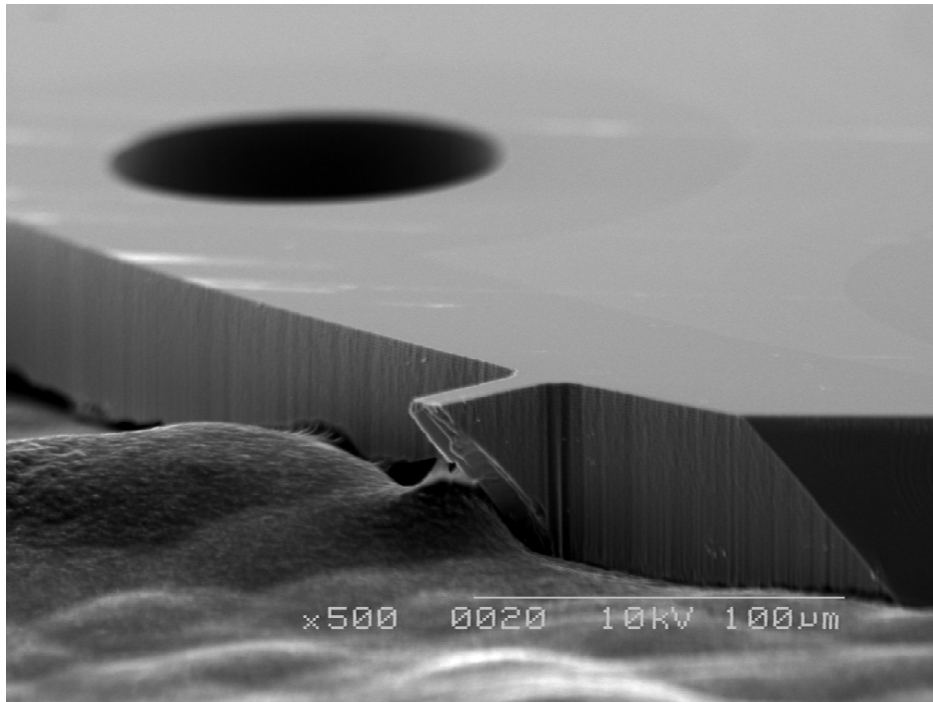


Figure 4.31: Close up of where the bridge has broken off of the platform. The furry and bumpy substance the platform is sitting on is black tape.

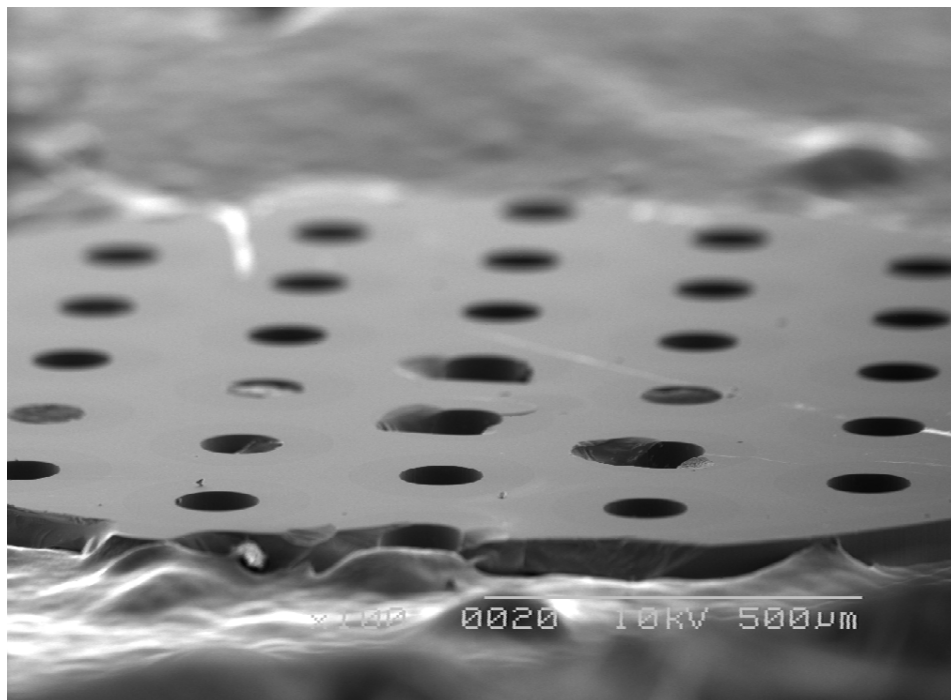


Figure 4.32: View of the backside of the platform, revealing the absence of oxide

Since the first device had a hole configuration different than the one tested, the concentrated HF etch time had to be estimated based on the results of the testing. Instead of holes with spacing in between them of 200 μm , the first device had holes with spacing of 300 μm . As already mentioned, this particular device was left in concentrated HF for 3 hours and 30 minutes. Compared to the 2 hours and 5 minutes needed to release a platform with holes of 100 μm in diameter with 200 μm spacings, this extended etch time is sufficient.

Five more devices with platforms containing holes of 100 μm in diameter with spacings of 200 μm were successfully released, with the final one used for electrical testing. One of them was accidentally destroyed while making connections for electrical testing, so it was used to further prove platform release. Tweezers were used to push on the side of the platform, and because it was still attached to one bridge, it began to swing like a pendulum. Viewing under the microscope, there was no oxide present in the center of the device. Therefore, there is no doubt that the torque magnetometer that was used for electrical testing was fully released.

A torque magnetometer of this particular design was successfully constructed following the procedure laid out in Section 4.3 of this chapter. Over the course of fabrication, finer details (such as the elimination of the L-shaped alignment marks and dicing to remove the gold border) were ironed out. After performing many fabrication runs, the procedure for building the torque magnetometer has been established.

5. Testing

Having successfully released a torque magnetometer, the final stage to this thesis is the characterization and testing of the released device. Once the device was successfully connected to the laboratory equipment and characterized, a number of resonance detection tests were performed. The ultimate goal was to detect the rotational resonance of the torque magnetometer electrostatically. However, it was determined that particular method of detection was not possible. A more optimal method was devised and is presented in the latter part of this chapter.

A higher order mode of the torque magnetometer corresponding to the bridge mode was successfully detected by electrostatic testing. More details will be given later in this chapter.

5.1 Sample Preparation

Using a number of samples, the procedure for preparing the device for characterization was established. Four samples were used as test samples, and the fifth sample was successfully prepared for characterization and was used in all measurements explained in the later sections of this chapter.

5.1.1 Printed Circuit Boards (PCBs)

There are a number of ways to make connections from the device to the laboratory equipment. Using a printed circuit board was deemed the most efficient and convenient method in this case, as it generates the least amount of parasitic capacitance. The board was designed using EagleCAD and made by a student IEEE group on the McMaster campus. Figure 5.01 shows the revised PCB with the device glued on. Standard coaxial cables connect the SMA connectors to the laboratory equipment.

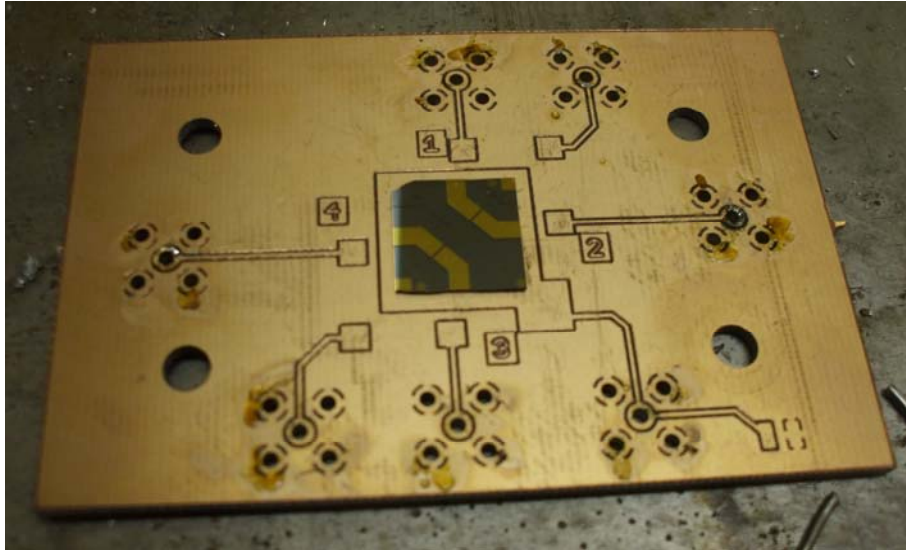


Figure 5.01: A 12.5 X 12.5 mm device on a PCB

5.1.2 Test Samples

In the early stages of the characterization of the device, connections from the device to the PCB were made using silver paint and copper wire. A corner of the first sample is displayed in Figure 5.02, showing the blob of silver paint shorting the device layer to the substrate layer. The corners and edges of most of the devices are roughened and chipped in some places, due to problems with dicing that could not be solved in the fabrication stage. This exposes the substrate layer in some areas. Removal of the silver paint in acetone was largely unsuccessful, as particles of the silver paint tend to collect in all crevices of the device.

The second released device was destroyed accidentally while trying to glue it to the PCB. A dab of silver paint on the center pad of the PCB is used as the glue, but too much of it was put down. As a result, when the device was placed on the silver paint, it came up on the sides. Again, the device layer was shorted to the substrate.

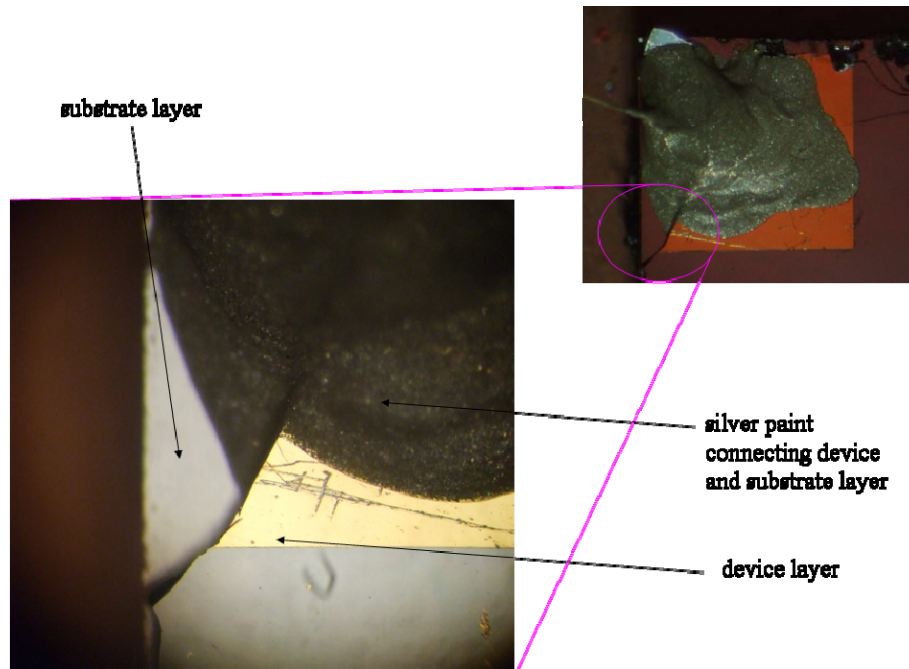


Figure 5.02: A corner of the first sample, showing the blob of silver paint shorting the device layer to the substrate.

At this point, it was realized that making connections to the device would take some practice. One of the devices in the final batch of fabrication had three damaged bridges, making it a perfect test subject. Instead of making connections to the device using silver paint and copper wire, an ultrasonic wire bonding machine was used to ball bond gold wire to the gold pads on the device. Since gold wire does not bond well to the copper on the PCB, the wire was connected to the individual pads on the PCB using silver paint. Also, the gold wires were made long enough so that a 'hill' could be made as shown in Figure 5.03 – preventing a device to substrate short.

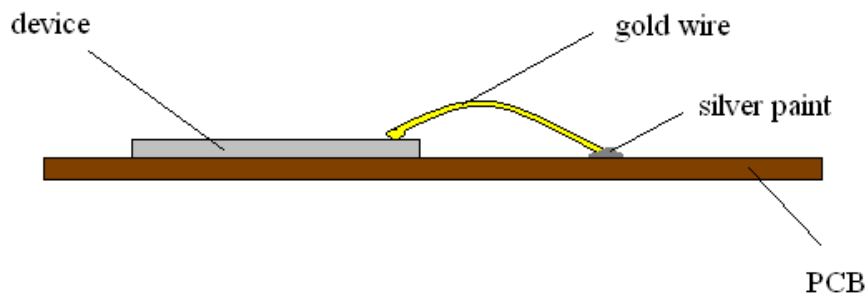


Figure 5.03: A gold wire ball bonded to the device

Once the procedure for making connections was established, a fourth device was released and successfully connected to a PCB. As a result of applying too much voltage ($\sim 20+$ V), a part of one bridge blew up. The actual value of the voltage is not known because a voltage source with a needle gauge was used. Then, the SMA connectors on the PCB became loose and had to be re-soldered. As a result of that, the device was covered in solder flux. From this device two lessons were learned – what approximate value of voltage should not be exceeded, and to reduce the size of the SMA holes on the PCB so that the SMA connectors would not become loose.

5.1.3 Final Device

The fifth released device was successfully connected to a PCB. Using probes and a handheld multimeter (8026B True RMS Multimeter), the resistance of each connection was measured to be zero or close to zero (with one probe on the device and the other probe on the center SMA connector pin). The PCB was successfully connected to the laboratory equipment. Using an Andeen Hagerling 2500A Ultra Precision Capacitance Bridge, the capacitances between connections were measured. The AH 2500A does this by making three terminal measurements, which is a very precise and efficient way of determining capacitances [51]. The results are listed in Table 5.01 along with the theoretical values determined by equation 2.64. As can be seen, the actual values vary by orders of magnitude from the theoretical values. The difference is attributed to unknown background and parasitic capacitances from unwanted particles lodged in the device, unpreventable physical deviations from the design, and/or from electrical connections.

Table 5.01: Theoretical and actual capacitances

	Capacitance (pF)	
	Theoretical	Actual
Bridge – electrode	0.177	6.0-6.4
Electrode – electrode	0.0443	1.8-1.9
Bridge – substrate	232	excess noise
Electrode - substrate	71.8	36-37

Theoretically, there should be a short between the two corner bridge pads. Any spot on the device (corner supports, bridges, and platform) should be physically and electrically connected to all other areas of the device. However, there is no short between the two bridge pads – the capacitance reading and the

resistance reading gives 0.4 pF and 26 G Ω respectively. It was determined electrostatically that the break was somewhere close to the one corner support (B12). Thus all electrostatic measurements were made by using the other bridge connection, named B34. The two electrodes closest to this corner support are assigned numbers 3 and 4. Refer to Figure 5.04 for numbers corresponding to each metal pad.

5.2 Electrostatic Testing

Once the connections were established and the initial measurements were made, a number of electrostatic tests were performed on the device. In all the circuit diagrams in the following subsections, the device is represented as one capacitor, two capacitors, or four capacitors. The bridge (represented by the letter B) is the moveable plate, whereas the electrodes (represented by the letter E) are the fixed plates. In cases where the only two electrodes being used are directly across from each other, only those electrodes are shown in the diagram. In cases where the only two electrodes being used are not in a pair, all of the electrodes are included to conveniently show which electrodes are being used. Figure 5.04 shows how the device is represented in circuit form.

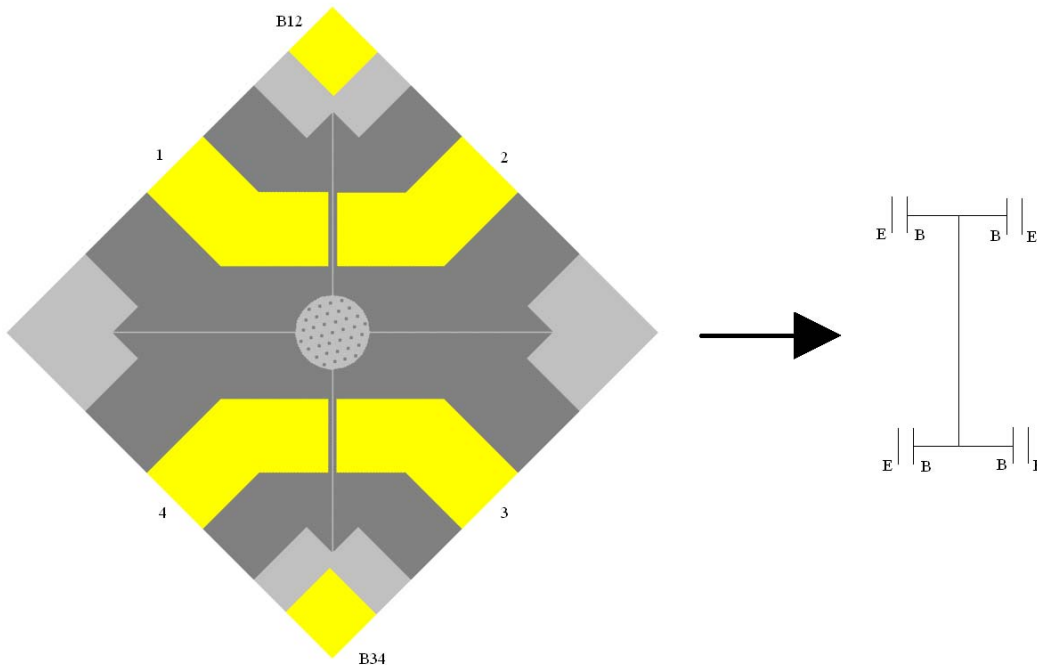


Figure 5.04: Device represented in circuit form, with a bridge and one electrode being one parallel plate capacitor.

5.2.1 Initial Testing

Basic tests were done in air under an Olympus optical microscope. By applying a DC voltage (using the Hewlett Packard 3245A Universal Source) to the device as shown in Figure 5.05, the bridge deflected without the platform visibly rotating. This movement of the bridge was visible to the eye under the microscope. Since the HP 3245A can only supply up to 10 V, another voltage source was added in series (Hewlett Packard 6212B Power Supply). A multimeter (Hewlett Packard 3478A) was put in along with the two voltage sources to measure the total amount of voltage being applied.

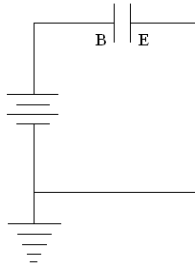


Figure 5.05: Basic testing circuit, used to deflect the bridge

By connecting a function generator (Hewlett Packard 33120A Function/Arbitrary Waveform Generator) to the electrode and applying a low frequency wave (~ 1 -100 Hz), the oscillations of the bridge could also be seen under the microscope. Increasing the frequency also increased the oscillations, until it became a steady blur to the eye, and eventually that blur could no longer be seen by eye (when the frequency reached about 1000 Hz).

The bridge could only be deflected when a DC voltage was applied to the bridge and the substrate was grounded. If the substrate was not grounded and the electrode was, the bridge would not move. When a DC voltage was applied to any electrode, the bridge did not move (regardless of whether the substrate and/or electrode was grounded or not). This would suggest that the potential drop is occurring from bridge to substrate, and not from bridge to electrode. Since the bridge is $5\ \mu\text{m}$ wide and $50\ \mu\text{m}$ thick, it moves from side to side instead of up and down to the substrate.

Figures 5.06 and 5.07 show a series of snapshots of the bridge being deflected. Each snapshot has the corresponding DC voltage underneath it. The snapshots in Figure 5.06 are from the center of the electrodes, and the snapshots in Figure 5.07 are from the end of the electrode, closest to the corner support. On the other end of the electrode (closest to the platform), the movement of the bridge is not detectable to the eye. In both figures, the bridge is at an equal distance from each electrode at 0 V. As the DC voltage is increased, the bridge

starts moving closer to the electrode on the right. As seen in Figure 5.07, the bridge touches the one corner of the electrode at 10 V and starts to bend in the opposite direction as the DC voltage is increased.

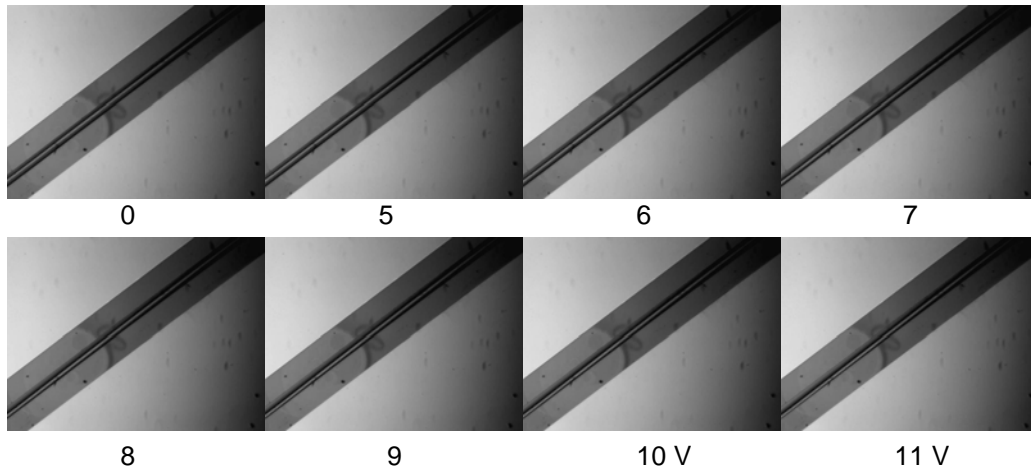


Figure 5.06: Deflection of bridge for certain values of DC voltages at middle portion of electrodes

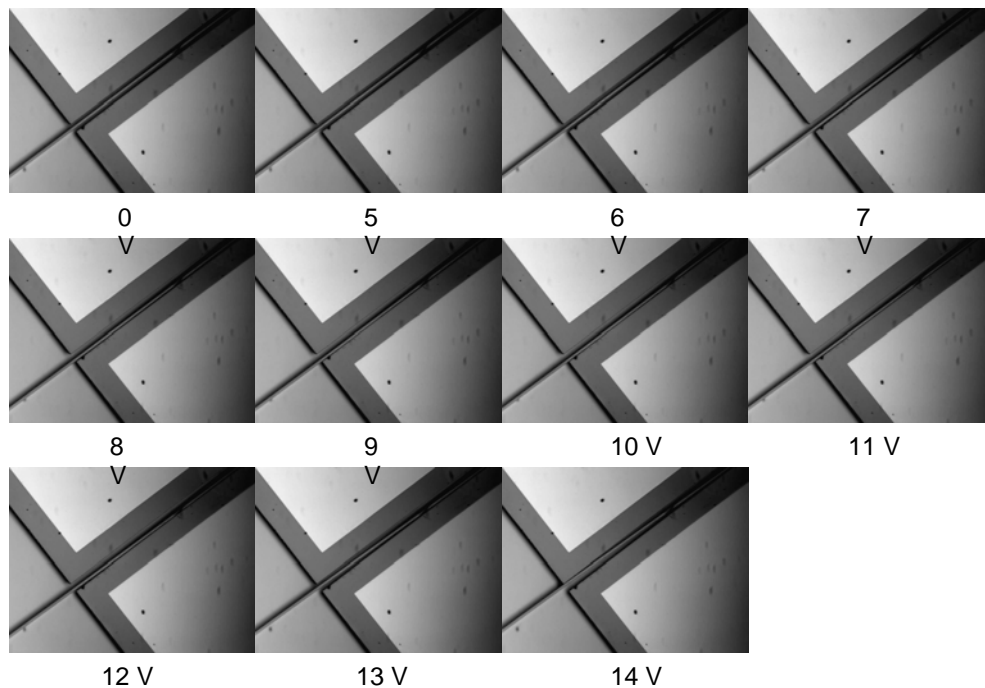


Figure 5.07: Deflection of bridge for certain values of DC voltages at corner portion of electrodes

Since the platform did not rotate or move in any way significantly, the mode that was being seen under the microscope corresponds to the bridge mode (two fixed ends). This experiment illustrates how soft the bridge mode is – apparently softer than the rotational mode of the device. Being able to deflect the bridge significantly by applying a relatively small DC voltage was early proof that the rotational mode might not be soft enough to be found electrostatically. That is, the bridge mode will be more easily visible instead.

According to Figure 5.07, it would seem that the pull-in voltage for the bridge mode is around 15 V. Theoretically, the pull-in voltage is calculated as follows (using equations 2.44 and 2.92, and Tables 3.01 and 3.04):

$$V = 4wtL$$

$$V = 2.5 \times 10^{-12} \text{ m}^3 \quad 5.01$$

$$m = 5.83 \times 10^{-9} \text{ kg} \quad 5.02$$

$$k_R = 0.0634 \text{ N-m} \quad 5.03$$

$$V_p = 1.63 \text{ V} \quad 5.04$$

The theoretical value is much smaller than the supposed actual value. However, it has already been mentioned that the potential drop is suspected to be from the bridge to the substrate (which is grounded), instead of from the bridge to the electrode. Most of the voltage being applied to the device could be dropping to ground.

5.2.2 Resonance Detection

Electrostatic detection of rotational resonance was not successful, as previously mentioned. However, resonance of a higher order mode was detected – the bridge mode corresponding to modes five, six, and seven in Table 3.03.

5.2.2.1 Device in Vacuum

The device was kept under vacuum (shown in Figure 5.08) while all the resonance detection tests were done. Vacuum was achieved by using a Pyrex bell jar sealed to a metal base with high vacuum grease and either a dry vacuum pump or an oil-based roughing pump (Alcatel Dryel 31 or Alcatel 2008A). A Varian Multi-Gauge was used to measure the vacuum within the bell jar. With the

vacuum pump, the pressure inside the bell jar was lowered to 4.24 mT, and with the oil pump the pressure was at 6.8 mT.



Figure 5.08: Device in vacuum, achieved by using a bell jar and a pump

As can be seen in the figure, a total of seven coaxial cables are run from the PCB to the metal base. Connections to the laboratory equipment were conveniently made from underneath the metal base.

5.2.2.2 Important Circuit Components

In each circuit described in the later subsections of this chapter, there are three main components: the voltage sources, amplifiers, and lock-in amplifiers. The purposes of the voltage sources are simple. The AC voltage source provides the driving frequency found in equation 2.52. It is used to drive the device into resonance. The DC bias provides and maintains a potential difference to the circuit.

An inverting operational amplifier is used to amplify the signal before it is received by a lock-in amplifier [52]. The lock-in amplifier detects small AC

signals using phase sensitive detection [53]. It will only receive signals that are at the reference frequency. As a result, all noise that is not at the reference frequency is eliminated. The reference frequency signal is provided by an external source, which is synchronized to the lock-in amplifier. The voltage is measured in root-mean-square (RMS) units, and the phase is measured in degrees.

5.2.2.3 Single Lock-In

As the name implies, only one lock-in amplifier is employed in this method of resonance detection. In this case, the Stanford Research 830 DSP Lock-In Amplifier was used along with the Stanford Research 570 Low Noise Current Amplifier at the 10^{-6} gain setting. Both are suitable for low frequency ranges (10 Hz - 5 kHz) [53, 54]. The HP 33120A and the HP 3245A were used as the AC and DC sources, respectively.

Figure 5.09 shows the electrical setup. On the one side of the bridge is the drive electrode, and on the other side of the bridge is the detection electrode. The DC bias is applied to the bridge and the substrate is grounded using 50 Ω SMA terminators. The other two unused electrodes are also grounded using SMA terminators. As the AC current flows into the one electrode causing the bridge to oscillate, the amplifier and the lock-in amplifier on the other side of the bridge pick up the oscillating signal. Theoretically, when the AC current is at the resonant frequency of the device, the amplitude of the oscillations will begin to increase. The increase in oscillations would show up as a peak in the data.

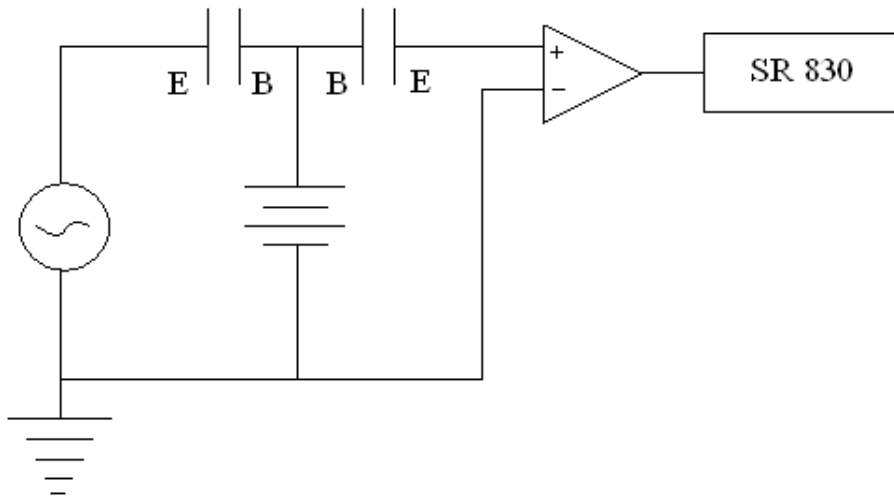


Figure 5.09: Basic single lock-in circuit, using the SR 570 as the amplifier. The frequency ranges from 10 Hz – 5 kHz.

A more sensitive alternative to this setup is illustrated in Figure 5.10. To avoid picking up noise from the drive electrode, the detection side of the circuit was moved to an electrode on the other side of the platform. Since the rotational mode is symmetrical, the non-driven bridge should also move if resonance is achieved.

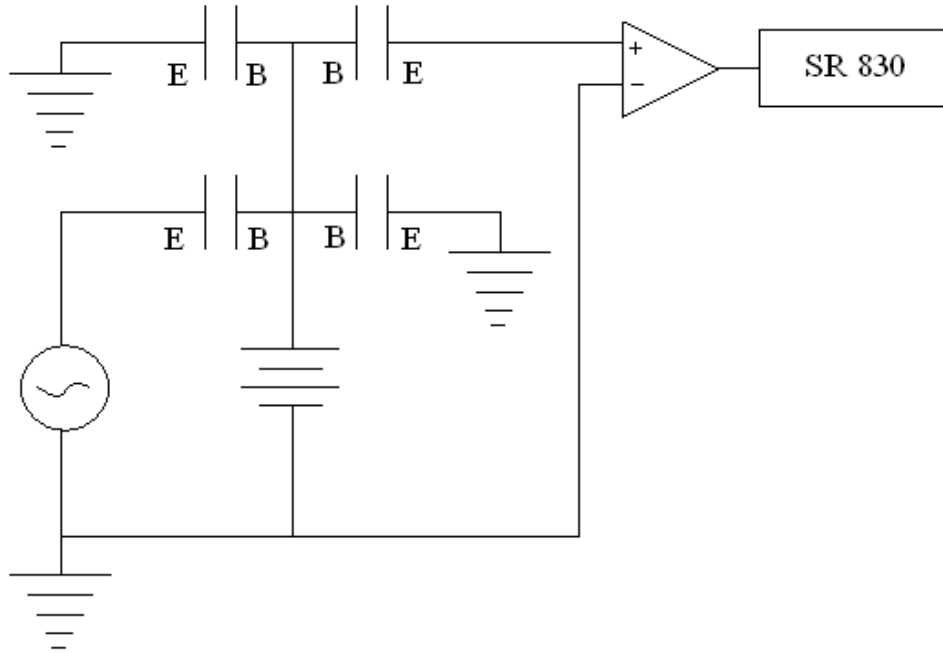


Figure 5.10: A more sensitive version of the basic single lock-in circuit

Another sensitive alternative to the basic single lock-in setup is to compensate for the electrode to electrode capacitance, thus driving the background down by a significant amount. The General Radio 1615 Capacitance Bridge was used for this attempted compensation, with the variable capacitor set at 0.2 pF. By definition, along with a variable capacitor it contains a transformer allowing it to nullify the signal coming from the electrode to electrode capacitance. It can also accept a range of frequencies, which the AH 2500A cannot do (The AH 2500A uses a fixed frequency of 1 kHz [51]). Figure 5.11 illustrates how the 1615 is connected to the circuit.

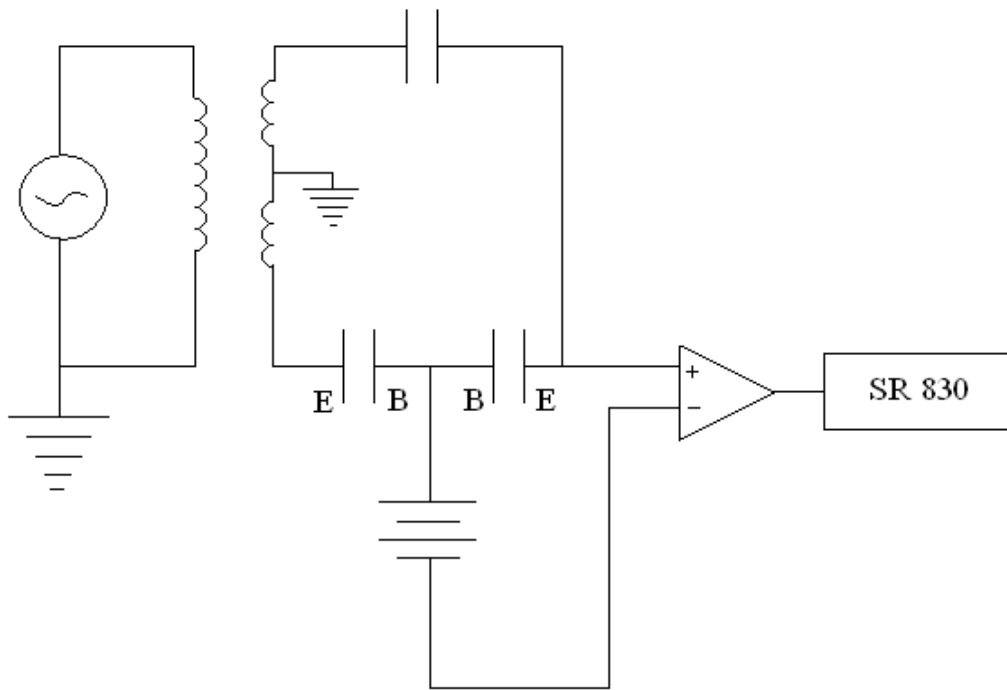


Figure 5.11: Another sensitive version of the basic single lock-in, using a transformer (the 1615)

Unfortunately, the capacitance of the electrode to electrode was too small for the 1615 to compensate for – the signal was the same order of magnitude regardless of whether or not the 1615 was connected. This is demonstrated in Figures 5.12 and 5.13. The frequency sweep shown in Figure 5.12 was done at 1 V_{pp} (peak to peak), 7 V_{dc} (DC voltage), with 0.1 Hz steps. The frequency sweep shown in Figure 5.13 was done at 0.5 V_{pp} , 5 V_{dc} , with 2 Hz steps. The varying parameters for both sweeps account for some of the minor differences, but there is no significant difference.

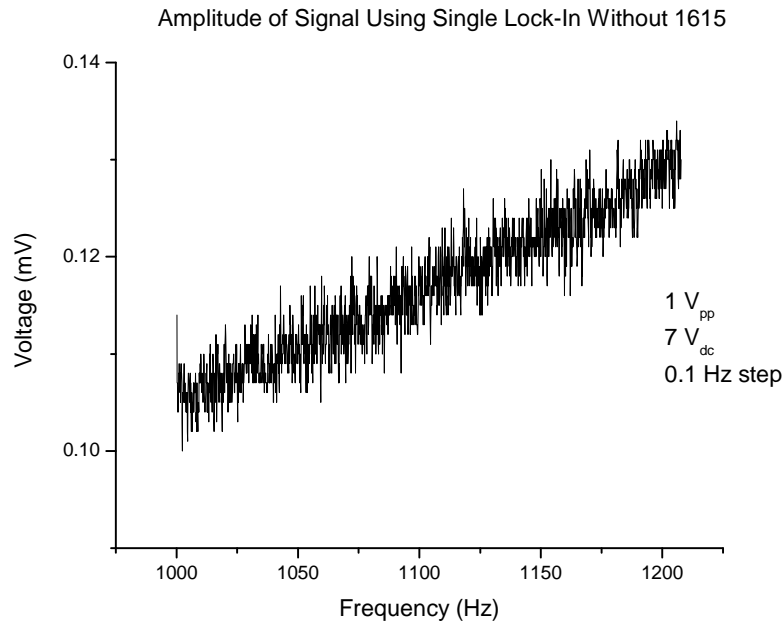


Figure 5.12: Amplitude of signal using single lock-in without 1615

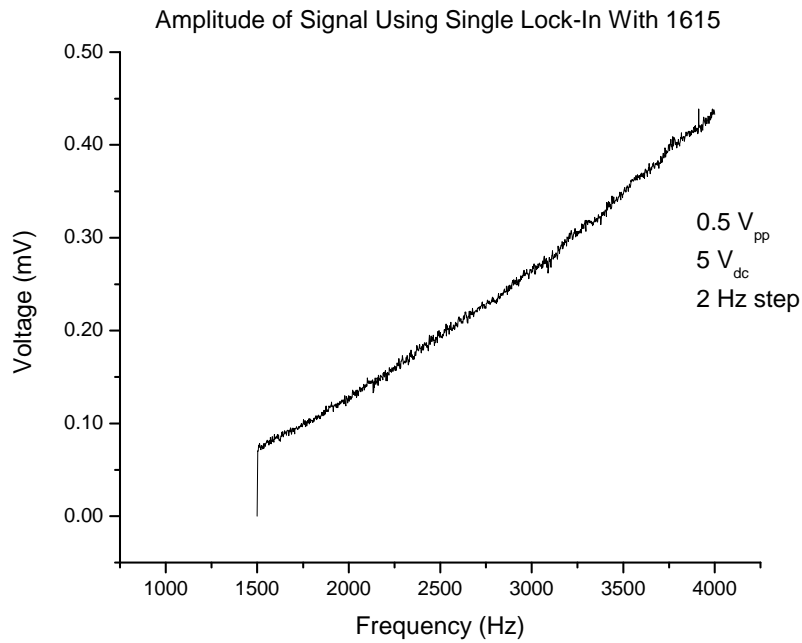


Figure 5.13: Amplitude of signal using single lock-in and 1615

Rotational resonance was not found using any single lock-in circuit, therefore the next step was to design a more sensitive circuit that might pick up the apparently very small resonant signal. More results from the testing will be shown and discussed in a later subsection.

5.2.2.4 Double Lock-In

As already seen, reducing the background signal as low as possible is the motivation for all the different tests. The reason for not finding the rotational resonant thus far could be that it was being lost in noise. The Amptek A250 Charge Sensitive Operational Amplifier has a lower noise floor compared to the SR 570 model used for the single lock-in. However, the Amptek does not work well with frequencies of lower than 20 kHz, thus it could not be used in the single lock-in setup [55].

The double lock-in method involves using two lock-in amplifiers, the SR 830 and the SR 844 RF Lock-In Amplifier. The SR 844 can also provide a reference frequency signal of up to 20 MHz [56]. This signal was measured to be at 8.4 V by the HP 54600B Oscilloscope. Since the SR 844 can only take in a signal of 1 V or less, the input signal coming from the circuit was not being read. Thus the reference signal from the SR 844 was diminished to ~ 2.4 V using an attenuator. The modulated signal containing the low frequency signal (10 Hz – 1 kHz) from the HP 33120A and the high frequency signal (100 kHz) from the SR 844 was fed into the circuit as shown in Figure 5.14. After passing through the Amptek, the signal was demodulated in the SR 844, and the low frequency signal was picked up by the SR 830. The double lock-in method was done with the detection electrode directly across the drive electrode (Figure 5.14), with the detection electrode on the other side of the platform (Figure 5.15), and with the high frequency signal applied to the electrode across from the detection electrode instead of in series with the DC bias (Figure 5.16). The last test done was the double lock-in with a transformer connected to the high frequency electrode and the detection electrode, to cancel out the noise from the electrode to electrode capacitance (Figure 5.17). A transformer with a more sensitive home made variable capacitor was employed instead of the 1615. The variable capacitor was tinkered with until the signal voltage of the electrode to electrode signal was at its lowest.

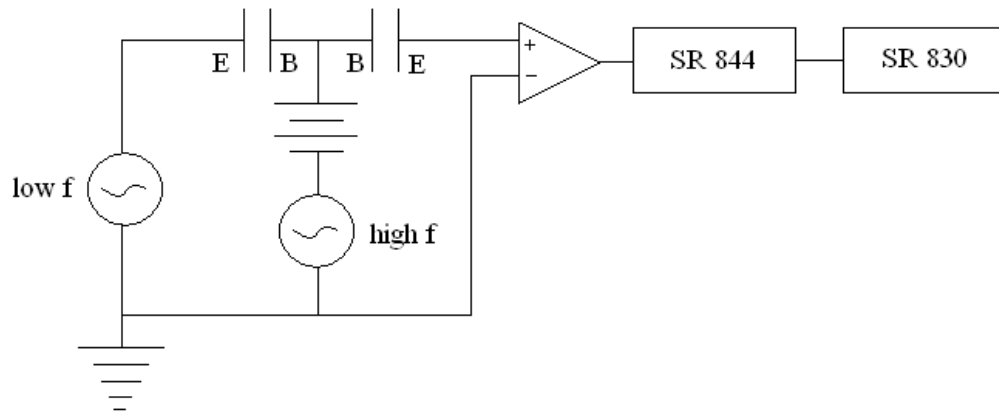


Figure 5.14: Basic double lock-in circuit, with the AMTEK as the amplifier. The low frequency ranges from 10 Hz – 10 kHz and the high frequency is set at 100 kHz.

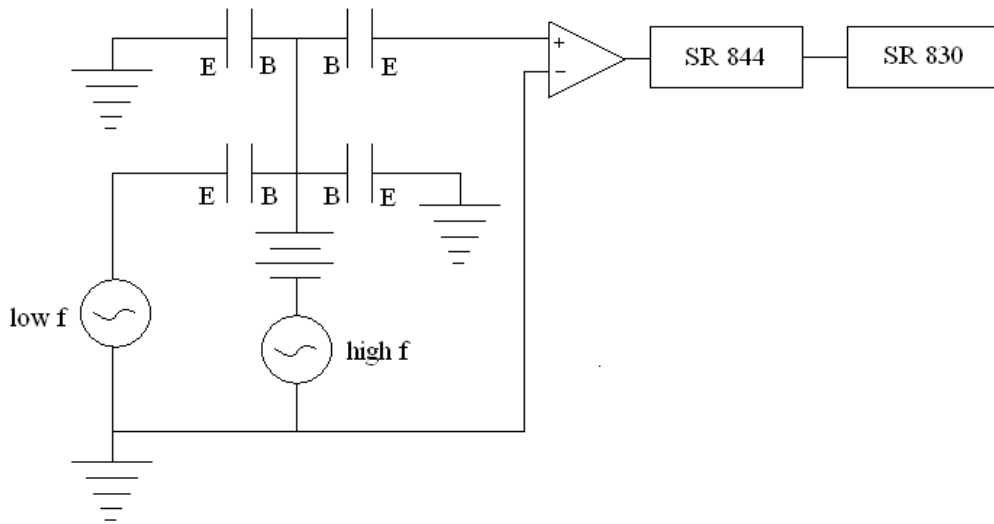


Figure 5.15: Second double lock-in circuit

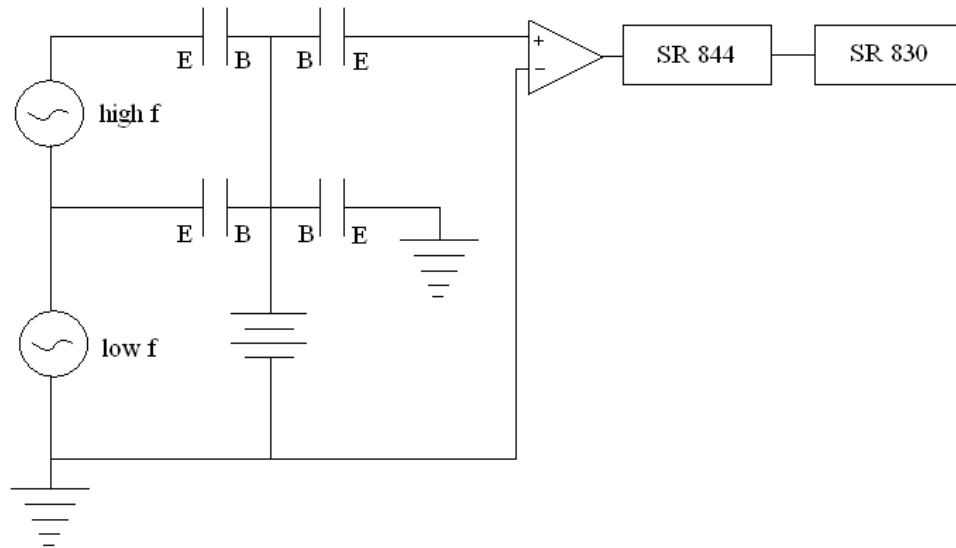


Figure 5.16: Third double lock-in circuit

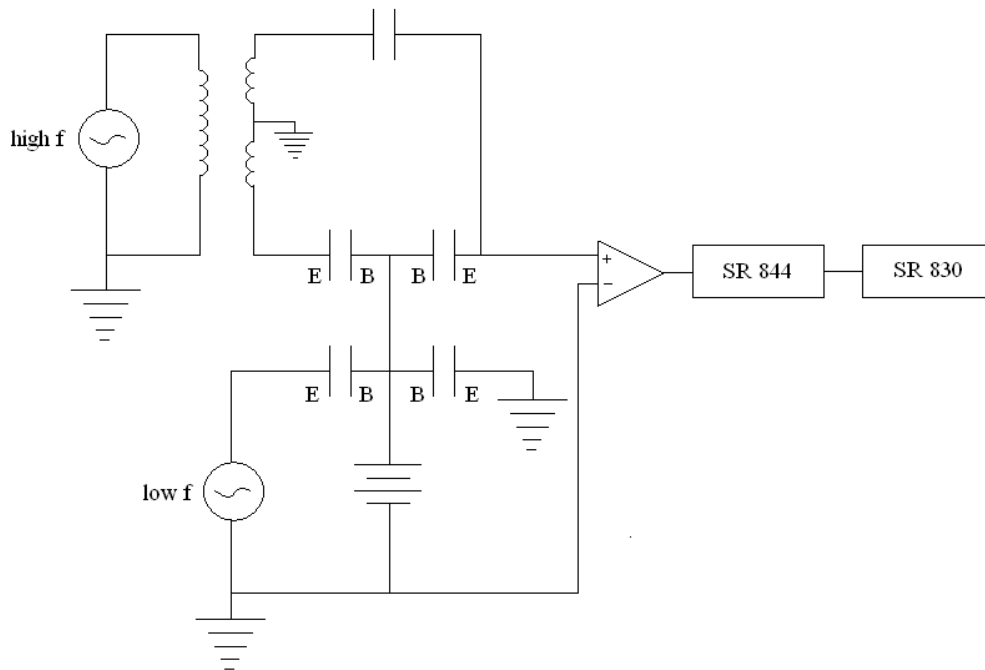


Figure 5.17: A sensitive version of the double lock-in, using a transformer

The addition of the transformer to the double lock-in circuit drove the background down by a factor of ~ 0.25 , as shown in Figure 5.18. The peaks that

are seen are not resonant peaks from the device, but are rather oscillations due to the equipment or the environment. When sweeps are done at low frequencies (10-1000 Hz), many of these oscillations can be seen, as illustrated in Figure 5.19. The frequency of the power lines connected to the lab is 60 Hz, thus at that frequency and at multiples of that frequency oscillations will naturally occur in the data. In the particular data plot in Figure 5.19, the 4th, 9th, 11th, 13th, and 14th harmonics of the 60 Hz resonance can be seen. A similar sweep was run at 1 V_{dc} (all other parameters the same), with similar results – but fewer harmonics appear. Oscillations that are not at multiples of 60 Hz are attributed to environmental effects or to the electrical equipment. Each oscillation was investigated and determined not to be a resonance. Again, the corresponding phase (not shown) does not show any change.

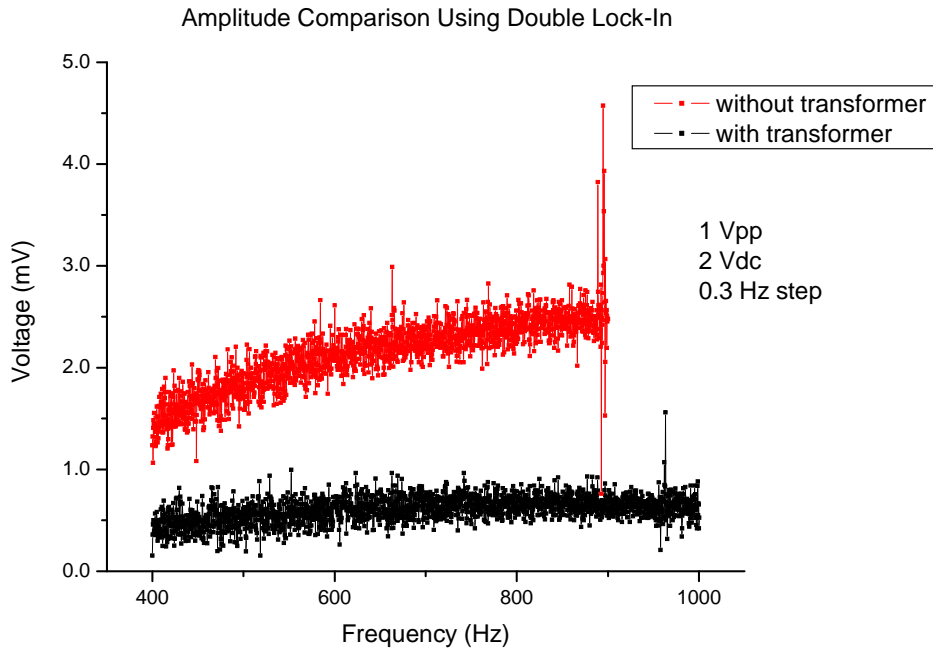


Figure 5.18: Amplitude comparison using double lock-in

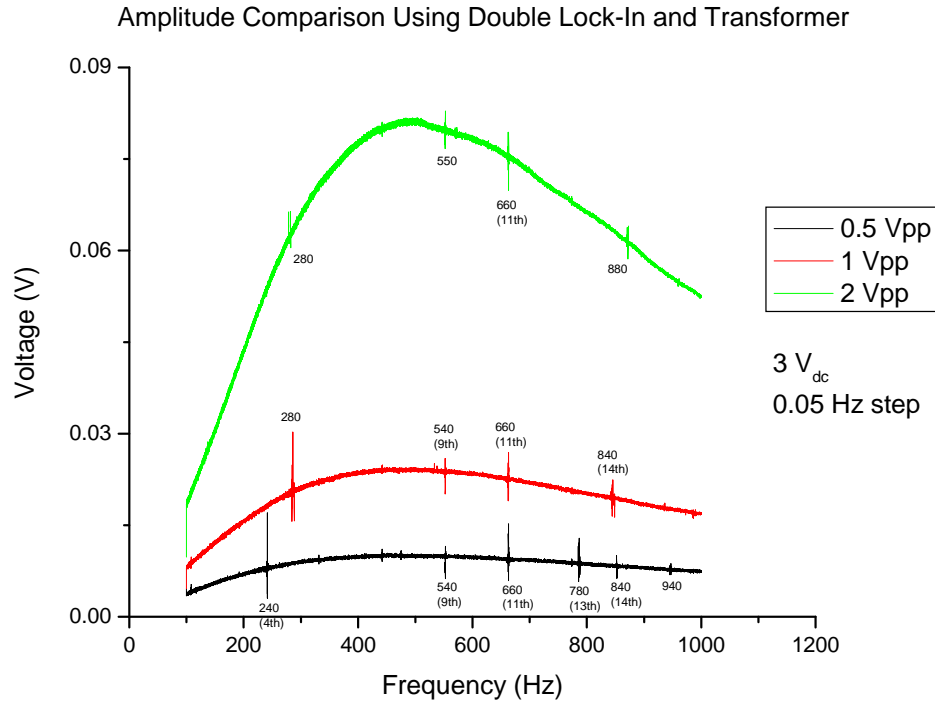


Figure 5.19: Amplitude comparison using double lock-in and transformer

5.2.2.5 Discussion of Results

Testing the single lock-in and the double lock-in methods at higher frequencies (1000-8000 Hz) generated the resonant peak of the bridge mode, seen in Figures 5.20 – 5.24. There are two different bridges that were tested – the bridge between electrodes 1 and 2, and the bridge between electrodes 3 and 4. Ideally, the two bridges should be identical. However, the resonant peak of the one between electrodes 1 and 2 (B12) is located at 6600 Hz, whereas the resonant peak of the other (B34) is located at ~3000 Hz. The difference is due to the physical dissimilarities of the two bridges. Both bridges were tested within the range of 1000-8000 Hz, and only the one peak was found for each. Since the single lock-in is only suitable for frequencies up to 5000 Hz (due to the restraints of the SR 570), the resonant peak of B12 was detected using the double lock-in (circuit corresponding to Figure 5.15, with the drive electrode directly across the detect electrode), and the resonant peak of B34 was detected using the single lock-in (circuit corresponding to Figure 5.09).

The first time the resonant peak of the bridge mode was seen using the single lock-in method, the peak was located at 2600 Hz. A month later, the peak

had shifted up to 3000 Hz. According to ANSYS data, the bridge mode should be at approximately 3300 Hz. A number of factors could have contributed to the actual peak being lower – the dimensions of the bridge are not exact, and residue from materials used in the fabrication stage may have remained in certain areas. Likewise, these things could account for the resonant peak of B12 being much higher than expected. Looking at the peaks, one can see the gradual shifting up of the amplitude, and then the abrupt drop to below the baseline. The corresponding phase plots show a phase change of approximately 40° . Ideally, the resonant peaks would not have the abrupt drop, and the phase would change by 180° . This is due to background capacitances that have not been compensated for.

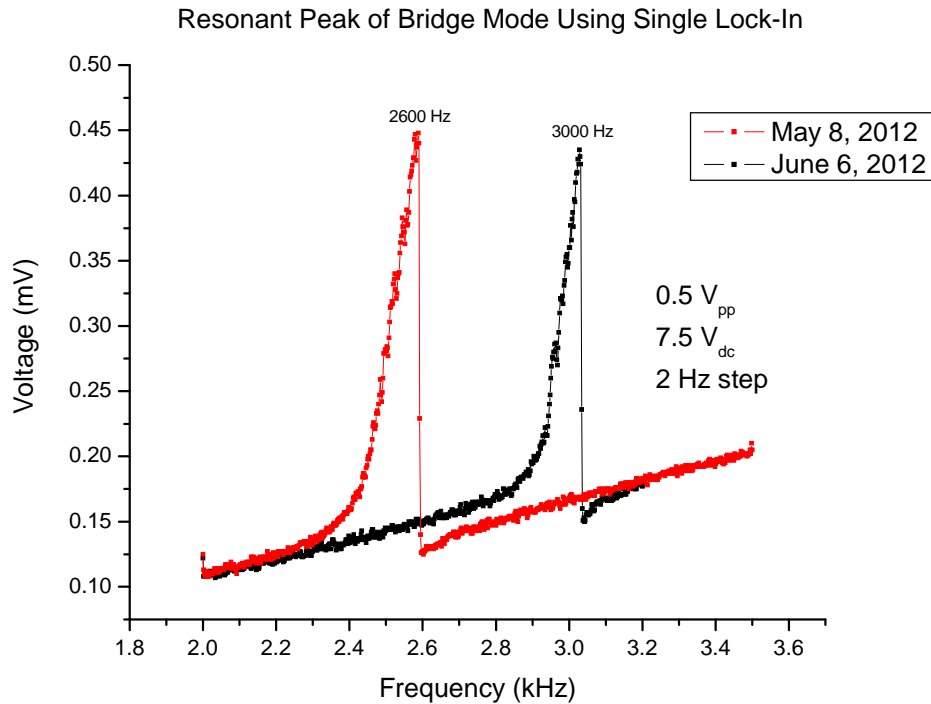


Figure 5.20: Resonant peak of bridge mode (B34) corresponding to different dates using the single lock-in method

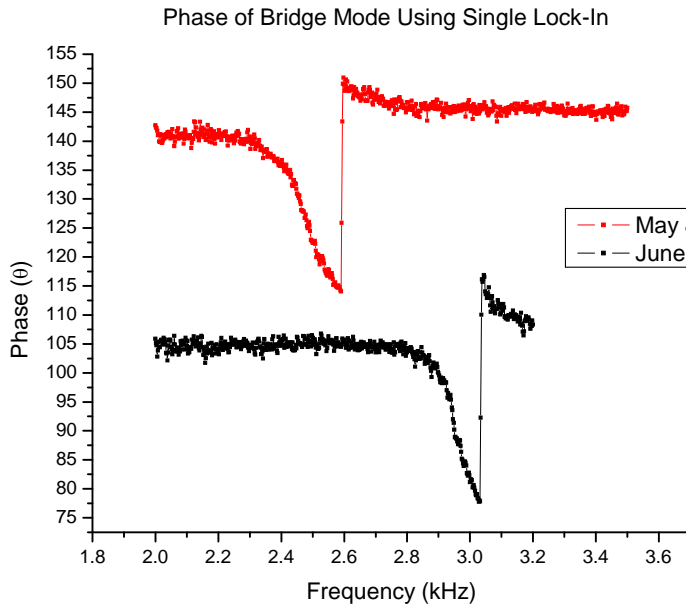


Figure 5.21: Phase of bridge mode (B34) corresponding to different dates using the single lock-in method

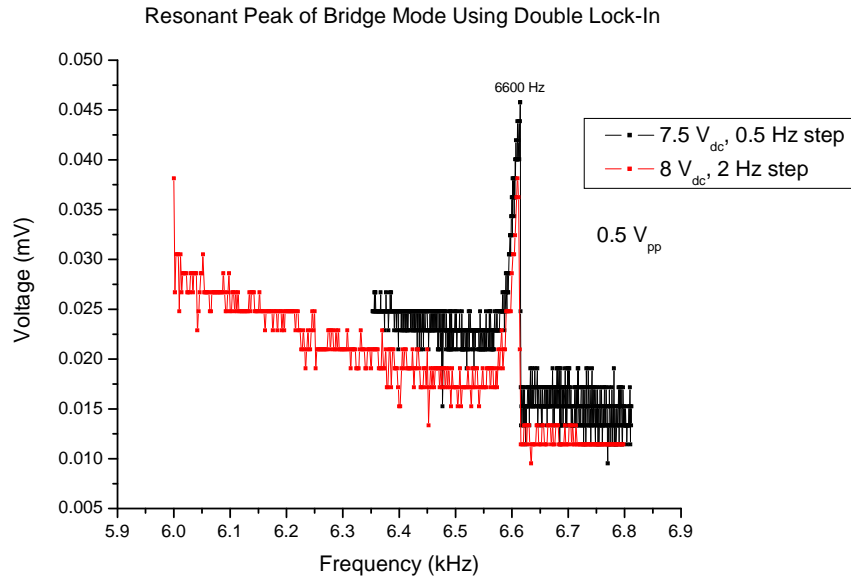


Figure 5.22: Resonant peak of the bridge mode (B12) with different parameters using the double lock-in method

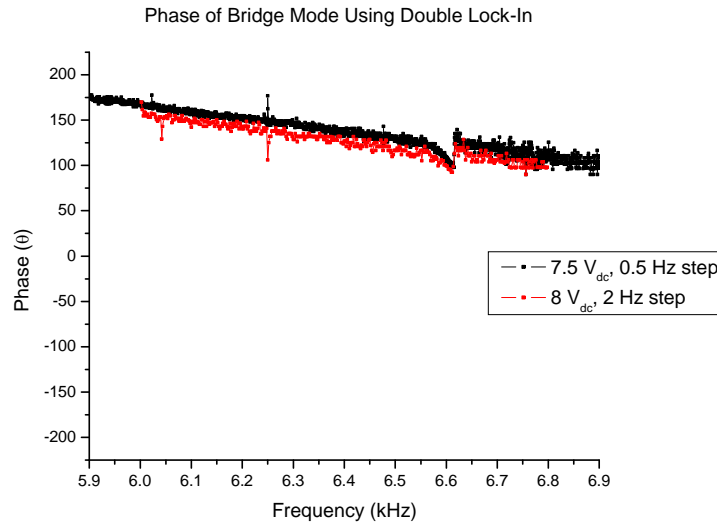


Figure 5.23: Phase of bridge mode (B12) with different parameters using the double lock-in method

The fact that the bridge mode resonance can be seen by using the single and double lock-in methods show that there is no error in the circuitry. Both the single lock-in and the double lock-in methods were tested at low frequencies (10-1000 Hz) with varying parameters to search for the rotational resonance. Applied voltages were in the range of 0.5-2 V_{pp} and 1-8 V_{dc} – high enough without running into the pull-in effect. The step sizes ranged from 0.01-5 Hz. Referring back to equation 2.62 and using the rotational frequency value from Table 3.04, a step size of 0.01 Hz gives a quality factor of approximately 66,800. The quality factor of the rotational mode is not known, but is estimated to be high – approximately 1,000. Thus it could not be argued that the system is not given enough time to reach resonance.

Looking at the data corresponding to 0.5 V_{pp} in Figure 5.19, it can be seen that the background has been driven low enough that four of the 60 Hz harmonics can be seen as well as two other oscillations attributed to environmental effects or to the electrical equipment. Going from the basic single lock-in circuit to the double lock-in with a transformer, the background has successfully been driven down by a factor of approximately 15. Using the double lock-in with the transformer, the baseline is sufficiently low enough that if the resonance of the rotational mode were to occur, it should be noticeable.

It has been proven and seen that the platform and bridges are fully released. It has been proven that the single and double lock-in methods work as methods of resonance detection. It has been proven that the parameters of each test were sufficient, and that the background of the data was low enough that if

rotational resonance were to occur, it would be seen. Then why is rotational resonance not seen electrostatically?

The answer lies in the softness of each mode. The stiffness of a mode depends on the geometry of the object, its boundary conditions, and the material. In this case, the material is the same, so the defining differences are the geometry and the boundary conditions. The rotational mode is less flexible and more restricted than the bridge mode, thus it is stiffer. Looking at Table 5.02, the stiffness of the rotational mode is almost three times greater than the bridge mode. The large difference in frequency is due to the mass of the device being approximately 100 times greater than the mass of the bridge (equation 2.44). Applying a DC voltage softens the bridge mode (as seen earlier in the chapter), thus when a frequency sweep is done, the rotational mode is prevented from occurring.

Table 5.02: Comparison of stiffnesses and frequencies

Mode	Frequency (Hz)	Stiffness (N-m)
Rotational	668.44	0.174
Bridge	3330.0	0.0634

5.3 Magnetic Torque Resonance Detection

Electrostatically, the rotational mode could not be easily measured. However, this does not reflect poorly on the design of the torque magnetometer – when a torque is applied to the platform, the rotational mode is still the fundamental mode. Therefore, the best way to investigate the rotational resonance of the torque magnetometer would be to apply a force to the platform instead of the bridge. This can be done simply by gluing a magnetic sample to the platform and applying a magnetic field to the device over a frequency range, very similar to the purpose for which the torque magnetometer was designed.

To carry out this method, a procedure for placing the sample on the device needs to be developed. Since the platform has holes, different types of glue need to be tested for viscosity. The sample itself should have a known magnetic moment and alignment, so that the needed magnetic field strength can be calculated and applied. A way of applying a magnetic field needs to be developed as well. A suggestion would be to use a simple speaker coil connected to a power supply. Using a Bell 610 Gaussmeter with a Hall probe distanced 2 mm away from the center of the coil to measure the field, a speaker coil can generate a 1.1 mT magnetic field at a DC voltage of 6.0 V and a current of 0.44 A (The Agilent E3630A Triple Output DC Power Supply was used to supply the voltage). This method of resonance detection has a very high probability of producing good results.

6. Conclusion

Throughout the course of this project, a number of accomplishments have been made. Most of the proposed goals have been reached. The main goals of this thesis project were to uniquely design, fabricate, and test a capacitive MEMS torque magnetometer. The purpose of the torque magnetometer is to measure the torque of magnetic crystals, giving valuable insight into the properties of superconducting materials. This chapter will quickly review what has been completed and what further work can be done.

6.1 Main Accomplishments

A number of capacitive MEMS torque magnetometers of a particular design have been successfully fabricated and released. Several fabrication procedures were attempted before arriving at the successful perforated platform process. This process has been condensed into three main stages: metallization, DRIE, and release; with a heavy emphasis on DRIE and using the critical point dryer. If all resources and equipment were available in one cleanroom, a batch of torque magnetometers could be efficiently made by one person in one working day.

Numerical analyses were performed and a list of modes corresponding to the particular design of the torque magnetometer was generated. One mode (the bridge mode) was excited electrostatically and recorded. This mode was seen in both bridges, with the resonant peak of the one being at ~ 3000 Hz and the resonant peak of the other being at 6600 Hz. Resonance of the first bridge was detected by using the single lock-in method, and resonance of the second bridge was detected by using the double lock-in method.

Several electrostatic tests were developed and executed to search for the rotational resonant peak. None of the tests showed a noticeable peak within a range of 10-2000 Hz. This led to further analyses of the modes of the device, and eventually led to the conclusion that due to the unique design of the torque magnetometer, the rotational resonance cannot be easily measured electrostatically.

Having found the bridge modes at a frequency relatively near the values computed by ANSYS (taking into account physical deviations from the design) suggests that the fabricated MEMS torque magnetometer is behaving as theoretically expected. As such, the torque magnetometer should be able to be used for the purpose for which it was designed.

6.2 Future Work

The successfully fabricated and released MEMS torque magnetometer was a revision of an earlier design. The earlier design consisted of a solid platform, whereas the revised design has a perforated platform which contributed largely to the success of the fabrication. A challenge would be to develop a fabrication procedure that could create a fully released MEMS torque magnetometer with a solid platform. This particular design would allow for easy attachment of the sample to the device – there would be no holes for glue to seep through. Releasing a device that contains both fully supported and free standing macro and micro features would also be an interesting feat to accomplish.

Detection of the rotational resonance is also another goal to reach. A suggested method has been laid out in the previous chapter, and has a high chance of producing the desired results. Once it has been established that the rotational mode can be seen, the torque magnetometer can then be used for the purposes for which it was designed. Some time in the future, this torque magnetometer could be commercially reproduced for research purposes in the field of magnetic crystals and/or superconductors.

References

1. Feynman, Richard P. There's Plenty of Room at the Bottom. *Journal of Microelectromechanical Systems*, Vol 1, No 1, March 1992.
2. Feynman, Richard. Infinitesimal Machinery. *Journal of Microelectromechanical Systems*, Vol 2, No 1, March 1993.
3. Kaajakari, Ville. *Practical MEMS*. Small Gear Publishing, 2009.
4. Tai-Ran Hsu. *MEMS and MICROSYSTEMS Design and Manufacture*. McGraw-Hill Book Company, 2002
5. Peterson, Kurt E. Silicon as a Mechanical Material. *Proceedings of the IEEE*, Vol 70, No 5, May 1982.
6. Bean, Kenneth E. Anisotropic Etching of Silicon. *IEEE Transactions on Electron Devices*. Vol ED-25, No 10, October 1978.
7. Bustillo, James M. et al. Surface Micromachining for Microelectromechanical Systems. *Proceedings of the IEEE*, Vol 86, No 8, August 1998.
8. Kovacs, Gregory T.A. et al. Bulk Micromachining of Silicon. *Proceedings of the IEEE*, Vol 86, No 8, August 1998.
9. Foner, S. Review of Magnetometry. *IEEE Transactions on Magnetics*, Vol 17, No 6, November 1981.
10. Aczel, A.A. *Studies of Bose-Einstein Condensates in Magnetic Insulators*. Ph.d. thesis. McMaster University, Canada, 2010.
11. Cullity, B.D. and Graham, C.D. *Introduction to Magnetic Materials*, John Wiley & Sons Inc, 2nd ed, 2009.
12. Heydon, G.P. et al. Resonant Torque Magnetometry: a new in-situ technique for determining the magnetic properties of thin film MFM tips. *IEEE Transactions on Magnetics*, Vol 33, No 5, September 1997.
13. Farrell, D.E. et al. Experimental Evidence for Flux-Lattice Melting. *Physical Review Letters*, Vol 67, No 9, August 1991.
14. Zijlstra, H. *Experimental Methods in Magnetism*, Vol. IX. John Wiley & Sons, 1967.

15. P.J. Flanders. An alternating-gradient magnetometer. *Journal of Applied Physics*, Vol 63, No 8, April 15, 1988.
16. Biggar, R.D. and Parpia, J.M. High-Q oscillator torque magnetometer. *Review of Scientific Instruments*, Vol 69, No 10, October 1998.
17. Rossel, C. and Bauer, P. Active microlevers as miniature torque magnetometers. *Journal of Applied Physics*, Vol 79, No 11, June 1996.
18. Brugger, J. et al. Microfabricated ultrasensitive piezoresistive cantilevers for torque magnetometry. *Sensors and Actuators*, Vol 73, 1999.
19. Rossel, C. et al. Torsion cantilever as magnetic torque sensor. *Review of Scientific Instruments*, Vol 69, No 9, Sept. 1998.
20. Kohout, Stefan et al. Novel sensor design for torque magnetometry. *Review of Scientific Instruments*, Vol 78, January 2007.
21. Qvarford, M. et al. Microtorquemeter for magnetization measurements on small superconducting samples. *Review of Scientific Instruments*, Vol 63, No 12, December 1992.
22. Heydon, G.P. et al. Resonant Torque Magnetometry: a new in-situ technique for determining the magnetic properties of thin film MFM tips. *IEEE Transactions on Magnetics*, Vol 33, No 5, September 1997.
23. Moreland, John et al. Micromechanical Torque Magnetometer for In Situ Thin-Film Measurements. *IEEE Transactions on Magnetics*, Vol 37, No 4, July 2001.
24. Beer, Ferdinand P. and Johnston, Russel Jr. *Mechanics of Materials*. McGraw-Hill Book Company, 2nd ed. 1992.
25. WIKA Instruments. *Technical terms used when specifying pressure transducers*. The Official Journal of the SAIMC, July 2002.
<<http://www.instrumentation.co.za/article.aspx?pkarticleid=1904>>
26. Weaver, William Jr. et al. *Vibration Problems in Engineering*. John Wiley & Sons, 5th ed, 1990.
27. McQuarrie, Donald A. *Mathematical Methods for Scientists and Engineers*. University Science Books, 2003.

28. Wolfe, Joe. Strings, standing waves and harmonics. University of New South Wales, Sydney, Australia. <www.phys.unsw.edu.au/jw/strings.html>
29. *Forced Vibration of a Cantilever Beam (Continuous System)*. Sakshat Virtual Labs. 2012. <<http://iitg.vlab.co.in/?sub=62&brch=175&sim=1081&cnt=1>>
30. Fowles and Cassiday. *Analytical Mechanics*. Thomson Brooks/Cole, 7th ed, 2005.
31. Thornton, Stephen T. and Marion, Jerry B. *Classical Dynamics of Particles and Systems*. Thomson Brooks/Cole, 5th ed, 2004.
32. Serway and Jewett. *Physics for Scientists and Engineers with Modern Physics, Volume 2*. Brooks/Cole, 6th ed, 2004.
33. R. Nave. *Electricity and Magnetism: Bar Magnet*. HyperPhysics, Georgia State University, 2012.
<<http://hyperphysics.phy-astr.gsu.edu/hbase/magnetic/elemag.html>>
34. Knight, Randall D. *Physics for Scientists and Engineers with Modern Physics: A Strategic Approach*. Addison Wesley, 2004.
35. Colwell, Catherine H. *Magnetic Field Along the Axis of a Current Loop*. PhysicsLAB, 1997-2012.
<http://dev.physicslab.org/Document.aspx?doctype=3&filename=Magnetism_BiotSavartLaw2.xml>
36. *MIT courseware 8.02SC Physics II: Electricity and Magnetism*, Fall 2010.
<http://ocw.mit.edu/courses/physics/8-02sc-physics-ii-electricity-and-magnetism-fall-2010/biot-savart-law/MIT8_02SC_notes19to20.pdf>
37. Stolarski, T. et al. *Engineering Analysis with ANSYS Software*. Elsevier, 2006.
38. *MICROPOSIT S1800 SERIES PHOTO RESISTS*. Shipley.
<<http://www.nanophys.kth.se/nanophys/facilities/nfl/resists/S1813/s1800seriesDataSheet.pdf>>
39. Williams, Kirt R. et al. Etch Rates for Micromachining Processing-Part II. *Journal of Microelectromechanical Systems*, Vol 12, No 6, December 2003
40. Roxhed, Nicolas et al. A method for tapered deep reactive ion etching using a modified Bosch process. *Journal of Micromechanics and Microengineering*, Vol 17, April 2007.

41. Chang, Chienliu et al. Etching submicrometer trenches by using the Bosch process and its application to the fabrication of antireflection structures. *Journal of Micromechanics and Microengineering*, Vol 15, January 2005.
42. Sun, Guangyi et al. 3-D Simulation of Bosch Process with Voxel-Based Method. *Proceedings of the 2nd IEEE International Conference on Nano/Micro Engineered and Molecular Systems*. January 2007.
43. *Negative Tone Photoresist Formulations 2-25*. Microchem, Revision 2, 2002.
<http://www.microchem.com/products/pdf/SU8_2-25.pdf>
44. *NEGATIVE RESIST NR9-1500P*. Futurrex, Inc.
<<http://www.davidlu.net/NR9-1500P.pdf>>
45. Namatsu, Hideo et al. Dimensional limitations of silicon nanolines resulting from pattern distortion due to surface tension of rinse water. *Applied Physics Letters*, Vol 66, No 20, May 1995.
46. *tousimis® Autosamdri®-815 Series B Manual*. ©tousimis, 2005.
47. *Critical Point Dryers & Freeze Dryers*. Quorum Technologies, ProSciTech Pty Ltd. July 2012.
< <http://www.proscitech.com/cataloguex/online.asp?page=k3>>
48. Williams, Kirt R. and Muller, Richard S. Etch Rates for Micromachining Processing. *Journal of Microelectromechanical Systems*, Vol 5, No 4, December 1996.
49. *KOH Etching*. Brigham Young University.
<www.cleanroom.byu.edu/KOH.phtml>
50. *Oxide Growth Calculator*. Brigham Young University.
<www.cleanroom.byu.edu/OxideThickCalc.phtml>
51. *AH 2500A 1 kHz Ultra-Precision Capacitance Bridge Operation and Maintenance Manual*. Andeen-Hagerling, Inc., 2nd Ed, 1994.
52. Horowitz, Paul and Hill, Winfield. *The Art of Electronics*. Cambridge University Press, 2nd Ed, 1989.
53. *Model SR830 DSP Lock-In Amplifier Operating Manual and Programming Reference*. Stanford Research Systems, Inc., Revision 1.4, 1995.

54. *Model SR570 Low-Noise Current Preamplifier Operating Manual and Programming Reference*. Stanford Research Systems, Inc., Revision 1.6, 2005.

55. *Amptek Charge Sensitive Amplifier A250*. Amptek Inc., August 27, 2008.
<www.amptek.com/a250.html>

56. *Model SR844 RF Lock-In Amplifier Operating Manual and Programming Reference*. Stanford Research Systems, Inc., Revision 2.3, 1997.